DEUTERON PRODUCTION IN AU+AU COLLISIONS AT 1.23A GEV

Goethe Universität Frankfurt am Main
Fachbereich Physik
Institut für Kernphysik

Master's Thesis

Author: Maximilian Zuschke, 5171277
First Supervisor: Prof. Dr. Christoph Blume
Second Assessor: Dr. Manuel Lorenz

Frankfurt, October 30, 2017

Abstract

In April and May 2012 data on Au+Au collisions at beam energies of $E_{kin} = 1.23A$ GeV were collected with the High Acceptance Di-Electron Spectrometer (HADES) at the GSI *Helmholtzzentrum für Schwerionenforschung* facility in Darmstadt, Germany.
In this thesis, the production of deuterons in this collision system is investigated.
A total number of 2.1×10^9 Au+Au events is selected, containing the most central 0-40% of events. After particle identification, based on a mass determination via time-of-flight and momentum and on a measurement of the energy loss, the transverse mass spectra of the deuteron candidates are extracted for various rapidities and subsequently corrected for acceptance and efficiency.
The inverse slope parameter of a Boltzmann fit applied to the transverse mass spectra at midrapidity, which is referred to as the *effective temperature*, is extracted. For a static thermal source, this parameter corresponds to the kinetic freeze-out temperature T_{kin} and is therefore expected to be smaller or equal to the chemical freeze-out temperature T_{chem}. The extracted effective temperature of $T_{eff} = (190 \pm 10)$ MeV however exceeds the chemical freeze-out temperature that was obtained by a statistical model fit to different particle yields. The effective temperatures of various particle species, obtained in previous analyses, suggest a systematic rise with increasing particle mass, which is confirmed by the deuteron results.
An explanation can be the influence of a collective expansion with a radial expansion velocity β_r. By fitting a *Siemens-Rasmussen* function to the transverse mass spectra, the global temperature of $T = (100 \pm 8)$ MeV and radial expansion velocity $\beta_r = 0.37 \pm 0.01$ are obtained. This temperature is still very high and only takes into account the production of deuteron nuclei.
The simultaneous fit of a *blast-wave* function to the transverse mass spectra of deuterons and other particles, as obtained by previous analyses, considers a velocity profile for the radial expansion velocity and takes into account the production of various particle species. The resulting global temperature $T_{kin} = (68 \pm 1)$ MeV and average transverse expansion velocity $\langle\beta_r\rangle = 0.341 \pm 0.003$ are within the expected range for the collision energy.
The Siemens-Rasmussen fits are also used to extrapolate the transverse mass spectra into unmeasured regions, to integrate them and obtain a rapidity-dependent count rate. This count rate exhibits a thermal shape for central events and shows increasing spectator contributions for more peripheral events.
The invariant yield spectra of the deuterons are compared to those of protons, as obtained by a previous analysis, in the context of a *nucleon coalescence model*. The hereby extracted nucleon coalescence factor $B_2 = (4.6 \pm 0.1) \times 10^{-3}$ agrees with the expected result for the beam energy that was studied.

Inhaltsangabe

In April und Mai 2012 maß das an der GSI *Helmholtzzentrum für Schwerionenforschung* Anlage gelegene High Acceptance Di-Electron Spectrometer (HADES)-Experiment Daten bei der Kollision von Au+Au mit einer Strahlenergie von $E_{kin} = 1.23A$.
In der vorliegenden Arbeit ist die Produktion von Deuteronen in diesem Kollisionssystem untersucht.
Eine Gesamtzahl von 2.1×10^9 Au+Au events, welche die zentralsten 40% der Kollisionen enthält, wurde ausgewählt. Nach einer Teilchenidentifikation, welche auf einer Massenbestimmung an Hand von Flugzeit und Impuls sowie einer Messung des Energieverlustes basiert, wurden die transversalen Massenspektren der Deuteronen fr verschiedene Rapiditäten extrahiert und anschließend auf Akzeptanz und Effizienz korrigiert.
Der inverse Steigungsparameter von Boltzmann fits, welche an die transversalen Massenspektren bei Schwerpunktsrapidität angepasst wurden, und der als *effektive Temperatur* bezeichnet wird, wurde extrahiert. Im Falle einer statischen, thermischen Quelle entspricht dieser Parameter der kinetischen Ausfriertemperatur T_{kin} und sollte aus diesem Grund niedriger oder gleich der chemischen Ausfriertemperatur T_{chem} sein. Die erhaltene effektive Temperatur $T_{eff} = (190 \pm 10)$ MeV übersteigt jedoch die chemische Ausfriertemperatur, die durch das Anpassen eines statistischen Modells an verschiedene Teilchenerträge bestimmt wurde. Die effektive Temperatur verschiedener Teilchenspezien, wie sie in vorangehenden Analysen bestimmt wurden, suggerieren einen systematischen Anstieg mit steigender Teilchenmasse, was von den Deuteronergebnissen bestätigt wird.
Eine Erklärung kann der Einfluss einer kollektiven Expansion mit radialer Expansionsgeschwindigkeit β_r liefern. Durch das Anpassen einer *Siemens-Rasmussen* Funktion an die transversalen Massenspektren, wurden die globale Temperatur $T = (100 \pm 8)$ MeV und radiale Expansionsgeschwindigkeit $\beta_r = 0.37 \pm 0.01$ bestimmt. Diese Temperatur ist immernoch sehr hoch und berücksichtigt nur die Produktion der Deuteron-Nuklide.
Das simultane Anpassen einer *blast-wave* Funktion an die transversalen Massenspektren der Deuteronen und der anderer Teilchen, bestimmt in vorangehenden Anaylsen, berücksichtigt ein Geschwindigkeitsprofil der radialen Expansionsgeschwindigkeit und die Produktion verschiedener Teilchenspezies. Die resultierende globale Temperatur $T_{kin} = (68 \pm 1)$ MeV und durchschnittliche transversale Expansionsgeschwindigkeit $\langle \beta_r \rangle = 0.341 \pm 0.003$ sind im erwarteten Rahmen für die betrachtete Kollisionsenergie.
Die Siemens-Rasmussen Funktionen wurden zudem verwendet, um die transversalen Massenspektren in ungemessene Regionen zu extrapolieren, um sie anschließend zu integrieren und eine Zählrate in Abhängigkeit der Rapidität zu erhalten. Diese Zählrate weist für zentrale Kollisionen eine thermale Form auf und zeigt wachsende Spektatorenbeiträge für peripherere Events.
Die invarianten Spektren der Deuteronen wurden im Kontext eines *Nukleonen Koaleszenz Modells* mit denen von Protonen verglichen, wie sie in einer vorangegangenen Analyse bestimmt wurden. Der hierbei erhaltene Nukleonen Koaleszens Parameter $B_2 = (4.6 \pm 0.1) \times 10^{-3}$ stimmt mit dem erwarteten Ergebnis für die betrachtete Strahlenergie überein.

Table of Contents

1 Introduction and Motivation

The *origin of elements* is one of the core fields of interest for modern science. Having been the subject of philosophy and theology since the early times, scientific methods to investigate the formation of matter have been developed during the last few decades.
A key event is the birth of the universe during what is commonly known as the *Big Bang*, approximately 13.8×10^9 years ago.
After this creation, the universe was in a state of free *quarks and gluons*, the so-called *Quark-Gluon-Plasma (QGP)*. After 10^{-5} seconds, while the system rapidly cooled down, the quarks and gluons formed the earliest *hadrons* in the form of nucleons and mesons. Following a further decrease in temperature, minutes after the creation, these nucleons bound as the first nuclei, which then became the foundation for the creation of atoms.
As the formation of a QGP occurred only under extreme temperatures of approximately 10^{32} K during timescales of microseconds it is very difficult to recreate it in a laboratory. In modern experiments the collisions of nucleons at high energies, using a heavy-ion accelerator, are able to produce a QGP [1]. However, their properties are still very short-lived and can not be directly observed. Indirect probes, like hadrons, lepton pairs or photons produced in the collision have to be studied in order to gain an insight into the properties of the medium.
Most observations concerning matter obtained by experiments can be described by the assumptions made by the *standard model* about the structure and interaction of matter, as shown in Fig. 1.1. It groups elementary particles in two categories: (Anti-)quarks and (Anti-)leptons that can be summarized in three generations. All stable matter on earth is made up of first generation particles. Quarks are characterized by their mass and the quantum numbers *spin* and *charge*. In each generation a quark with charge $-1/3$ and one quark with charge $2/3$ exist. For higher generations the masses of the quarks increase.
Leptons have whole numbered charges and can be differentiated into charged electrons, myons and tauons and uncharged corresponding neutrinos.
Also categorized by the standard model are three fundamental forces between these particles that vary in strength and range: The weak force, the strong force and the electromagnetic force. These forces are transmitted by force-carrying gauge bosons. The gluon transmits the strong force, the photon the electromagnetic and $W^{\pm}$ and Z bosons the weak interaction. Only the fourth fundamental force, the *gravitational force*, although believed to be carried by a yet undiscovered *graviton*, can not be described by the standard model.
The recently found scalar *Higgs boson* [2] carries out the interaction between particles and the Higgs field, which generates the particle's masses.
While quarks are subject to electromagnetic, weak and strong interactions, charged leptons are only influenced by electromagnetic and weak forces and the uncharged myons only interact weakly.
According to *Quantum Chromodynamic (QCD)* calculations, quarks, which can only occur in bound states due to the so-called *confinement*, carry an additional charge, the *color charge*. The bound states of quarks, so called *hadrons*, can only exist in colour-neutral combinations.

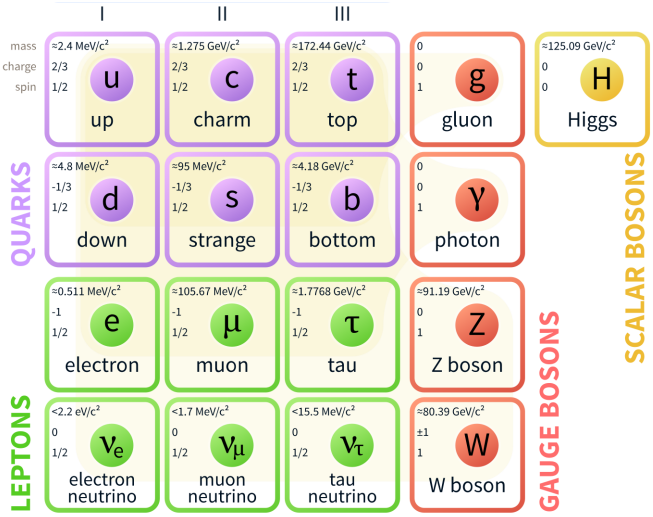

Figure 1.1: Standard model of nuclear particle physics. Includes quarks (purple) and leptons (green) in three generations, with their corresponding mass, charge and spin. Also pictured are the gauge bosons (red), that mediate the interactions and the Higgs boson. Taken from [3].

1.1 The Phase Diagram of Nuclear Matter

Phase diagrams contain information about the state and transition between phases of matter. Fig. 1.2 shows the phase diagram of nuclear matter, depending on the temperature T and the baryo-chemical potential μ_B. The baryo-chemical potential corresponds to the amount of energy that is needed to add or subtract a baryon respectively to or from the current system.
As indicated in the diagram, stable nuclei as a bound state of quarks exist at temperatures around $T = 0$ MeV.
According to the *MIT bag model* each nucleon can be considered as a bag of partons, which they can not escape from [4]. The quarks are *confined*. After an increase of temperature and/or the baryo-chemical potential above the phase boundary, hadrons begin to overlap and the rapid movements caused by the increase in temperature cause them to be *deconfined*. A Quark-Gluon-Plasma is formed. The $< q\bar{q} >$ condensate is the order parameter of the chiral symmetry, which is fully restored in a QGP [5].
These conditions are reproduced in laboratory experiments using heavy-ion collisions. The temperature and baryo-chemical potential that can be reached thereby depend on the bombarding energy and size of the collision system (number of nucleons in the colliding nuclei). The high energy collisions of Au+Au collisions that were observed with HADES in 2012 and are analyzed in this thesis, originate from the *Schwerionensynchrotron 18 (SIS18)* energy, that is marked in the diagram.
For low μ_B a smooth liquid-gas transition between the phases is observed while for higher net-baryon densities a phase transition of first order is expected,a *critical point* must exist [6]. Currently, the *Beam Energy Scan at the Relativistic Heavy-Ion Collider (RHIC)* is searching for the critical point as the exact temperature and μ_B is still unknown.

In the region labeled as *Color Super conductor*, attractive forces between two quarks are

[1]Schwerionensynchrotron
[2]Alternating Gradient Synchrotron
[3]Super Proton Synchrotron
[4]Relativistic Heavy-Ion Collider

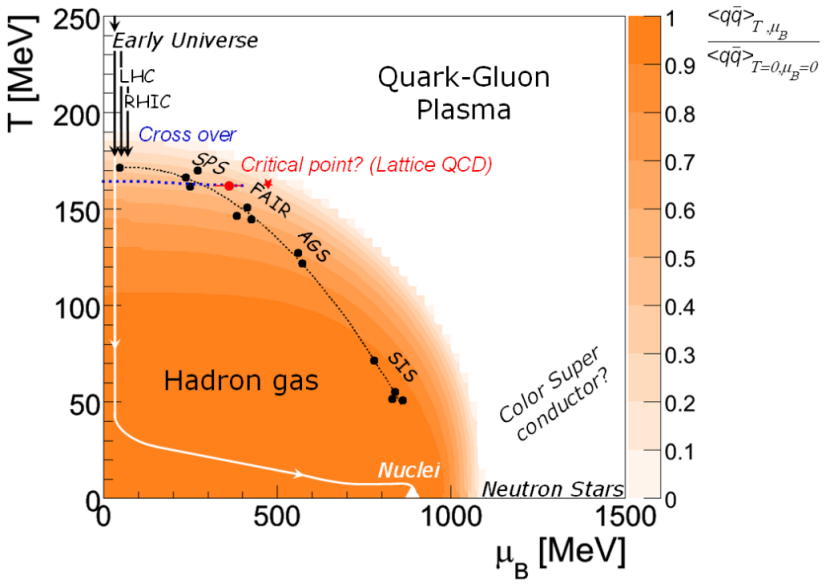

Figure 1.2: Schematic picture of the phase diagram of nuclear matter. The black freeze-out points were calculated by an statistical model fit (See chapter 1.3.1) to the particle yields measured in heavy-ion collisions at SIS [1] , AGS[2] , SPS[3] and RHIC[4] energies. The color on the z-axis codes the strength of the quark-antiquark condensate. Also indicated is the critical point (red) and the process during the formation of stable nuclei (white path). Taken from [7].

expected to cause them to form *cooper pairs* (their spins cancel out and add up to 0) [8]. As this region of extreme high net-baryon densities can not be reached by experiments, the effect has not yet been observed.

1.2 Introduction to Heavy-Ion Collisions

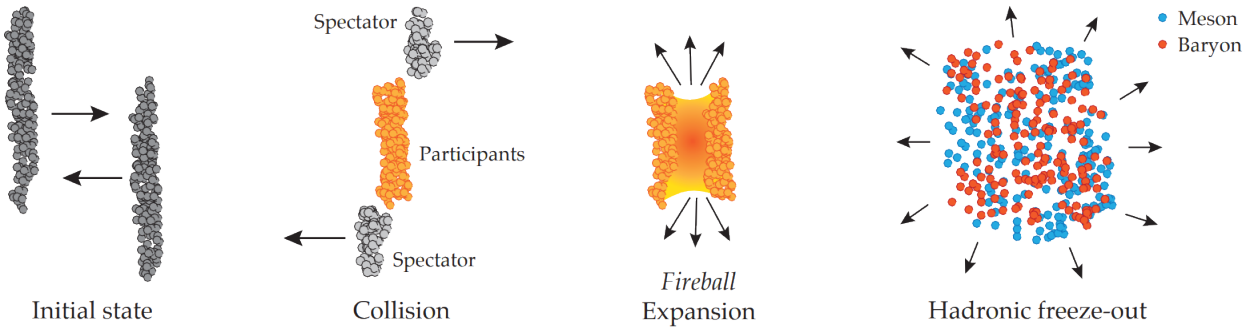

Figure 1.3: Stages during a heavy-ion collision. Taken from [9].

In *Heavy-Ion Collisions (HIC)*, the kinetic energies of two accelerated nuclei are mainly converted to high compression energies and temperatures. Therefore, they provide the possibility to map out regions of the phase diagram as explained in the previous chapter.
Fig. 1.3 shows the different stages during the collision of heavy ions at relativistic energies.
The **collision** phase is mainly characterized by its geometric properties, namely the *impact parameter* b, which corresponds to the distance between the centers of the colliding nuclei, and the *event-plane* which is defined as their angular orientation towards each other. The nucleons are distinguished into *participants* that are directly colliding and *spectators*, which do not geometrically overlap with the nucleons of the incident nuclei.
During the **fireball expansion** which is reached after approximately 3×10^{-24} s, the hot and dense medium, that is referred to as *fireball*, which was created by the participants during the collision, expands and begins to cool down.
The following **hadronic freeze-out** occurs as the temperature reaches the *chemical freeze-out* temperature T_{chem}. Below this temperature no further *inelastic* collisions take place and the particle abundances are fixed.
As the system continuously cools down, the *kinetic freeze-out* temperature T_{kin} is reached and no more elastic collisions occur.
By studying the transverse mass spectra of particles produced during the collision, as done with deuterons in this thesis, information about the kinetic freeze-out characteristics of the system can be gained.

1.2.1 Production of Deuterons

During HIC, large quantities of particles of various species are produced.
Deuterons, which are the lightly bound pair of a proton and neutron with a binding energy of $E_{bind} \approx 2.2$ MeV can not survive the conditions that prevail during a heavy-ion collision. Therefore, their production is more likely to occur during the freeze-out phase, following the expansion of the system.

Nucleon Coalescence Model

A simple assumption to understand cluster formation, first described by S. T. Butler & C. A. Pearson [10] is, that heavier nuclei are formed by *coalescence* of protons and neutrons close enough in phase space. Because the deuteron is only capable of absorbing a small amount of recoil, the two nucleons must have a small relative momentum.

The probability that a number of A close nucleons, which are scattered randomly throughout the nuclear volume, coalesce is described by the parameter B_A, which depends on the fireball size and dynamics. It can be derived by comparing the invariant yield of the light nuclei to the invariant yield of the coalescing nucleons [11]:

$$E_A \frac{\mathrm{d}^3 N_A}{\mathrm{d}p_A^3} = B_A \left[\left(E_P \frac{\mathrm{d}^3 N_p}{\mathrm{d}p_p^3} \right)^Z \left(E_n \frac{\mathrm{d}^3 N_n}{\mathrm{d}p_n^3} \right)^N \right]_{p_p = p_n = p_A/A} . \tag{1}$$

Where p is the particle's momentum and E the energy of the particle.

As it is not possible to measure neutrons with the HADES setup, it is for simplification reasons assumed that the distributions of neutrons and protons are identical. Therefore the invariant yield of the light nuclei is compared to that of protons to the power of A.

$$E_A \frac{\mathrm{d}^3 N_A}{\mathrm{d}p_A^3} = B_A \left(E_P \frac{\mathrm{d}^3 N_p}{\mathrm{d}p_p^3} \right)^A_{p_p = p_A/A} . \tag{2}$$

This can be rewritten as a function of the rapidity y and the transverse momentum p_t [12]:

$$\frac{1}{2\pi(p_t/A)} \frac{\mathrm{d}^2 N_A}{\mathrm{d}y_{cm}\mathrm{d}(p_t/A)} = B_A \left[\frac{1}{2\pi p_t} \frac{\mathrm{d}^2 N_p}{\mathrm{d}y_{cm}\mathrm{d}p_t} \right]^A , \tag{3}$$

where y_{cm} is the respective center-of-mass rapidity y_{cm}. The Lorentz-invariant transverse momentum $p_t = \sqrt{p_x^2 + p_y^2}$ can also be directly related to the transverse mass m_t as:

$$p_t = \sqrt{m_t^2 - m_0^2}, \tag{4}$$

where m_0 is the particle rest mass.

As the main focus of this thesis is the study of deuteron production, the coalescence factor B_2, associating the occurence of a proton-neutron pair to deuteron formation, will be further investigated and compared to previous experiments in chapter 5.3.

1.2.2 Radial Flow

After the collision of two heavy nuclei at high energies, collective expansion effects, superimposed on the thermal motion of the particles, can be observed. These effects are known as *flow*. Generally, a distinction between *isotropic* (uniform in all directions) and *anisotropic* flow is made.

For collisions with low impact parameters b (*central collisions*), the produced particles are emitted with a radial symmetry.

After *peripheral collisions* with higher impact parameters, the geometrical asymmetry of the fireball causes the anisotropic contributions to the particle's transverse momentum spectra to increase.

In this thesis only the radial contributions will be studied, as they influence the transverse mass spectra of the produced particles.

An ansatz to describe them and extract the freeze-out characteristics is made with a *Boltzmann* function:

$$\frac{dN}{dydp_t} \propto \exp\left(\frac{E}{k_b T_B}\right). \tag{5}$$

In a purely thermal system, the inverse slope parameter T_B of the Boltzmann function is the Boltzmann temperature T_B, which, at mid-rapidity corresponds to the *kinetic freeze-out* temperature of the system T_{kin}. Due to radial flow effects, a pure temperature can not be measured in the experiments and the *effective temperature* T_{eff} is introduced to correspond to T_B at mid-rapidity.
Fig. 1.5 shows the effective temperature for different particle species measured with HADES. The data exhibits a trend of increasing effective temperature with increasing particle mass. This can be explained by the radial expansion of the hot and dense medium. Due to the high pressure of the fireball, the emitted particles experience a push in radial direction. Hence, the effective temperature can be approximated with a function of the particle mass and expansion velocity β_r:

$$T_{Eff} = \frac{1}{2} m \beta_r^2 + T_{kin} \tag{6}$$

It is now possible to extract the kinetic freeze-out temperature T_{kin} and radial-flow velocity β_r from the fit, which characterize the fireball at thermal freeze-out.

A way to describe the transverse mass spectra including radial flow effects is the *Siemens-Rasmussen* ansatz:

$$\frac{1}{m_t^2}\frac{d^2N}{dm_t dy} \propto \cosh(y)\exp(\frac{-\gamma_r E}{T})\left[\left(\gamma_r + \frac{T}{E}\right)\frac{\sinh(\alpha)}{\alpha} - \frac{T\cosh(\alpha)}{E}\right] \tag{7}$$

where $\gamma_r = 1/\sqrt{1-\beta_r^2}$, $\alpha = (\gamma_r \beta_r p)/T$ and E, p and y are the total energy, momentum and rapidity of the considered particle in the center-of-mass system [13]. In this model, β_r represents a constant expansion velocity.

Considering the additional assumption of differing velocities for particles at different positions within the expanding medium, the *blast-wave* ansatz utilizes a transverse velocity profile [14]. After decoupling from the thermal system, the differential cross section of a particle species is given by:

$$\frac{1}{m_t}\frac{d^2N}{dm_t dy} \propto \int_0^R m_t K_1\left(\frac{m_t\cosh(\rho)}{T}\right) I_0\left(\frac{p_t\sinh(\rho)}{T}\right) r dr. \tag{8}$$

K_1 and I_0 are the modified *Bessel* functions, r the radial distance from the center of the fireball, R the radius of the fireball and $\rho = \tanh^{-1}\beta = \tanh^{-1}(\beta_S (r/R)^n)$, which is correlated to the transverse velocity β_S at the surface. The exponent n can be chosen to characterize the velocity profile of the expansion.

1.3 Previous Experiments in the SIS18 Energy Regime

1.3.1 HADES

The High Acceptance Di-Electron Spectrometer (HADES) is located at the GSI, *Helmholtzzentrum für Schwerionenforschung* facility in Darmstadt. Its detector components will be explained in detail in chapter 2.

In 2005, collisions of incident Ar ions on a KCl target with a beam energy of 1.76A GeV have been recorded. For this collision system, the production of light nuclei has been studied in [15]. By fitting a function according to Eq. 6 to the effective temperatures of different particle species, the parameters $T_{kin} = (74.7 \pm 5.8)$ MeV und $\beta_r = 0,37 \pm 0,13$ were extracted from the Ar+KCl data [15]. They will be compared to the new results of a heavier system at lower energies.
The Au+Au collisions at 1.23A GeV, that were measured in April an May 2012 and will be further analyzed in this thesis, represent the heaviest collision system that has been studied in the experiment. More specific information can be found in chapter 2.1.
Proton freeze-out characteristics have been studied for Au+Au collisions in [16]. By fitting *Siemens-Rasmussen* functions to their transverse mass spectra, as described in chapter 1.2.2, their kinetic freeze out temperature and the radial expansion velocity were determined. They were found to be $T = (70 \pm 4)$ MeV and $\beta_r = 0.41 \pm 0.01$ and can in this thesis be compared to the characteristics obtained from the deuteron spectra. The heavier particles are expected to be stronger affected by radial flow effects [17].
The yield of protons and other particle species was compared to the fit with a *Statistical Hadronization Model (SHM)*. SHM consider a macroscopic description of a homogeneous thermal source, as averaged over statistical ensembles. Particle numbers are assumed to depend solely on statistical factors as the system enters a state of chemical equilibrium. The predictions of the thermal model are thereby not limited to hadron mulitplicities, but can also be applied to the yields of composite particles [18].
Relevant parameters are the temperature T, the volume V and the chemical potentials μ_b (baryon-chemical potential), μ_S (strangeness chemical potential) and μ_Q (charge chemical potential) for each hadron, which makes it possible to characterize the particle emitting medium. μ_S and μ_Q are usually constrained by initial conditions [19].
Fig. 1.4 shows the measured yields of different particle species, compared to the yields that were obtained by a SHM fit. From the fit, the freeze-out parameters $T = (68 \pm 2)$ MeV and $\mu_B = (883 \pm 25)$ MeV were extracted. It can be seen that the measured data is in good agreement with the fit (χ^2/(degrees of freedom) = 2.3).
In Fig. 1.5, the effective temperature, obtained by analyzing the Boltzmann temperature at mid-rapidity, is shown for different particle species as a function of the particle mass. The systematic rise in effective temperature with increasing particle mass, as explained in chapter 1.2.2, can be observed in the data. By fitting a function according to Eq. 6 to the data, the parameters $T_{kin} = (71.5 \pm 4.2)$ MeV and $\beta_r = (0.28 \pm 0.09)$ were extracted.
Simultaneous fitting of the proton's transverse mass spectra with Siemens-Rasmussen functions (Eq. 7) resulted in the parameters $T_{kin}^{SR} = (70 \pm 4)$ MeV and $\beta_r^{SR} = 0.43 \pm 0.01$ which are consistent with the results of the linear fit to the effective temperatures.

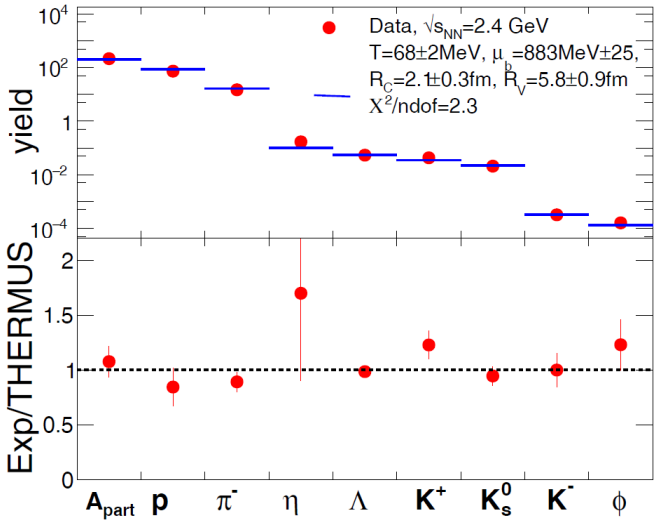

Figure 1.4: Comparison of measured particle yields (red dots) to a SHM fit (blue lines). The lower plot shows the ratios of the data to the fit. Also indicated are the fit parameters T, μ and the radius of the fireball R_V and the strangeness canonical suppression radious R_C in the right upper corner. Taken from [16].

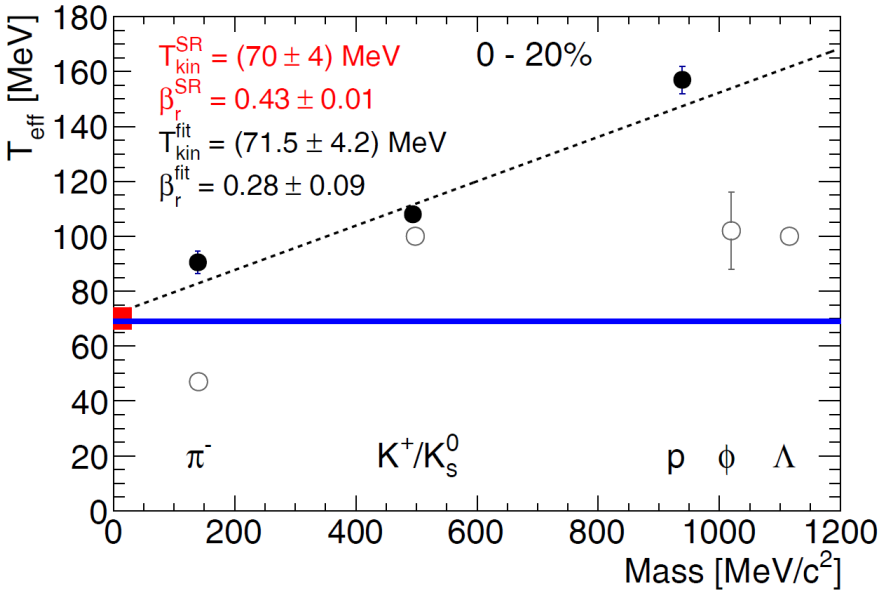

Figure 1.5: Effective temperature T_{eff} for different particle species as function of their mass for the 0-20% most central events in Au+Au collisions at 1.23A GeV. Also indicated is the chemical freeze-out temperature $T_{chem} = (69 \pm 1)$ MeV (blue line) from a SHM fit to the measured particle yields , a linear fit (dotted line), according to Eq. 6 and the resulting fit parameters T_{kin}^{fit} and β_r^{fit}. T_{kin}^{SR} (also indicated by a red marking on the y-axis) and β_r^{SR} are obtained by a simultaneous Siemens-Rasmussen fit to the transverse mass spectra of protons. Taken from [16].

1.3.2 FOPI

The *FOPI* experiment was installed at the SIS18 accelerator at the GSI facility in Darmstadt. Its name is a reference to its large acceptance, because it covers nearly the full solid 4π ("**fo**ur **pi**") angle. In 1996, the collision system ^{69}Ru+^{96}Ru was studied at beam energies of $0.4A$ and $1.528A$ GeV. For this collision system, the freeze-out characteristics have been analyzed and the fragment formation by nucleon coalescence investigated , using p,d,t,^{3}He and ^{4}He [20]. The results of the kinematic analysis are shown in Fig. 1.6. They exhibit a trend of increasing mean kinetic energies $\langle E_{kin} \rangle$ with increasing particle mass for both energies. This leads to the assumption of a radial flow velocity β_F, which is obtained by a fit to the data with:

$$\langle E_{kin} \rangle = \frac{1}{2} m_0 \langle \beta_F \rangle^2 m + \frac{3}{2} T. \tag{9}$$

Fig. 1.7 pictures the results for the nucleon coalescence parameter B_A as a function of the normalized rapidity $y^{(0)} = \frac{y_{lab}}{y_{cm}} - 1$. The values of the coalescence parameters decrease with the beam energy. They are observed to be almost independent of the rapidity around mid-rapidity.

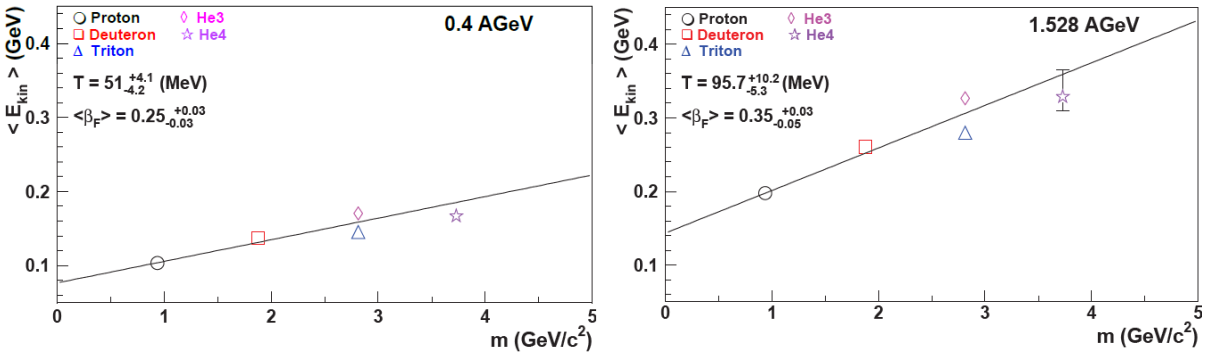

Figure 1.6: Mean kinetic energies of light fragments for most central events, measured with FOPI at $0.4A$ GeV (left) and $1.528A$ GeV (right). Also included are linear fits to the data to extract the freeze-out parameters T and $\langle \beta_F \rangle$. Taken from [20]

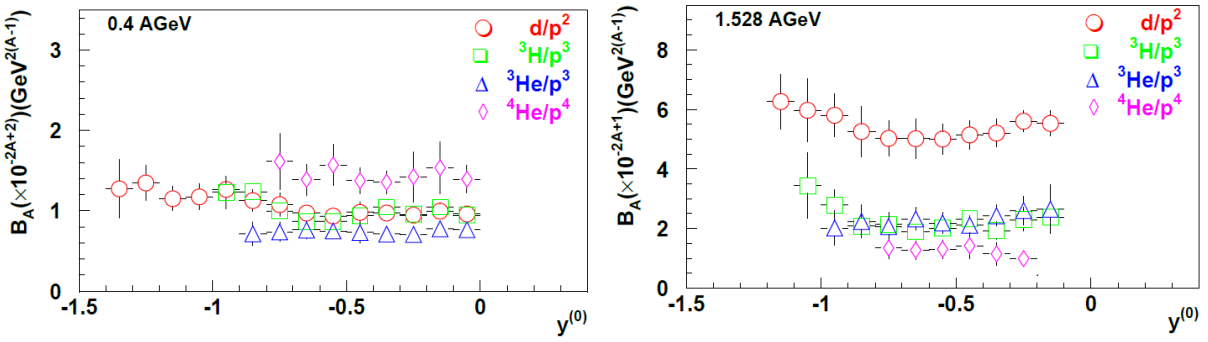

Figure 1.7: Coalescence parameter B_A for multiple nuclei, as estimated by the coalescence model for most central Ru+Ru collisions at $0.4A$ GeV as a function of normalized rapidity $y^{(0)}$ (left) and $1.528A$ GeV (right). Taken from [20].

1.4 Structure of this Thesis

In this thesis, the Au+Au data measured with the HADES detector at 1.23A GeV in 2012 will be analyzed. The aim is to study deuterons, originating from the the freeze-out of the hot and dense medium, as they can provide information about its characteristics.
After the reconstruction of the measured deuterons, which will be explained in chapter 3.1.4, their transverse mass spectra are studied. From these spectra, information about the freeze-out in form of the kinetic freeze-out temperature T_{kin} and characteristics of the radial flow in form of the radial expansion velocity β_r can be derived.
Because of their higher mass, deuterons can confirm the trend of increasing T_{eff} for increasing masses, as pictured in Fig. 1.5 with good leverage.
Fits to the data with Siemens-Rasmussen functions are used to extrapolate the transverse mass spectra to unmeasured m_t regions and integrate the yield for various rapidities in order to obtain a rapidity density distribution.
The extracted freeze-out parameters are afterwards discussed in the context of the results from other experiments.
The nucleon coalescence parameter B_2 will be determined and also be compared to the trend, as measured by other experiments.

2 The HADES Experiment

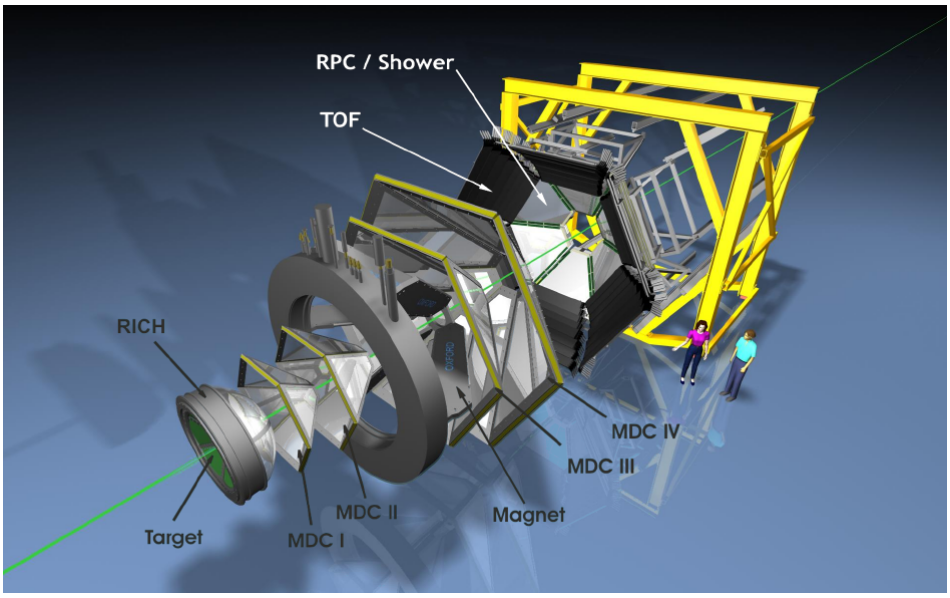

Figure 2.1: Expanded view of the HADES detector. The different components are labeled.

The High Acceptance Di-Electron Spectrometer (HADES) at the GSI *Helmholtzzentrum für Schwerionenforschung* facility in Darmstadt, Germany is a fixed target experiment, which was developed to study electron-positron pairs originating from the decays of light vector mesons like ρ, ϕ and ω, produced in proton- and heavy-ion collisions. These vector mesons were chosen as probes of the collision because they do not interact strongly and can therefore carry unaltered information about the medium [21].
The detector covers a polar angle of $18° < \Theta < 85°$ and features an azimuthal acceptance of 85%.
In order to record the high multiplicities of particles produced in heavy-ion collisions, the detector's data acquisition (DAQ) can record hits with a frequency of 10^8 Hz.
The HADES detector is made up of 6 sectors in a hexagonal structure, one of which is pictured schematically in Fig. 2.2.
A START detector, located closely before the target, provides a start time while a VETO detector behind it excludes reactions which did not occur within the target.
To differentiate electrons and positrons from other particles, a *Ring Imaging Cherenkov Detector (RICH)* and the pre-shower wall are used. Reconstructing the tracks of particles that are passing through the detector is done by a magnetic spectrometer, which consists of 4 planes of *Mini Drift Chambers (MDC)*, of which two are placed before the *Ironless Super Conducting Electromagnet (ILSE)* and two behind it.
The time-of-flight measurements for small polar angles between $18 - 45°$ are done by a *Resistive Plate Chamber (RPC*, and for larger angles between $44 - 85°$ conducted by a *time-of-flight (TOF)* wall of scintillators.
The *forward wall* further downstream the beamline is used to detect spectators and classify the centrality of the studied event.

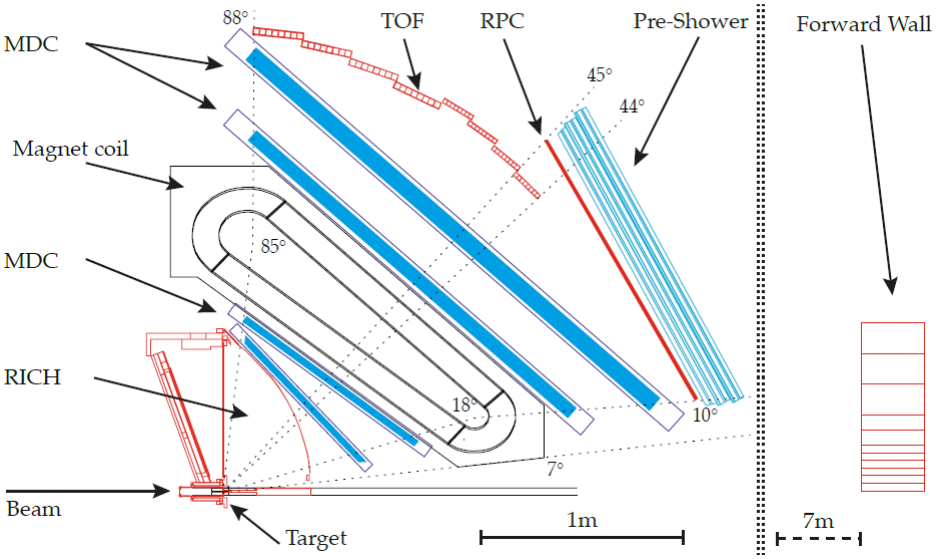

Figure 2.2: Schematic overview of one HADES sector, showing the detector components: A RICH detector surrounding the target, two planes of mini drift-chambers (MDC) before and after the super conducting magnet, the time-of-flight scintillators (TOF), resistive plate chambers (RPC) and a pre-shower detector. 7m further along the beam axis, the forward wall is placed. Taken from [9].

2.1 Beam and Target

The heavy-ion beam, used for the Au+Au collisions at 1.23A GeV with the HADES experiment in April and May 2012, is produced by the *SchwerIonen Synchrotron 18* (SIS18). The 18 indicates a magnetic rigidity of $B \times \rho = 18$ Tm, where B is the magnetic field strength and ρ the radius of the curvature of the beam. The maximum kinetic energy that can be reached depends on the accelerated ion. Protons can reach up to 4.5 GeV, while the Au ions used in the April and May beam time are limited by 1.25A GeV.
The target used during the beam time was a fifteen-fold segmented gold foil. The segmentation was chosen in order to reduce multiple scattering effects. Each foil was 25 μm thick, 2.2 mm in radius and located in a distance of 4.5 mm from the next segment, glued on a Kapton foil. The target, as shown in Fig. 2.3, was placed in an evacuated tube.

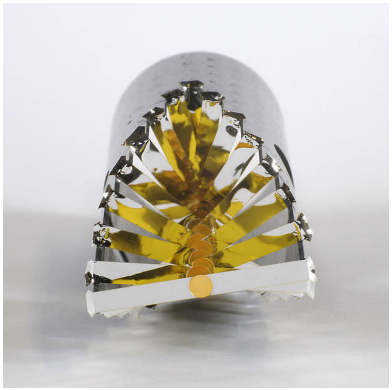

Figure 2.3: Segmented Gold target from the beam time in 2012. Taken from [22].

2.2 Ring Imaging Cherenkov Detector

For lepton identification with the HADES detector, a **R**ing **I**maging **Ch**erenkov (RICH) detector is used, that is filled with a C_4F_10 gas.
If a charged particle with velocity v passes through a medium, exceeding the speed of light in the medium $c' = c_0/n$, where n is the refraction index of the medium, dipol radiation causes the emission of a cone of photons [23].
The opening angle Θ of this cone depends on the medium's refraction index n and the particle's relative velocity $\beta = v/c$:

$$\cos(\Theta) = \frac{1}{\beta n}. \tag{10}$$

Because of the choice of C_4F_10 gas with a refraction index of $n = 1.00151$, only very light particles like electrons (0.51 MeV/c^2) with momentum between 0.1 GeV/$c < p <$ 1.5 GeV/c emit these radiation. Heavier particles like hadrons will, at SIS18 energies, not reach the *Cherenkov threshhold* and the detector is *hadron blind*.
As pictured in Fig. 2.4, the RICH detector consists of a gas filled volume in which Cherenkov radiation is induced by passing leptons. The emitted photons are then reflected by a *VUV-mirror* onto a plane of photon detectors which reconstruct the characteristic rings.

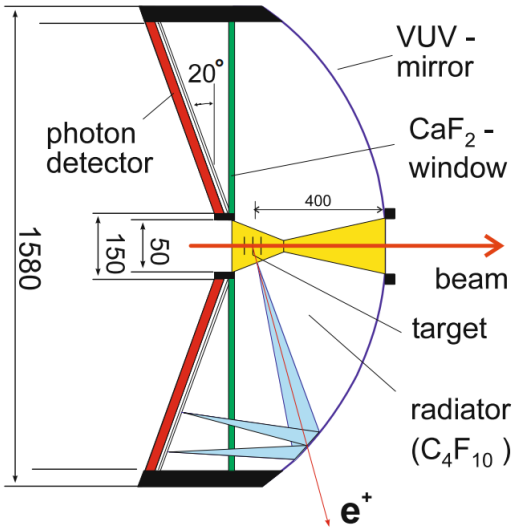

Figure 2.4: Schematic overview of the RICH detector. A lepton with high enough energy creates multiple photons, which are reflected by the VUV-mirror and recorded by the photon detectors. All lengths in mm. Taken from [24].

2.3 Tracking System

The magnet spectrometer used for particle tracking consists of the **M**ini **D**rift **C**hambers (MDC) and the **I**ron**L**ess **S**uperconducting **E**lectromagnet (ILSE).
Two planes of MDCs are located in front of the magnet and two behind it, in order to identify *tracklets* before and after the deflection that a charged particle experiences in a magnetic field.

2.3.1 Magnet

The superconducting magnet ILSE, pictured in Fig.2.5, consists of 6 NbTi-coils. It creates a toroidal magnetic field with a maximum intensity of 3.7 T on the coil surfaces and an intensity of 0.8 T in the center of an MDC which quickly decreases with further distance [25]. The magnetic field geometry was chosen in a way to have minimal strength around the target and in RICH, MDC and TOF/RPC.
The magnet is cooled down to 4.6 K by liquid helium to reach superconductivity.
Charged particles, passing through the magnetic field, are subject to a *kick*, that deflects positively charged particles towards the beam axis and negatively charged particles outwards.

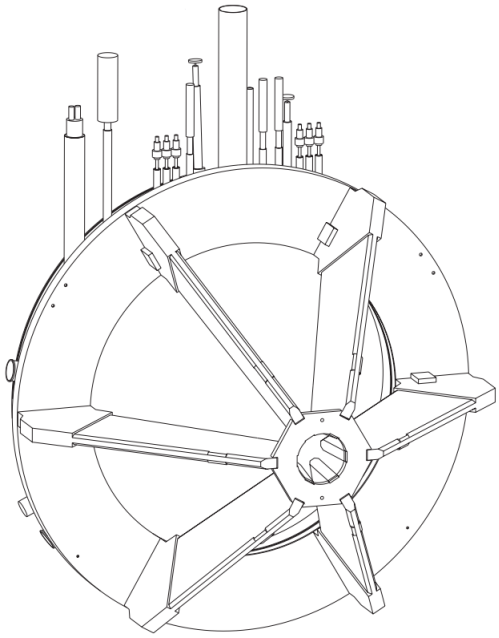

Figure 2.5: Technical drawing of the ironless, superconducting electromagnet ILSE. Also indicated are the power and gas supplies on top of the magnet. Taken from [25].

2.3.2 Mini Drift Chambers

24 **M**ini **D**rift **C**hambers (MDC) are installed in the HADES setup, divided in 4 planes over the 6 sectors of the spectrometer. They are used to reconstruct the tracks of passing charged particles.
Each drift chamber consists of 1100 wires, distributed in 6 layers of read-out wires, separated by cathode wires. Their relative orientation towards each other is pictured in Fig. 2.6 ($\pm 40°, \pm 20°, 0°$). The smallest sensitive unit, a mini drift cell, is made up of one gold coated wolfram signal wire surrounded by two aluminum potential wires and multiple cathodes wires. During the Au+Au beam time, the first chamber was filled with a 70% Argon, 20% CO_2 mixture and the subsequent chambers with an 84% Argon, 16% Isobutane mixture. The CO_2 and isobutane component were introduced as a *photon quencher*. They absorb free photons in order to reduce background noise in the signal [26].
A charged particle, traversing the MDC with sufficient kinetic energy, ionizes the gas atoms along its track. The emitted electrons begin to drift within the cells along the potential field lines, created by potential and cathode wires. While they pass trough the cell towards the signal wire with an almost constant velocity, they ionize other atoms and thereby create an electron *avalanche*. Once the avalanche and ions reach the signal wire, they create a strong enough signal to be read out.

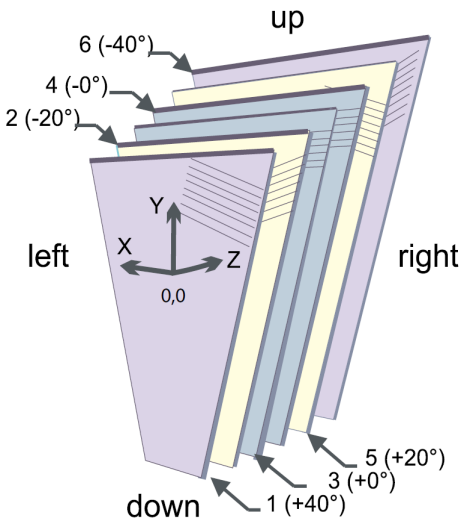

Figure 2.6: Schematic representation of the six anode wire planes in an MDC. They are orientated in a -40°, -20°, 0°, 0°, 20° and 40° angle with respect to each other. Taken from [24].

2.3.3 Track and Momentum Reconstruction

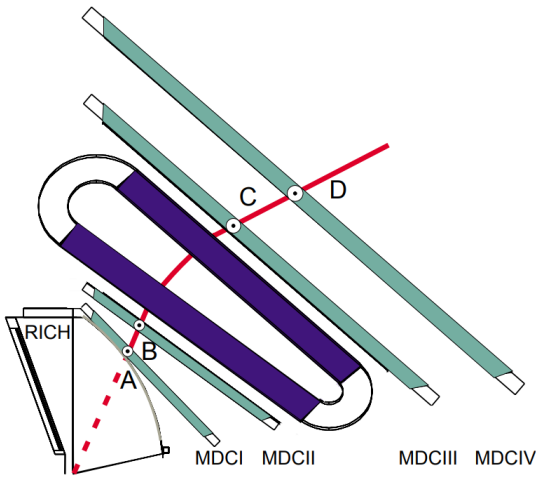

Figure 2.7: Schematic outline of the HADES tracking spectrometer. Two MDC planes are in front of the Magnet Coil (blue) and two behind it. A particle's track (red line) can be reconstructed by the four signals A,B,C and D, measured by the MDCs. Taken from [26].

When charged particles with kinetic energy pass through the magnetic field between the MDCs, they are subject to the *Lorentz force*. Their track is bend, whereby the curvature of the track depends on the particle's momentum.
Fig. 2.7 shows a schematic representation of the magnetic spectrometer. The hit points A, B, C and D, measured in the MDCs, can be used to calculate the *tracklets* $\overline{AB}$ and $\overline{CD}$. The angle between the tracklets and the known magnetic field intensity can then be used to calculate the particle's momentum.
Additionally, becauseof the gas within the chambers, the MDC data can be used to calculate a particle's *specific energy loss* (dE/dx) (See chapter 3.1.4).

2.4 Time-of-Flight Determination

Located behind the detectors used for track identification is the **M**ultiplicity and **E**lectron **T**rigger **A**rray (META) detector: a wall of scintillators at low polar angles ($18° - 45°$) and a ***R**esistive **P**late **C**hamber* (RPC) at higher polar angles ($44° - 85°$). In coincidence with the *START/VETO* counters in front of and behind the target, they are used for the *time-of-flight* calculations.

2.4.1 START/VETO Detector

A diamond *START* detector, placed a few millimeters before the target, provides the event start time t_0 for the time-of-flight calculations [27]. 70 cm further down the beamline, a *VETO* detector is placed. In coincidence with the signal from the START detector, the VETO detector can identify events that have not taken place within the target. The 4.7×4.7 mm wide START detector consists of 16 Cr stripes in x- and y direction of 50 nm thickness, mounted on a 150 μm diamond layer.
To minimize the effects of radiation damage, the detectors are mounted on plates which can be moved. Thus the beam, which only covers a part of of the surface, can be focused on nine different sections [28].

2.4.2 Resistive Plate Chambers

The RPC detector, covering polar angles $18° < \Theta < 45°$, is divided in six trapezoidal sections. The cross section of one chamber is shown in Fig. 2.8. Covered by a 2 mm Al shield, 3 layers of aluminum are stacked, separated by insulating glass layers. The 270 μm wide gaps between the planes are filled with a SF_6 and $C_2H_2F_4$ gas mixture [29]. To ensure stability, a plastic pressure plate is tightened by a screw. Insulation of the chamber is provided by three layers of Kapton coating.
A strong voltage of 5 kV is supplied to the center electrode, while the outer ones are grounded. If a charged particle passes through the cell with sufficient kinetic energy, it ionizes the gas atoms. The emitted electrons follow the electric field lines towards the anode plates and ionize further atoms as they are accelerated towards them. By this measurement, a time resolution of $\sigma_t = 80$ ps can be achieved.

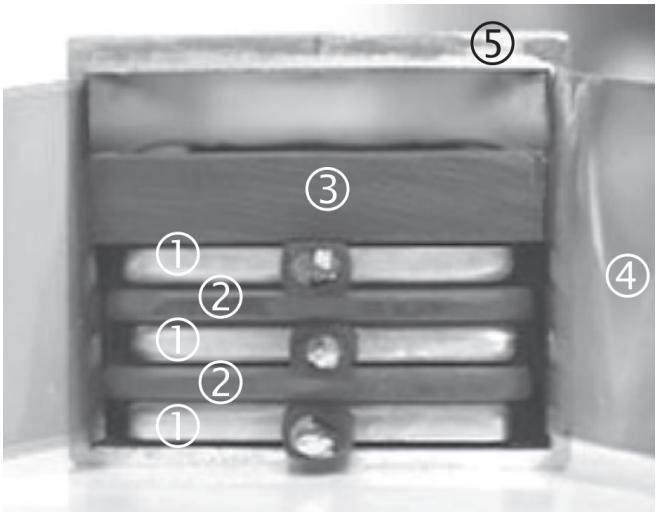

Figure 2.8: Cross Section of an RPC chamber: 1-Al electrodes, 2-glass electrodes, 3-plastic pressure plates, 4-kapton insulation, 5-2 mm thick Al shielding tube. Taken from [29].

2.4.3 Time-Of-Flight Detector

At higher polar angles $44° < \Theta < 85°$, the **T**ime-**O**f-**F**light (TOF) scintillators are installed. 384 polyvinyltoluene plastic scintillating rods are distributed in 48 modules over the 6 sectors. If a charged particle passes one of the rods, it excites the atoms of the material, which consequently emit photons while falling back to their initial state. The material used has a high light yield of ≈ 104 photons/MeV [30]. At both ends of the rods, **P**hoto **M**ultiplier **T**ubes (PMTs) are installed and detect the arrival times t_{left} and t_{right} and amplitudes a_{left} and a_{right} of the photons.
With the rod length L and the known group velocity v_g of light in the medium, the time of flight tof, the hit position x and the emitted light amplitude ΔE can be calculated:

$$\text{tof} = \frac{1}{2}\left(t_{\text{right}} + t_{\text{left}} - \frac{L}{v_g}\right) \tag{11}$$

$$x = \frac{1}{2}\left(t_{\text{right}} - t_{\text{left}}\right) \times v_g \tag{12}$$

$$\Delta E = k\sqrt{a_{\text{right}} a_{\text{left}} \exp\frac{1}{\lambda_{at}}} \tag{13}$$

where λ_{at} is the light attentuation length of the material (For the used plastic $\lambda_{at} = 210$ nm) and k a constant.
The achieved time resolution of the TOF detector is $\sigma_{\text{tof}} < 150$ ps and the spatial resolution $\sigma_x \approx 25$ mm.
The energy loss of particles in the TOF detector and their time-of-flight measurement can be used for identification purposes (See chapter 3.1.4).

2.4.4 Pre-Shower Detector

The Pre-Shower detector is divided in 6 sectors, which are located behind the RPC detectors. They were constructed to identify leptons by conversion showers. Fig. 2.9 shows a cross section of a Pre-Shower sector. Three 0.4 cm thick fiber-glass read-out planes are at the end of three gas chambers, filled with isobutane. In the chambers, alternating potential and ground wires are spanned. The chambers are separated by two Pb converter layers of different width. The

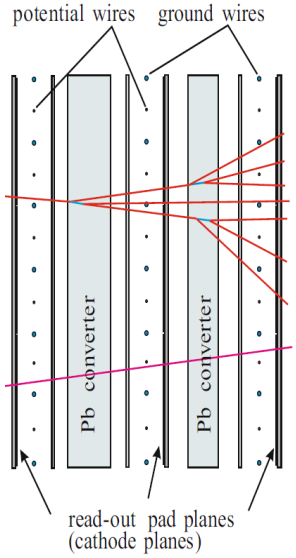

Figure 2.9: Schematic drawing of the Pre-Shower cross section. Pictured are two layers of lead converters between three planes of alternating potential and ground wires. Also indicated are the read-out cathode planes and two particle tracks: one lepton, performing a shower (Upper red track) and one hadron track (lower purple track). Taken from [24].

first layer has a width of $2x_0$ and the second $1x_0$, where $x_0 = 0.56$ cm is the radiation length of lead.
A charged particle with sufficient kinetic energy will excite the gas atoms and stimulate the emission of electrons, which are accelerated by the electric field. As they enter the lead converters, photons are produced via *bremsstrahlung* at the Pb atoms. After one radiation length, the photon decays into an electron-positron pair. Each of these again causes bremsstrahlung by interacting with the Pb atoms and thus two photons are created. This process is known as an *electromagnetic shower* and will continue until the energy loss during bremsstrahlung equals the ionization losses. The produced charged particles can then be measured at the read-out plane.
Hadrons do not produce as much bremsstrahlung (the production of bremsstrahlung scales with a factor $\approx 1/m^4$) and therefore don't create electromagnetic showers. Hence, the multiplicity of measured particles can be used to distinguish electrons and positrons from hadrons.

2.5 Forward Wall

In 2007, the *forward wall hodoscope* was installed approximately 7 m behind the target to investigate the event plane of the collision. The distance between the detector and forward wall is covered by a helium filled balloon, to reduce multiple scattering effects.
288 scintillation plates of increasing granularity are arranged around the beam axis in a 1.8×1.8 m wide setup. With this dimensions, it covers 7.3° of the polar angle.
Fig. 2.10 shows the layout of the scintillating detectors. The innermost 144 cells, next to the beam hole, have a surface of 4×4 cm^2, the next section is made up of 64 8×8 cm^2 wide cells, and the outermost scintillators are 16×16 cm^2 wide. This decrease of granularity towards the beam is due to the higher spectator multiplicities at smaller polar angles [31].
Behind each cell, PMTs are placed to measure the photons, that were created after the excitation of the scintillating atoms by charged particles, similar to the TOF detector (See chapter 2.4.3).

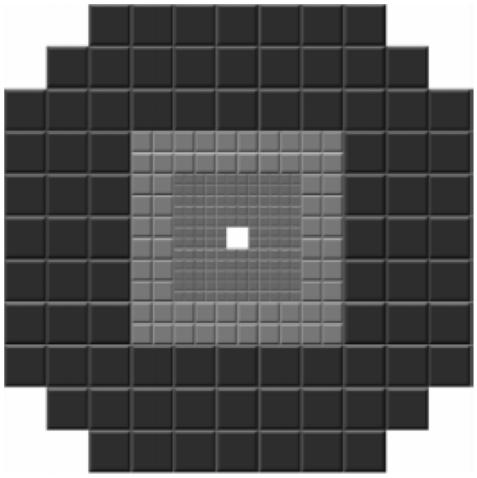

Figure 2.10: Schematic layout of the forward wall hodoscope. Taken from [31].

2.6 Data Processing

The large set of data produced during a HIC and measured by the different detectors are recorded by the **D**ata **A**c**Q**uisition (DAQ) system. The raw data is then stored in **H**ADES **L**ist-Mode **D**ata (HLD) files. The **H**ADES S**y**stem for **D**ata **R**eduction and **A**nalysis (HYDRA) framework processes the data. HYDRA is based on the *ROOT* C++ package, originally developed for the NA49 experiment.
The HADES experiment subsequently uses a **C**entral **T**rigger **S**ystem (CTS) to reduce the amount of data and dead time of the DAQ.
The first level trigger (LVL1) only selects events with a minimum track multiplicity in the TOF and RPC detectors in time coincidence with a START hit. This ensures that only events in a certain centrality range are considered. The exact conditions of the trigger are changed with the beam time to match the studied collision system and energy. For the analyzed Au+Au beam time a minimum of 5 hits was required for a *PT2* trigger, while events with more than 20 hits were classified as *PT3*.

2.6.1 Simulation

Because of limitations in the detector's acceptance and efficiency, corrections of the recorded data by comparison to simulations are required (See chapter 3.3).
Event generators are used to simulate collisions, which create momenta, energy and tracks for produced particles. These particles then pass a full geometrical simulation, containing all material constraints and the magnetic field of the HADES setup, as provided by the *GEANT* framework.
The Monte-Carlo event generators used for the present analysis are based on the relativistic transport models ***U**ltra **r**elativistic **Q**uantum **M**olecular **D**ynamics* (UrQMD) [32], and ***I**sospin **Q**uantum **M**olecular **D**ynamics* (IQMD) [33].
Since UrQMD does not produce particles with masses greater than the proton mass ($m_{\text{proton}} = 938,27\ \text{MeV/c}^2$), deuterons are embedded by a thermal *Pluto* event generator [34].
The resulting spectra can then be treated similarly to the measured data.

3 Analysis

3.1 Deuteron Reconstruction

3.1.1 Event Selection

The data, which are analyzed in this thesis, originate from Au - Au collisions recorded by the HADES collaboration in 2012. After an acceleration to a kinetic beam energy of $E_{kin} = 1.23A\text{GeV}$, the ions were shot on a gold target. Multiple selection criteria were then applied to the data, in order to purify and classify the recorded events.
A *PT3*-trigger was set to select only events with more than 20 hits in the TOF detector, so only semi-central to central events were considered. Further, cumulative triggers, as shown in Fig. 3.1 were applied:

SelectStart At least one of the two START modules must have registered a hit, while the VETO stayed unactivated.

StartPileUp Within a time frame of $-5\text{ns} < t_0 < 15\text{ns}$ around the start time, only one cluster was found in the START detector. Multiple events during this short time window (*"Pile-Ups"*), would lead to errors in the time-of-flight and mass determination, due to overlapping of the events.

GoodClusterVertex & GoodCandVertex The vertex of the reconstructed event has to lie within the physical target, to exclude reactions with any part of the detector other than the segmented target. Additionaly, at least two particles have to be registered (*"GoodCandVertex"*), and at least one track identified (*"GoodClusterVertex"*), each with a quality of the vertex reconstruction of $\chi^2 > 0$.

NoVeto Events with a registered hit in the VETO detector within $t_0 \pm 15\text{ns}$ are excluded, to also prevent the recording of collisions that occured outside the target.

VetoStart If an event can be correlated to a second START hit, but no VETO signal occurs within $15 - 350\text{ns}$ after t_0, it is also discarded.

StartMeta If a particle in the META detectors can be correlated to an event in the START detector within $80 - 350\text{ns}$, the event is rejected. Particles with these flight times can not physically originate from the triggered event, but would lead to a higher multiplicity.

This led to a final sample of around 58% of the initially recorded data.

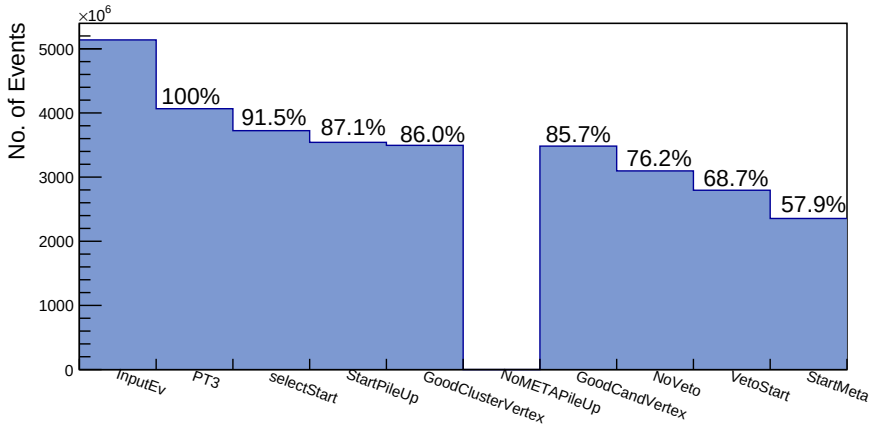

Figure 3.1: Cumulative number of events after applying each selection criteria.

3.1.2 Centrality Classification

In order to classify the events after the initial selection, the centrality of the collision, characterized by the impact parameter b, was used. As Fig.3.2 shows, the impact parameter quantifies the distance of the colliding nuclei's centers. The smaller the impact parameter, the more energy was deposited in the collision process. As this parameter is impossible to measure during or after a collision, so called *centrality estimators* have to be used as indirect probes. The Glauber model allows for a correlation of the measurable produced particle multiplicity N_{Ch} with the number of participating nucleons A_{part}, or the impact parameter b of the collision, as described in [9].

In this analysis, the measured multiplicity of TOF & RPC hits was used as an estimator to discriminate the events in four centrality classes, covering the most central 40% of collisions. Each of the classes consequently covers a 10% bin. The important parameters can be found in Table 1.

The data sample that was obtained after the event selection is spread evenly over the 4 centrality classes, as can be seen in Fig. 3.3.

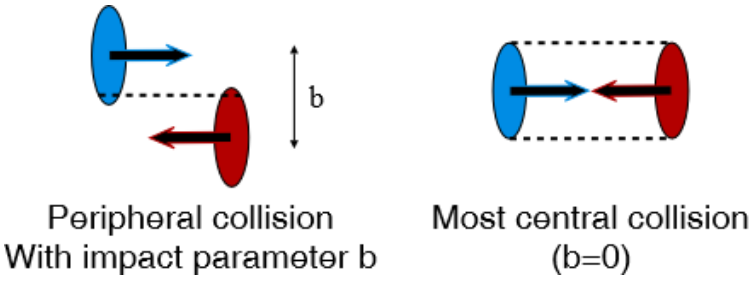

Figure 3.2: Impact parameter of two colliding nuclei

Class [%]	$< A_{part} >$	b_{max} [fm]	N_{min}	N_{max}
0-10	301 ± 11	4.6	160	250
10-20	212 ± 10	6.5	121	160
20-30	149 ± 8	7.95	88	121
30-40	102 ± 6	9.18	60	88

Table 1: Characteristics of the 40% most central Au-Au centrality classes, as estimated by a Glauber model as described in [9]. Given are the mean number of participants $\langle A_{part} \rangle$, the maximum impact parameter b_{max} and the corresponding number of hits in TOF & RPC between N_{min} and N_{max}.

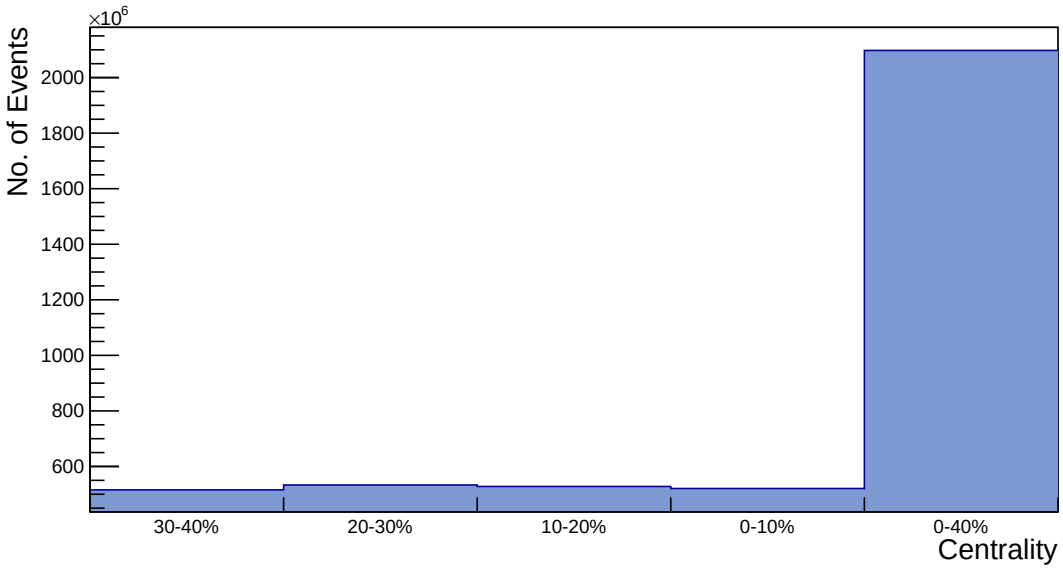

Figure 3.3: Event distribution over the most central classes, as defined in table 1.

3.1.3 Deuteron Properties

Deuteron (d)	
Mass	2.014u
Mass [MeV/c^2]	1875.612
E_B [MeV]	-2.225
Spin^{Parity}	1^+

Table 2: Properties of the deuteron, see [35].

The deuteron, as the bound state of a proton and a neutron, is the heaviest stable hydrogen isotope. Its most important characteristics can be found in Table 2. Because of the relatively low binding energy E_{bind}, it is easily formed by *pick-up* reactions (A proton with sufficient kinetic energy picks up a weakly bound neutron) [35].

3.1.4 Deuteron Identification

Particles reconstructed with the HADES spectrometer are mainly identified by the correlation between their velocity β and their momentum p. Alternatively, the energy-loss deposition in the time-of-flight (TOF) and miniwire-drift-chamber (MDC) detectors can be used for the particle identification. Additionally, *track quality cuts* were applied to the data. By cutting on a Runge-Kutta quality of $\chi^2_{RK} < 400$ and Meta-Match quality $\chi^2_{MM} < 3$, only candidates with small deviations from ideal tracks were considered. While these cuts improve the quality of the data, they also reduce the signals and therefore the resulting spectra need to be corrected for the *cut-efficiency*, which will be explained in chapter 3.3.
Also excluded from the analysis are candidates at the edge of the MDC detectors, as this regions exhibit larger deviations between simulated and measured data.
Events registered in sector 2 of the detector setup were also not considered, as this sector exhibited unstable performances at high voltages.

Cuts in Momentum and Time-of-Flight Correlation
After an initial time measurement t_0 in the START detector, one of the META detectors (TOF or RPC, depending on the polar angle of the particle tracks in the laboratory system) provides a second signal t_1 which allows for a calculation of the time-of-flight by $\Delta t = t_1 - t_0$. As charged particles do not cross the detector in a straight line, because the magnet forces them on a bend trajectory, a reconstruction of the curved track's length s is calculated by a Runge-Kutta approach. This information is then used to calculate the velocity β and Lorentz factor γ :

$$\beta = \frac{v}{c} = \frac{\frac{s}{\Delta t}}{c}, \tag{14}$$

$$\gamma = \frac{1}{\sqrt{1-\beta^2}}. \tag{15}$$

The trajectory within the magnetic field can be used to identify the momentum of a traversing particle. Charged particles, passing through a magnetic field with field strength B are subject to the *Lorentz Force* $\vec{F_L} = q\vec{v} \times \vec{B}$. The change in momentum is described by the transverse kick $\Delta\vec{p}_{kick}$.
Thus, the following relation can be obtained:

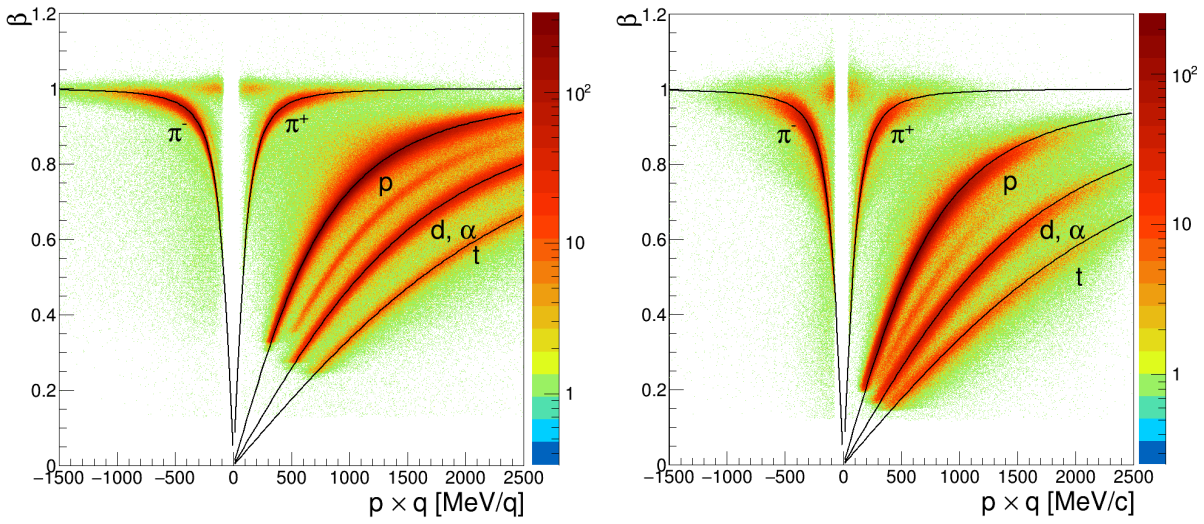

Figure 3.4: Correlation between velocity β and momentum in the RPC (left) and TOF (right) system. Lines indicate the expected trends for particles according to Eq. 19. Uncertainties in the time measurement Δ_t lead to $\beta > 1$ for velocities close to the speed of light.

$$\Delta\vec{p}_{kick} = \vec{p}_{out} - \vec{p}_{in} = \int d\vec{p} = \int \vec{F} dt \tag{16}$$

$$= \int q\left[\vec{v} \times \vec{B}\right] dt = -q \int \vec{B} \times d\vec{s} \tag{17}$$

Using the Lorentz force F_L and the centrifugal force F_Z, the *mass-to-charge* ratio of a particle can be correlated to the velocity β and momentum p :

$$\frac{m}{q} = \frac{p/q}{\beta\gamma c}. \tag{18}$$

Because the time resolutions of the TOF and RPC detector differ from each other, it is necessary to distinguish between the two systems. Fig. 3.4 shows the velocity vs. momentum distributions separately for both detectors.
Also indicated are the theoretically expected velocity and momentum correlations, as predicted by:

$$\beta = \frac{p}{m} \frac{1}{\sqrt{\left(\frac{p}{m}\right)^2 + 1}} \tag{19}$$

As indicated in Fig. 3.4, using the momentum and time-of-flight information for particle identification poses a problem for the deuteron analysis. Because the momentum is calculated from the curvature in a magnetic field, according to Eq. 18, a candidate with double the mass and double the charge of a given particle can lead to an inconclusive result. In this particular case, the deuteron ($m = 1875$ MeV/c^2, $q = 1$), and ^{4}He ("α") ($m = 3727$ MeV/c^2, $q = 2$) are overlapping.
Fig. 3.5 shows the mass distribution obtained from the data. In this representation, deuteron and ^{4}He overlap, and the ^{3}He peak, which has a higher expected nominal mass than the deuteron, is found in a lower mass region.
Therefore, additional information is required for an unambiguous identification.

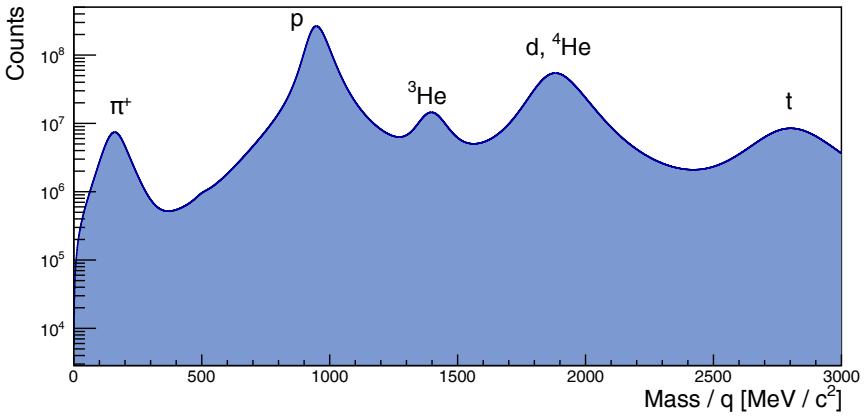

Figure 3.5: Mass spectrum for the whole data sample. Particles are distributed around their nominal mass.

Cuts in Specific Energy Loss

A property of different particle species is their specific energy loss when passing through material. In the HADES setup, the energy loss can be determined in the TOF & MDC detectors by measuring the time that the signal stays over a defined threshold, the *time-over-threshold*. The dependencies of the mean energy loss $\langle dE/dx \rangle$ on material properties, velocity, momentum and charge are described by the *Bethe-Bloch equation*, [36] :

$$-\left\langle \frac{dE}{dx} \right\rangle = Kz^2 \frac{Z}{A} \frac{1}{\beta^2} \left[\frac{1}{2} ln \frac{2m_e c^2 \beta^2 \gamma^2 T_{max}}{I^2} - \beta^2 - \frac{\delta(\beta\gamma)}{2} \right] \tag{20}$$

where:

$$\begin{aligned}
\left\langle \frac{dE}{dx} \right\rangle &: \text{mean rate of energy loss} \\
K &: 4\pi N_A r_e^2 m_e c^2 \ \left[0.307 \frac{\text{cm}^2}{\text{mol}} \right] \\
z &: \text{charge number of incident particle} \\
Z &: \text{atomic number of absorber} \\
A &: \text{atomic mass of absorber} \ \left[\frac{\text{g}}{\text{mol}} \right] \\
T_{max} &: \frac{2m_e c^2 \beta^2 \gamma^2}{1 + 2\gamma m_e/M + (m_e/M)^2} \\
M &: \text{incident particle mass} \ \left[\frac{\text{MeV}}{c^2} \right] \\
N_A &: \text{Avogadro constant} \ \left[6.022 \times 10^{23} \frac{1}{\text{mol}} \right] \\
I &: \text{mean excitation energy [eV]} \\
\delta(\beta\gamma) &: \text{density effect correction} \\
m_e &: \text{electron mass} \ \left[\frac{\text{MeV}}{c^2} \right]
\end{aligned}$$

Therefore, particles with higher charge deposit more energy while passing through the detector. This allows for a separation of ^{4}He and deuterons. The procedure is performed by first selecting a relevant mass region around 1700 MeV $< M <$ 2000 MeV to remove the proton peak around 938 MeV that dominates the spectrum.
The specific energy loss as a function of momentum measured in the TOF detector with expected correlations according to Bethe-Bloch is shown in Fig. 3.8. Because the TOF detector is situated at the end of the HADES setup and is a solid scintillator, particles can be stopped entirely. For this reason, the observed energy loss deviates from the Bethe-Bloch curve at low momenta. This is called the *full stopping* region. To remove the stopping peak, a lower momentum cut is applied at $p = 600$ MeV/c.

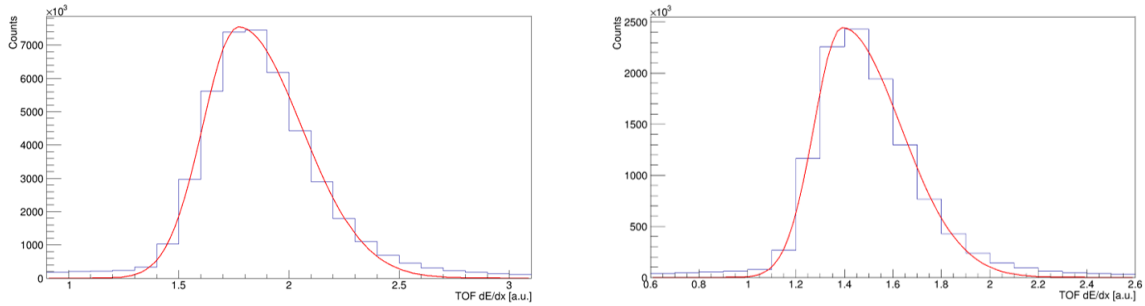

Figure 3.6: Projections of the specific energy loss in the TOF detector for two exemplary slices, fitted by an asymmetric Gaussian function, according to Eq. 21 (red).

The deuteron candidates are distributed around the theoretical curve. To estimate the width σ of this distribution, a projection of the energy loss axis is done for 25MeV wide slices perpendicular to the momentum axis. Because these projections exhibit an asymmetric shape, an upper width σ_{up}, and a lower width σ_{low} are extracted by fitting an asymmetric Gaussian function to the projections:

$$f(x) = a \times \exp\left(\frac{(x-\mu)^2}{\sigma}\right) \begin{cases} \sigma = \sigma_{low}, \text{ if } x < \mu \\ \sigma = \sigma_{up}, \text{ if } x \geq \mu \end{cases} \tag{21}$$

Where a is a constant, μ the mean value of the Gaussian and σ the width. This is shown for two momentum slices (1150 MeV$< p <$ 1175 MeV and 1975 MeV$< p <$ 2000 MeV) in Fig. 3.6.

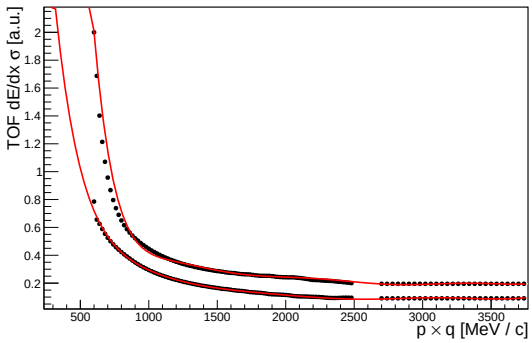

Figure 3.7: Widths σ_{up} and σ_{low} of the deuteron signal in the TOF dE/dx, extracted after fitting Eq. 21. The upper data points correspond to σ_{up}, the lower to σ_{low}. The data points are fitted with a 9^{th}-grade polynomial (red).

Afterwards, the widths obtained by the fits were plotted against the momentum and approximated by a 9^{th}-grade polynomial to achieve a smooth distribution (compare Fig. 3.7).
Subsequently, these widths were used to apply a cut of $\pm 3\sigma$ width around the theoretically expected energy loss for the deuteron candidates. Fig. 3.8 shows the specific energy loss with the final cuts indicated around the deuteron curve.
Similarly, the specific energy loss in the MDC detectors was analyzed. In this case, it was also differentiated between candidates that were registered in the TOF or RPC system, to take the different time resolutions into account. Fig. 3.9 displays the resulting energy loss distribution in the MDC detectors, with the momentum measured with the RPC. Also indicated are

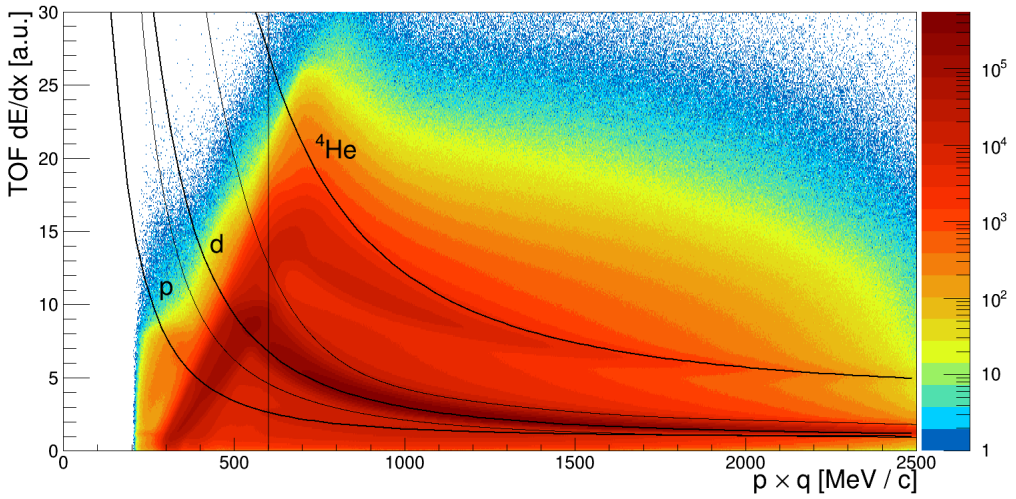

Figure 3.8: Specific energy loss in the TOF detector for particles with 1700 MeV/c^2 < M < 2000MeV/c^2. Around the theoretically expected deuteron curve according to Eq. 20, cuts within a 3σ surrounding and the low momentum cut at $p = 600$ MeV/c are indicated.

the deuteron PID cuts and the low momentum cut. The widths and fit can be found in the supplemental material 7.

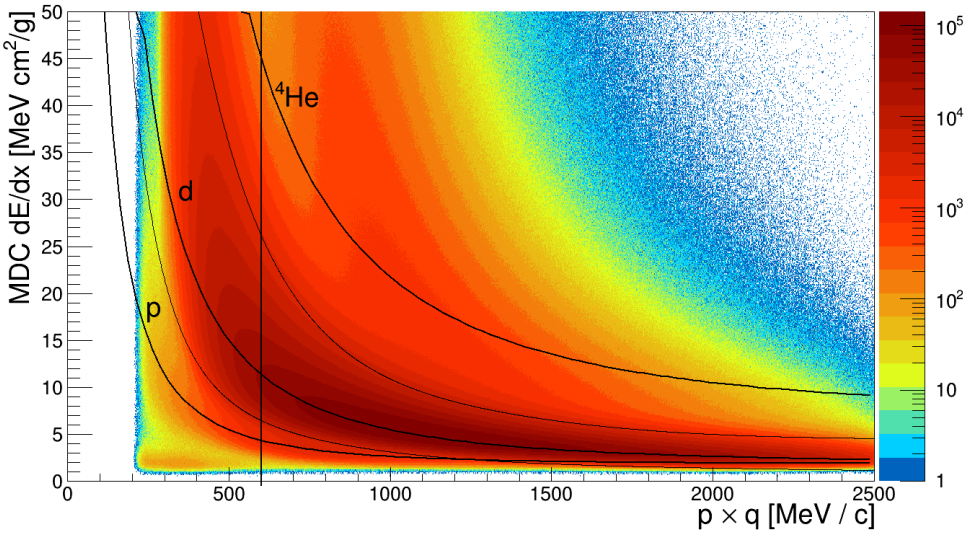

Figure 3.9: Specific energy loss in the MDC detector for particles with 1700MeV/c^2 < M < 2000MeV/c^2 measured by the RPC system. Around the theoretically expected deuteron curve according to Eq. 20, cuts within a 3σ surrounding and the low momentum cut at $p = 600$ MeV/c are indicated.

The effects of the cuts on the overall mass distribution are pictured in Fig. 3.10. The cuts successfully reduce the ^{4}He, as well as ^{3}He, triton and proton background significantly.

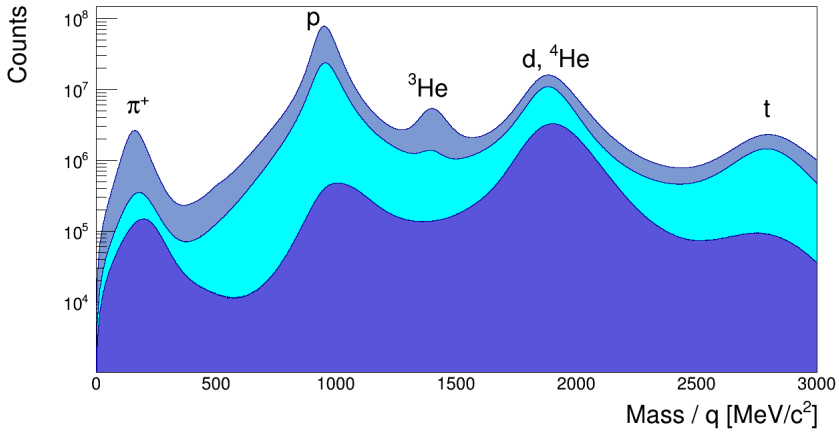

Figure 3.10: Mass spectra after the different energy loss cuts are applied. Blue represents the initial spectrum, turquoise indicates the effects of the MDC cuts and purple denotes the final mass spectrum after all cuts have been implemented

^{4}He Contamination To assess the performance of the cuts, their effect on the deuteron and ^{4}He mass spectra was investigated. By using the *IQMD* simulation, it is possible to identify each particle that was detected by their assigned *Monte-Carlo*-PID. The cuts that were used for the simulated data were obtained by the same procedure as described above for measured data. As there are differences in the resolutions (see [16]), these procedures result in different cut-values. Fig. 3.11 reveals that after applying the cuts 98% of deuterons remain, while the ^{4}He background is successfully reduced by 99.5%. This reduces the contamination from originally 8% to a statistically irrelevant contamination of 0.04%.

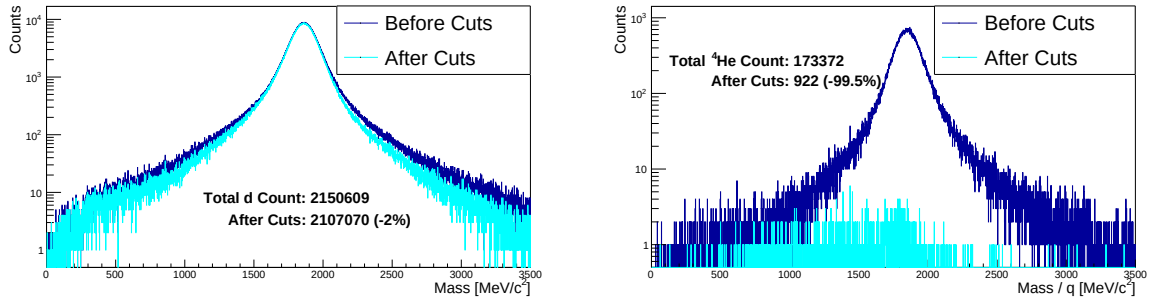

Figure 3.11: Simulated mass spectra of deuterons (left) and ^{4}He (right) in both systems (TOF and RPC), before and after the specific energy loss cuts were applied.

Phase Space Coverage The deuteron candidates that remain after the selection process exhibit a large coverage of the phase space, as shown in Fig. 3.12. Taking the beam line along the z axis, the transverse mass m_t and the rapidity y are defined as [37] :

$$m_t c^2 = (mc^2)^2 + (p_x c)^2 + (p_y c)^2 \tag{22}$$

$$y = \ln\left(\frac{E + p_z c}{m_t c^2}\right) \tag{23}$$

For the analyzed Au+Au collisions at 1.23AGeV mid-rapidity corresponds to $y_{cm} = 0.74$.

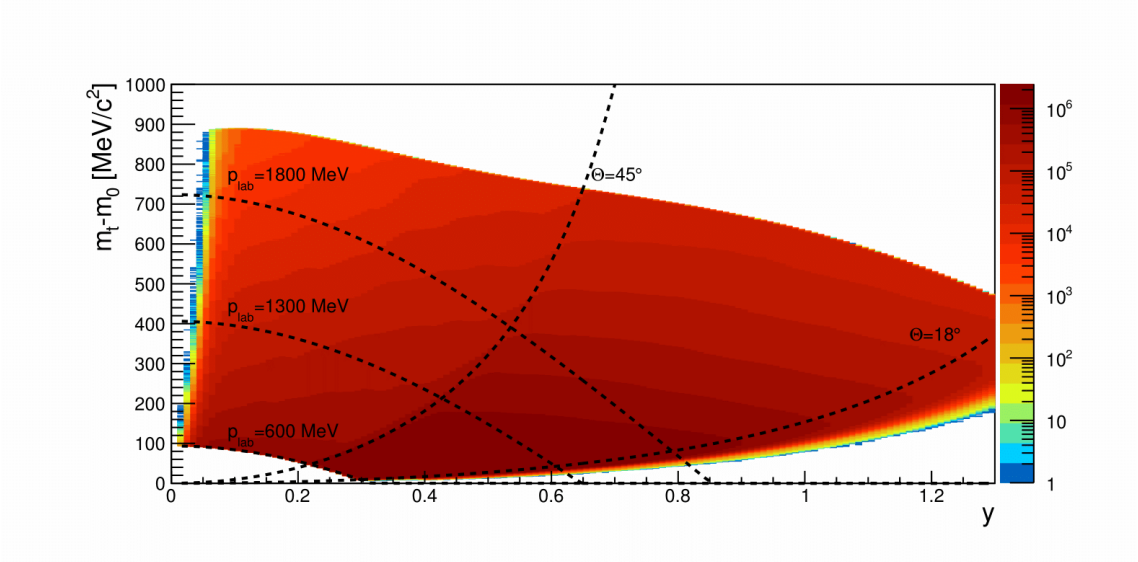

Figure 3.12: Phase space coverage of the identified deuteron candidates as a function of rapidity and reduced transverse mass. The missing area in the low transverse mass and rapidity region is caused by the low momentum cut. The dashed lines represent regions of constant momentum at $p_{lab} = 600$ MeV (low momentum cut), $p_{lab} = 1300$ MeV and $p_{lab} = 1800$ MeV or polar angle of $\Theta = 45°$ (the geometric border between RPC and TOF detector) and $\Theta = 18°$.

3.2 Count Rate Estimation

In order to calculate the count rate of the deuterons, the phase space coverage, as pictured in Fig. 3.12 was divided into cells along the rapidity and transverse mass axis. These cells were chosen to cover an interval of $0.09 < y < 1.29$ along the y-axis and span across 900 MeV/c^2 along $m_t - m_0$. The widths of the cells were set to be 0.1 for the rapidity and 25 MeV/c^2 for the transverse mass. This yielded a segmentation of 12 rapidity and 36 transverse mass bins, totaling 432 bins. For each of the bins, the corresponding mass spectrum was further analyzed.

As explained before, even after application of the introduced cuts, a relatively small underground of protons, tritons and other fragments remained. To remove this contamination from the deuteron count rate, each peak next to the deuteron signal was fitted with a Gaussian function and subtracted from the spectrum. The deuteron peak around $m_{deut} = 1875.6$MeV is then described by a Gaussian fit.
The remaining deuteron signal was afterwards integrated in a 3σ region around its mean. For this result, the statistical error can be estimated as $\sqrt{N}$, where N is the total number of counts per cell. This process is shown as an example for the 30-40% most central events in Fig. 3.14. The deviations between the fit and data between the signals can be explained by residual background. As the peak is integrated within a 3σ interval, a good description of the deuteron signal is paramount.

To assess the parameters of the fits, the resulting means and widths of the fits were studied as a function of increasing transverse mass. The mean should, with minor fluctuations, describe the nominal mass, as given in table 2. This is presented in Fig. 3.13 for the midrapidity region. The width's continuous increase originates from the decrease of momentum resolution at higher transverse masses. Overall, the tendencies of the fits are within the expected range.

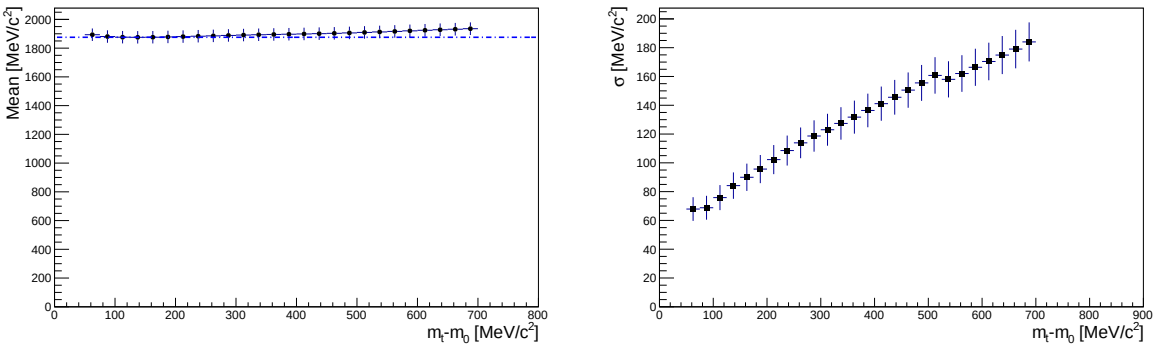

Figure 3.13: Mean (left) and σ (right) extracted for a region around midrapidity ($0.69 < y < 0.79$) as a function of the transverse mass. In the left plot, the nominal deuteron mass, as given in table 2 is indicated by a dotted line.

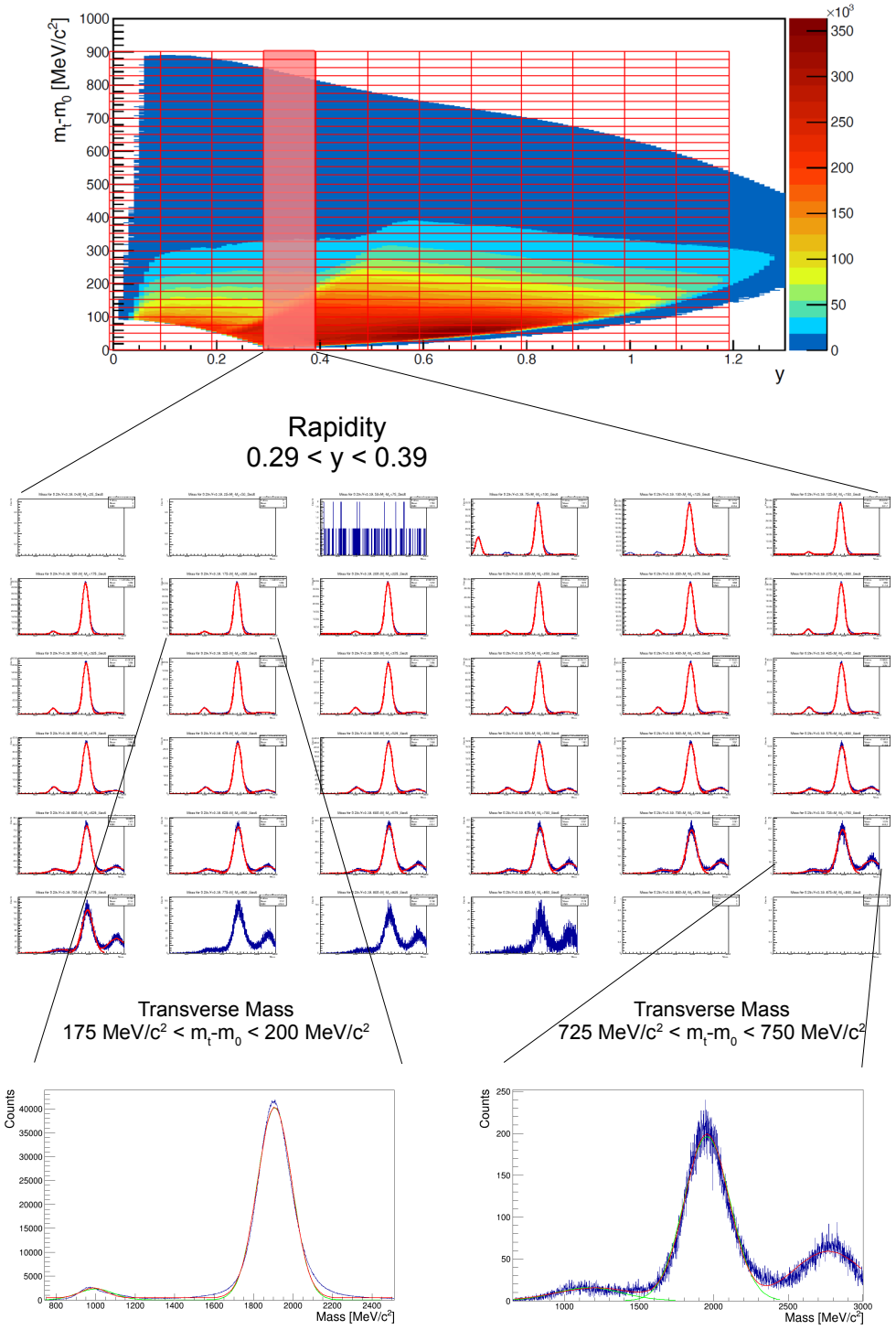

Figure 3.14: Procedure of count rate estimation for the most central 30-40% of events. After the phase space has been separated into cells each rapidity slice is analyzed (here shown for a backward rapidity bin in the TOF system). For every transverse mass bin the mass spectra is drawn and treated as described in chapter 3.2. This is shown here exemplary for two randomly selected bins, one with high and one with low statistics.

3.3 Efficiency & Acceptance Correction

The HADES detector setup features a large geometrical coverage, but in between the different sectors detector mounts or other materials cause holes in the acceptance. An *acceptance correction* has to be applied to account for particles that do not pass through the detector's active regions.
Additionally, particles in the active detector regions are not always correctly identified. Reasons for this can be found in the detector response or the cuts that were applied during the analysis. To correct for these issues, an *efficiency correction* factor is calculated separately for each step of the particle identification process, as described in chapter 3.1.3.
To calculate a final correction matrix over the entire phase space, the different acceptance and efficiency correction factors were then combined into a total correction by multiplication.
The acceptance was estimated by employing the earlier described simulations and comparing the known number of generated tracks $N_{gen}(m_t, y)$ to the detected amount of candidates $N_{acc}(m_t, y)$ from the measured data, as defined in chapter 3.1.3, in each phase space cell. The resulting acceptance matrix is shown in Fig. 3.15.

$$\mathrm{acc}(m_t, y) = \frac{N_{acc}(m_t, y)}{N_{gen}(m_t, y)} \tag{24}$$

Afterwards, the efficiency of the track reconstruction can be examined, as the number of reconstructed tracks $N_{reco}(m_t, y)$ in relation to the accepted particles.

$$\epsilon_{reco}(m_t, y) = \frac{N_{reco}(m_t, y)}{N_{acc}(m_t, y)} \tag{25}$$

This is shown in Fig. 3.16.
Each cut the data is subjected to, is similarly assessed by analyzing the number of reconstructed particles before $N_{pre}(m_t, y)$ and after $N_{post}(m_t, y)$ applying the cut.

$$\epsilon_{cut}(m_t, y) = \frac{N_{post}(m_t, y)}{N_{pre}(m_t, y)} \tag{26}$$

Fig. 3.17 and 3.18 show the efficiency factors of the cuts on the specific energy loss, as explained in chapter 3.1.4.

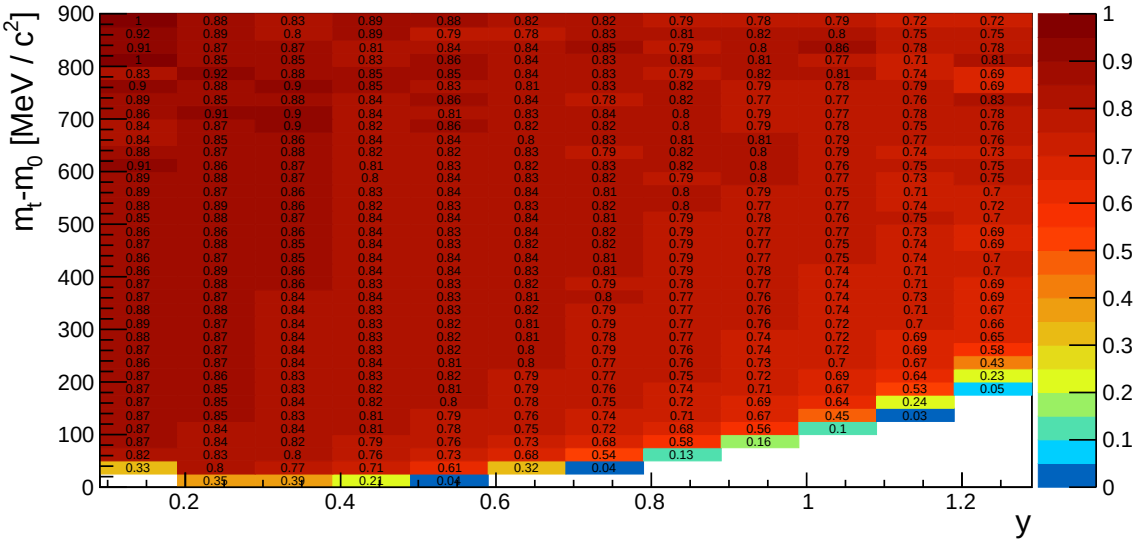

Figure 3.15: Acceptance factor, as obtained from the UrQMD simulation, according to Eq. 24.

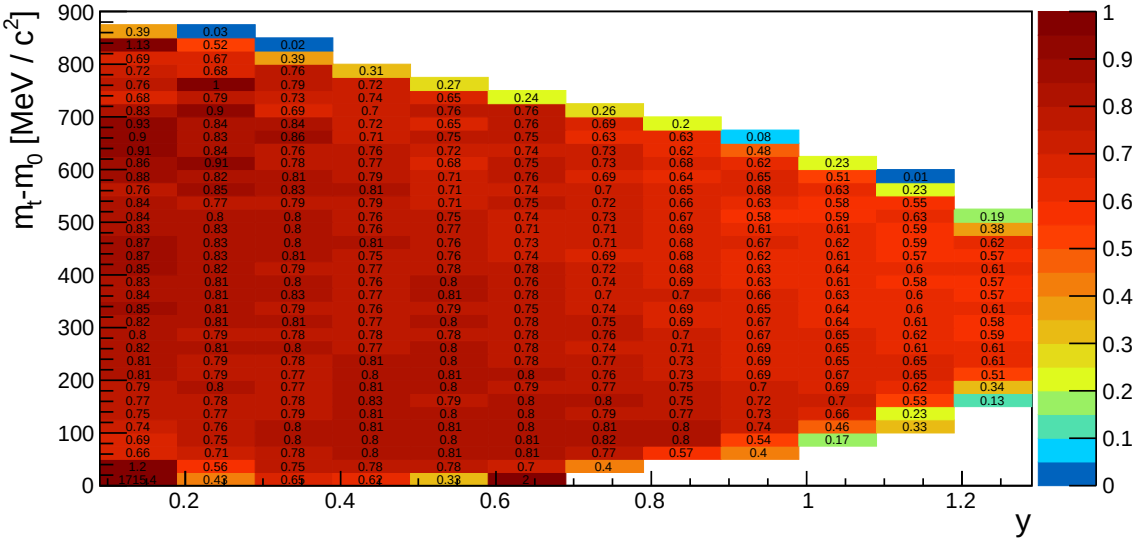

Figure 3.16: Reconstruction efficiency, as obtained from the UrQMD simulation, according to Eq. 25.

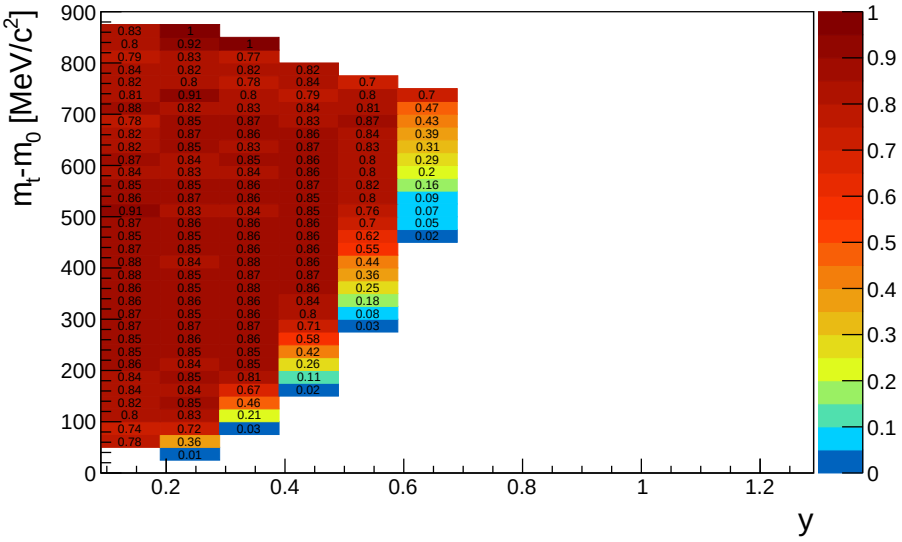

Figure 3.17: Efficiency of the specific energy loss cuts, as obtained from the IQMD simulation according to Eq. 26. Shown are the values for the TOF detector.

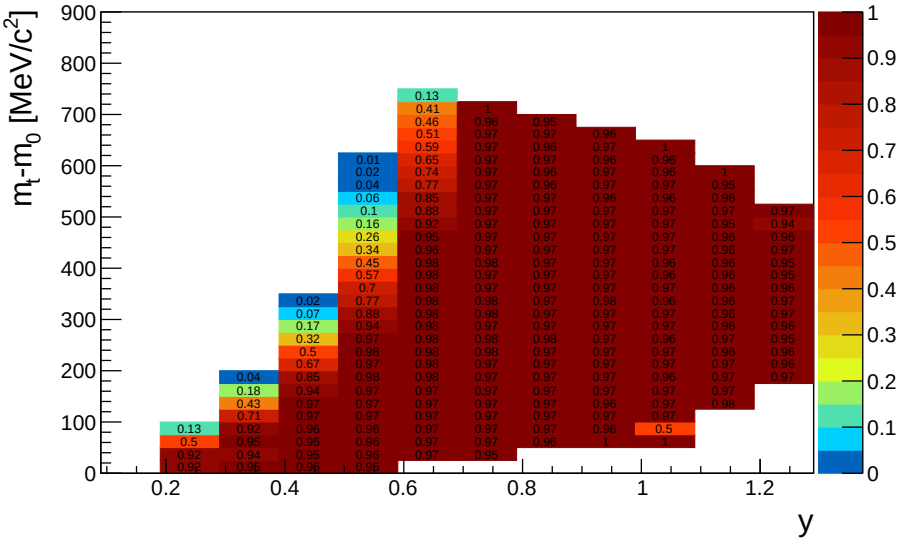

Figure 3.18: Efficiency of the specific energy loss cuts, as obtained from the IQMD simulation according to Eq. 26. Shown are the values for the MDC detector.

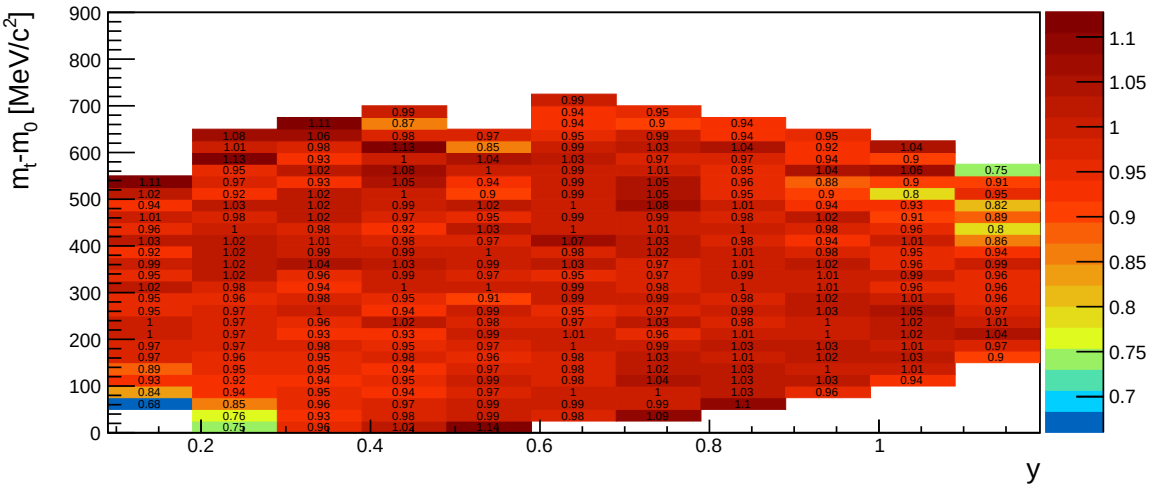

Figure 3.19: Ratio of the correction factors obtained by calculating the efficiencies and acceptance separately by taking the overall ratio of identified candidates to the generated ones.

In case of statistically independent cuts, the final total correction factor ϵ_{tot} should be the product of acceptance and the separate efficiencies.

$$\epsilon_{tot}(m_t, y) = \text{acc}(m_t, y) \times \epsilon_{reco}(m_t, y) \times \Pi_i \epsilon_{cut,i}(m_t, y) \tag{27}$$

which can be rewritten as:

$$\epsilon_{tot}(m_t, y) = \frac{N_{acc}(m_t, y)}{N_{gen}(m_t, y)} \times \frac{N_{reco}(m_t, y)}{N_{acc}(m_t, y)} \times \frac{N_{post}(m_t, y)}{N_{pre}(m_t, y)} \tag{28}$$

$$= \frac{N_{post}(m_t, y)}{N_{gen}(m_t, y)} \tag{29}$$

This total correction can also be obtained by dividing the count rate of the final deuteron candidates, that have undergone all identification cuts as described above, by the number of generated tracks from the simulation. The matrix that is obtained by this procedure was compared to the one from the separately calculated and multiplied efficiencies. The percentage of the resulting deviation is shown in Fig 3.19. A greater deviation is observed in the TOF region at lower rapidities y.
Because of the statistical independence of the cuts, the latter described method was used to calculate the acceptance & efficiency corrections of the analyzed data. Fig. 3.20 presents the correction factors, that were used for the subsequent analysis.

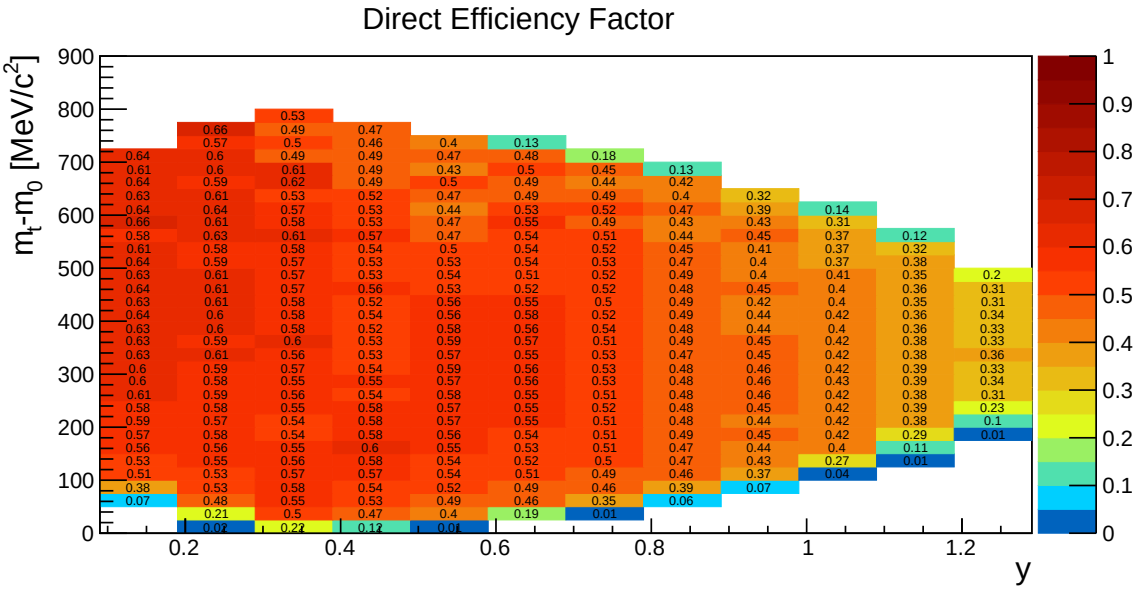

Figure 3.20: Efficiency and acceptance correction matrix, obtained according to Eq. 29

4 Results

4.1 Transverse Mass Spectra

The integration of the mass distribution, as described in chapter 3.2, results in a *transverse mass spectrum* for each rapidity interval. These spectra were corrected for efficiency and acceptance, as described in detail in chapter 3.3. The resulting corrected number of counts is divided by m_t^2 in order to be described by theoretical functions. Two general approaches were considered for this analysis:

Boltzmann Approach The first, most simple interpretation of the data is that of a static thermal source which can be described by the thermal Boltzmann relation [38]:

$$\frac{1}{m_t^2}\frac{d^2N}{dm_t dy} = C(y)\exp\left(\frac{-(m_t - m_0)}{T_B(y)}\right) \tag{30}$$

where C is a constant for each rapidity interval and T_B, the *inverse slope parameter*, describes the Boltzmann temperature for a source in thermal equilibrium. The subtraction of the nominal particle mass m_0 is done, because it later on permits an easier comparison of different particle species.
At midrapidity y_{cm} the inverse slope T_B reaches its maximum value, often characterized as *effective temperature* T_{eff}. The *kinetic freeze-out temperature* T_{kin} of the system can then be derived as:

$$T_{kin} = \frac{T_{eff}}{\cosh(y_{cm})}. \tag{31}$$

In transverse mass regions that are not accessible for the detector because of its acceptance limitations, the fit to the data points can be extrapolated in order to obtain a rapidity-differential yield. The analytic integration of Eq. 31 in the range of $[m_0, +\infty]$ yields:

$$\left.\frac{dN}{dy}\right|_{y_i} = C(y_i)[(m_0c^2)^2 T_B(y_i) + 2m_0c^2T_B^2(y_i) + 2T_B^3(y_i)] \tag{32}$$

where all parameters have previously obtained by fitting a Boltzmann exponential to the transverse mass spectra.

Siemens Rasmussen Approach A more realistic approach, which also contains a constant radial expansion velocity β of the particle-emitting source, is the version of the *blast-wave* model suggested by Siemens & Rasmussen. It is able to describe the flattening shape, that semi-logarithmic representations of hadron's transverse mass spectra exhibit in low transverse momenta regions, which can not be represented by the earlier described Boltzmann-Ansatz [16]:

$$\frac{d^2N}{2\pi p_t dp_t y_0} = C(y) E e^{-\gamma_r \frac{E}{T}} \left[\left(\gamma_r + \frac{T}{E} \right) \frac{\sinh(\alpha)}{\alpha} - \frac{T\cosh(\alpha)}{E} \right]. \tag{33}$$

Here, $C(y)$ is a constant for each rapidity bin, E represents the particle's center-of-mass energy, $\gamma_r = \frac{1}{\sqrt{1-\beta_r^2}}$ is the Lorentz factor of the radial expansion, T the kinetic freeze-out temperature, β_r the radial expansion velocity and $\alpha = \frac{\gamma_r \beta_r p}{T}$ (where p is the momentum of the particle in the center-of-mass system).
The free parameters T, β_r and $C(y)$ of this function are strongly correlated.

For the most central 10% of events the transverse mass spectrum is shown in Fig. 4.1. The lowest pictured rapidity (*most backward*) bin is from $0.09 < y < 0.19$ which can be converted to the center-of-mass rapidity by subtracting the value for mid-rapidity of $y_{cm} = 0.74$, leading to a center-of-mass interval of $-0.65 < y_{cm} < -0.55$. The highest *(most forward)* rapidity displayed is $1.09 < y < 1.19$, corresponding to a center-of-mass rapidity interval of $0.35 < y_{cm} < 0.45$. In between, each rapidity is pictured in $\Delta y = 0.1$ steps.
For better visibility, the different rapidity spectra are scaled by powers of 10.
Each rapidity interval is fitted with a Boltzmann function, according to Eq. 31 and a Siemens Rasmussen parametrization, as given by Eq. 33. Because of the strong correlation of the free parameters of the Siemens Rasmussen function, a χ^2 minimization process has to be conducted in order to ensure that the fit does not run in a local minimum. During the procedure the fit parameters T and β_r are varied to find the optimum global parameters. This is explained in detail in chapter 4.1.1.
It is observed that the Siemens Rasmussen function better describes the spectrum at low transverse momenta. Especially around midrapidity (black empty squares) the quality of the fit noticeably improves.
Fig. 4.2 shows the transverse mass spectra, zoomed in at mid-rapidity. The deviations become more obvious in this close up representation. While the exponential Boltzmann fit results in an approximate distribution and describes the data well for intermediate transverse masses, the Siemens Rasmussen clearly follows the trend also in regions of high and low m_t.
In order to quantify this improvement, Fig. 4.3 shows the ratios of both fits to the data points. If the fits were in perfect agreement with the measured data, the ratio should be 1. (Again, the spectra were scaled to improve visibility). As expected, the Siemens Rasmussen approximation results in a much closer description of the data for very high or low transverse momenta.

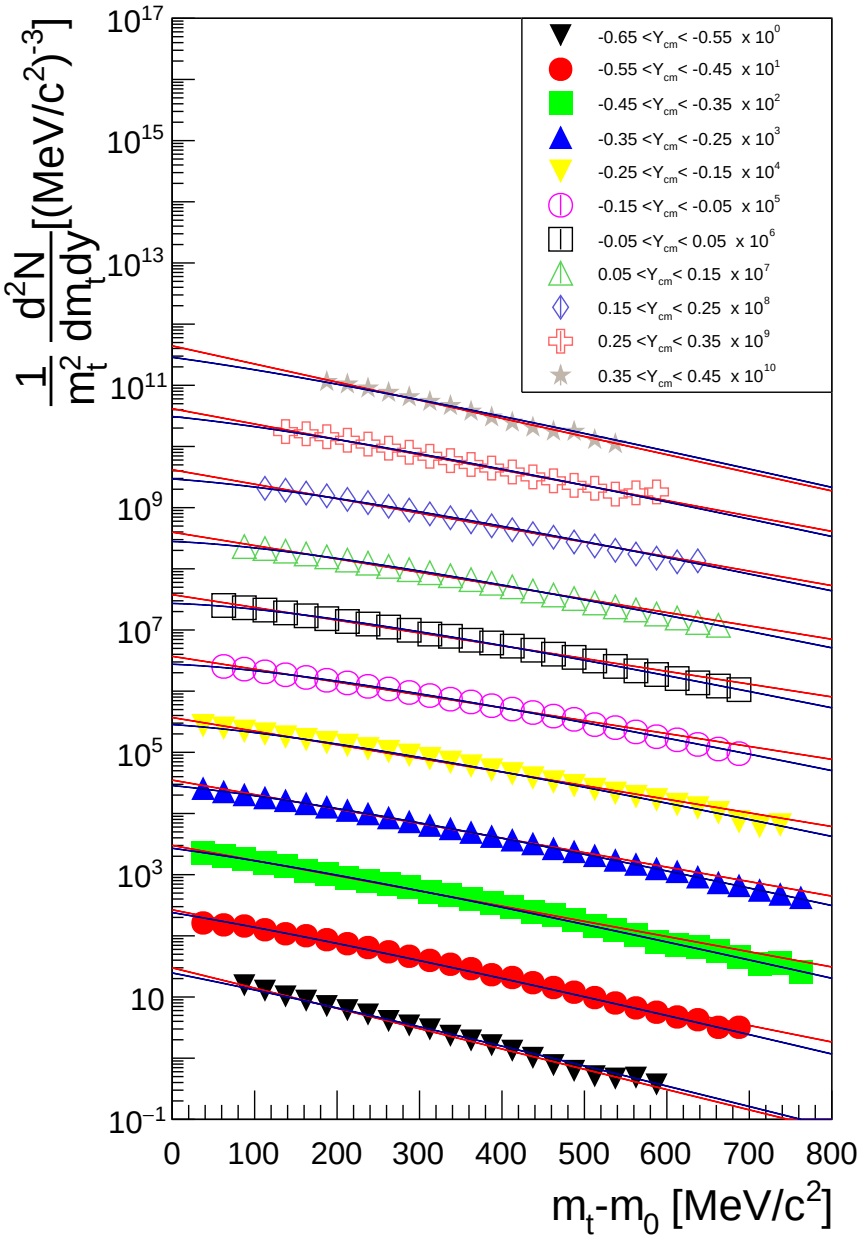

Figure 4.1: Efficiency and acceptance corrected transverse mass spectra of deuterons for the 0-10% most central events, scaled by $1/m_t^2$. For better visibility, each spectrum is multiplied by a power of 10, as indicated in the legend. Also drawn are fits with a *Boltzmann* (red, Eq. 31) and *Siemens Rasmussen* (blue, Eq. 33) function. Other centralities are shown in the supplemental material 7

.

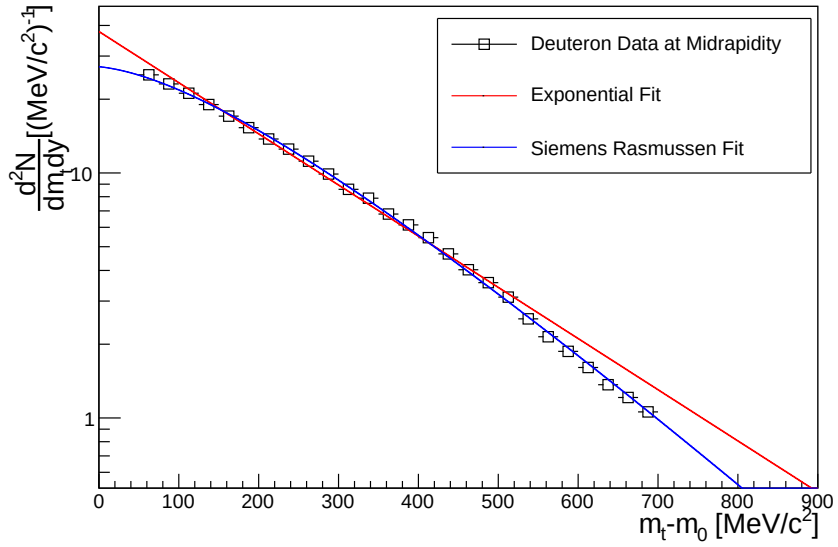

Figure 4.2: Transverse mass spectrum at mid-rapidity for the most central 0-10% of events. Fits were performed with the exponential Boltzmann (red) and Siemens Rasmussen (blue) function.

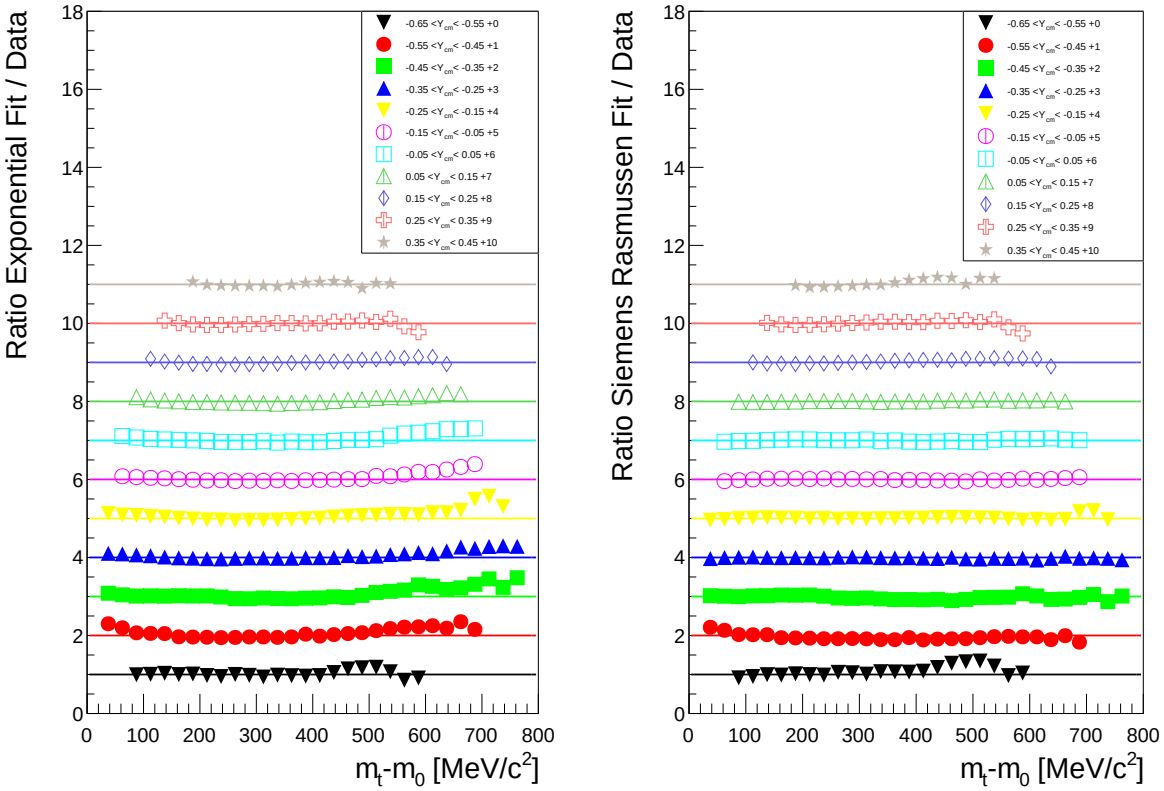

(I) (II)

Figure 4.3: (I) Ratio of the Boltzmann-fit from Fig. 4.1 to the data. (II) Ratio of the Siemens Rasmussen-fit from Fig. 4.1 to the data.

4.1.1 Global Parameter Optimization

As indicated in Eq. 33, the Siemens-Rasmussen function depends on three free variables: β_r, T and $C(y)$. While $C(y)$ is a rapidity dependent normalization constant that is re-evaluated for each fit, the first two parameters β and T are heavily correlated. As a consequence, the fit can result in only a local, but not global minimum.
In order to find a global minimum, which provides the real freeze-out parameters, a χ^2 minimization according to *Pearson's chi squared test* [39] was performed.
It can generally be applied in the case that a set of N measurements $x_i \pm \sigma_i$ exists and a theoretical expectation value μ_i (a *null hypotheses*) for each measurement is given. In the case at hand, the theoretical expectation is represented by the fit to the data, while the measurements x_i are realized by the transverse mass spectra. Then, the quality of the fit, χ^2 of the approximated values to the model can be calculated as:

$$\chi^2 = \sum_{i=1}^{N} \left(\frac{x_i - \mu_i}{\sigma_2} \right)^2 \tag{34}$$

Here, the fit quality is rated by the number of standard deviations, that each data point is differing from the model. This equation assumes a statistical independence of the data points.
By that procedure, the quality of the entire fit to the data points can be summarized in a single quality parameter. The closer to unity χ^2 ends up to be, the better the distribution is described by the fit to the data.
To obtain the χ^2 of the Siemens-Rasmussen fits each possible parameter combination in the T-β_r plane was systematically fitted for a chosen range of $0 < \beta_r < 0.75$ and 50 MeV$< T <$ 175 MeV. These regions are within the reasonable range, as measured by other particle species with HADES [16]. In this interval the parameters were manually varied in small steps and for every possible combination a Siemens Rasmussen function fitted to the data by varying C. For each fit the χ^2 was determined.
The χ^2 values are then normalized to the number of *degrees-of-freedom (NDF)*. The NDF of a fit can be determined by subtracting its number of parameters from the number of data points. In order to find a global minimum for all rapidities initially the non-normalized values for χ^2 for all rapidity intervals are summed up and the resulting distribution afterwards normalized by the total number of degrees-of-freedom.

Fig. 4.4 shows the obtained χ^2 map as it results from the systematic fitting of Eq. 33 to the m_t spectra, which are pictured in Fig. 4.1. A trend is visible with a minimum region around $T = 100$ MeV and $\beta_r = 0.37$.
This procedure was repeated for the four centrality bins $(0 - 10\%)$, $(10\% - 20\%)$, $(20\% - 30\%)$ and $(30\% - 40\%)$. The resulting fits for the midrapidity bin are pictured in Fig. 4.5 and the corresponding parameters given in table 3. The kinetic freeze-out temperature T and transverse expansion velocity β_r both increase for more central events.
For the most peripheral bin $(30\% - 40\%)$ the fit quality deteriorates significantly in the higher transverse mass regions.

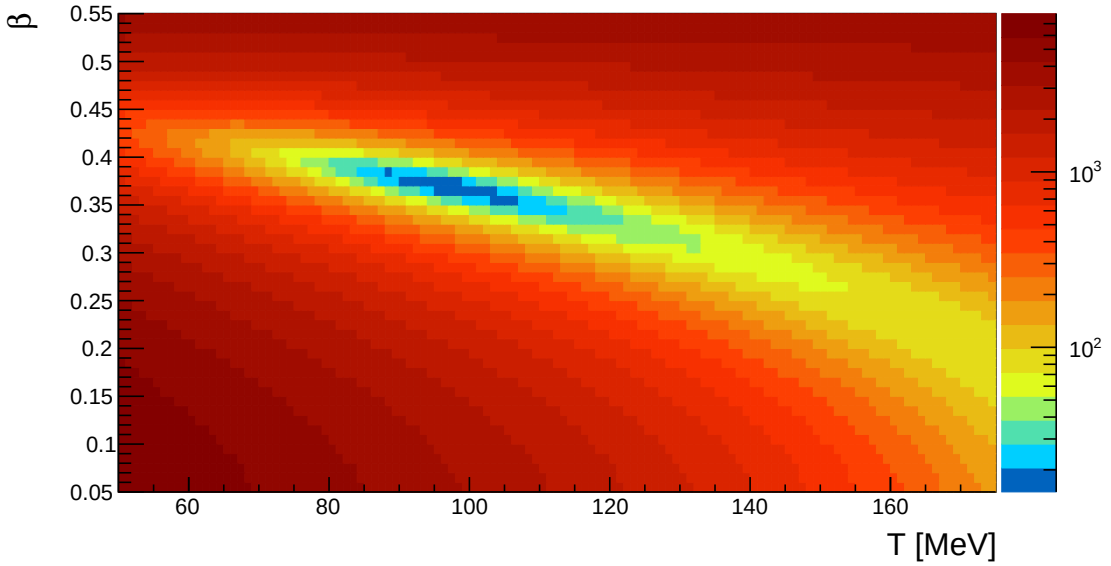

Figure 4.4: Results from the χ^2 mapping in the T-β_r plane, normalized by the degrees-of-freedom for the 10% most central events, as obtained by applying fits according to Eq. 33 to the transverse mass spectra (fig. 4.1) summed up over all rapidities.

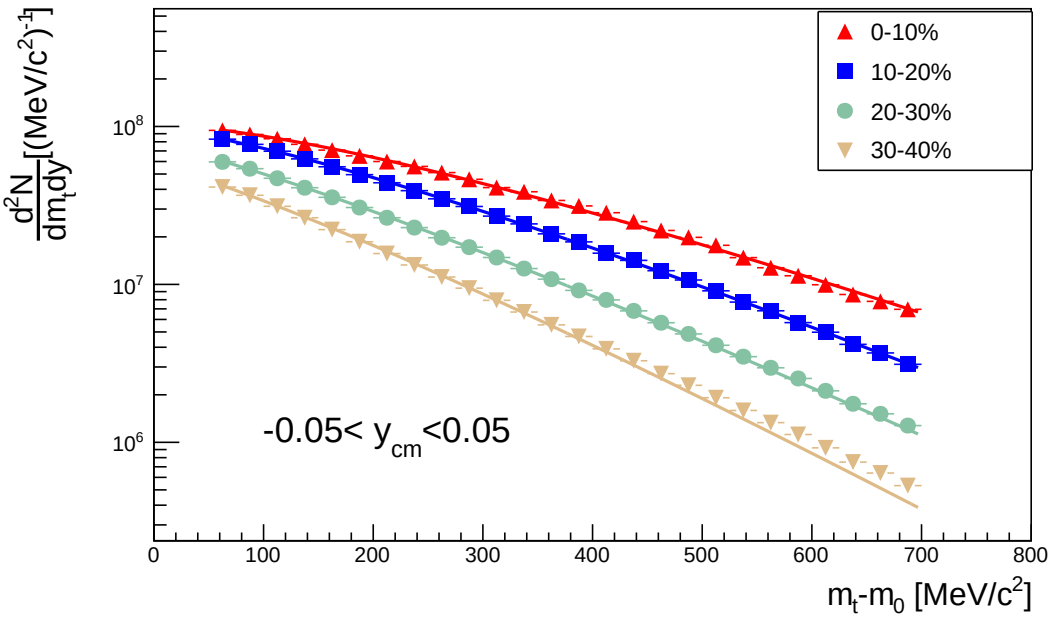

Figure 4.5: Transverse mass spectra at mid-rapidity for the 4 centrality classes $(0-10\%)$,$(10\%-20\%)$, $(20\%-30\%)$ and $(30\%-40\%)$. Fits of a Siemens Rasmussen function (Eq. 33) have been applied.

Freeze-out Parameters		
Centrality Class [%]	T [MeV]	β_r
0-10	100 ± 8	0.37 ± 0.01
10-20	92 ± 4	0.33 ± 0.01
20-30	88 ± 5	0.29 ± 0.01
30-40	78 ± 6	0.27 ± 0.02

Table 3: Freeze-out parameters for different centralities, obtained by fitting a Siemens Rasmussen function (Eq. 33) to the transverse mass spectrum. The estimation of the systematic errors is described in chapter 4.3.

4.2 Rapidity Spectra

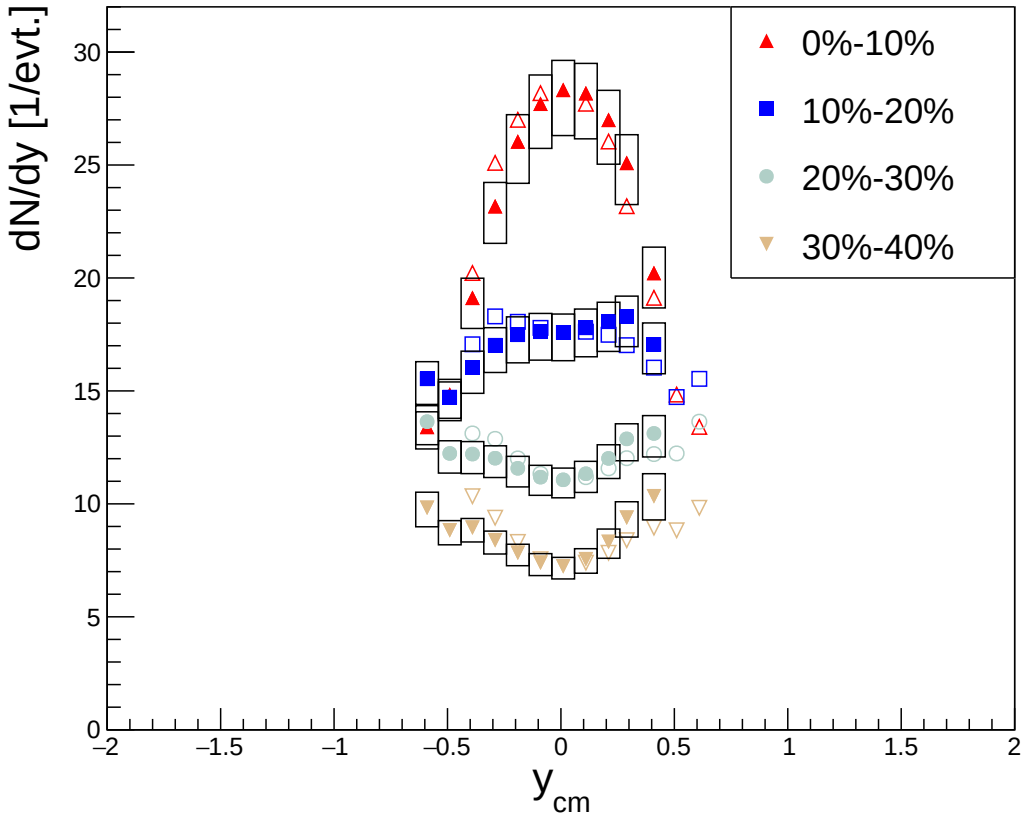

Figure 4.6: Rapidity density distributions of produced deuterons. Shown are four centrality classes. Also indicated are systematic errors (boxes) (See chapter 4.3), statistical errors (hardly visible due to their small magnitude) and reflections around y_{cm} (open symbols).

The extrapolation of the transverse mass spectra to unmeasured regions with a Siemens Rasmussen function (Eq. 33), as shown in chapter 4.1, is used to integrate the invariant yield. First the data N_{data} in the measured range from $m_t^{\min}$ to $m_t^{\max}$ is summed up. Subsequently the extrapolation factor $f(y)$ is calculated from the Siemens Rasmussen fit $f_{SR}(m_t, y)$:

$$f(y) = \int_0^{\infty} f_{SR}(m_t, y)\mathrm{d}m_t - \int_{m_t^{\min}}^{m_t^{\max}} f_{SR}(m_t, y)\mathrm{d}m_t \tag{35}$$

and added to N_{data} for the total invariant yield. It is then divided by the total number of analyzed events (See fig. 3.1) in order to obtain the rapidity density distribution $\frac{dN}{dy}$. This is shown for the analyzed centrality classes in Fig. 4.6. The rapidity density distribution is within the errors symmetric around midrapidity. To verify this, the reflections of the measured data points are also indicated by open symbols.
The most central events exhibit a Gaussian like distribution around midrapidity, which resembles a thermal spectrum with a maximum value of $\frac{dN}{dy}|_{y_{cm}} = 28 \pm 2$.
For more peripheral events an increasing spectator contribution at rapidities further away from y_{cm} can be observed which leads to a *flattening* of the spectra.
An additional quantity is the inverse slope parameter, that can be extracted from the Boltzmann

fits to the transverse mass spectra, shown in chapter 3.2. For the assumption of a static thermal source, this inverse slope parameter corresponds to the *Boltzmann temperature* T_B. This is shown in Fig. 4.7 for the analyzed centrality classes.
At mid-rapidity, the Boltzmann temperature is the *effective Temperature* T_{eff} of the particles (compare section 4.1).
The distribution does not follow a $\cosh(y)$ function as shown in Fig. 4.8, which would be expected for a static thermal source. This is due to the neglect of radial flow effects in this assumption.

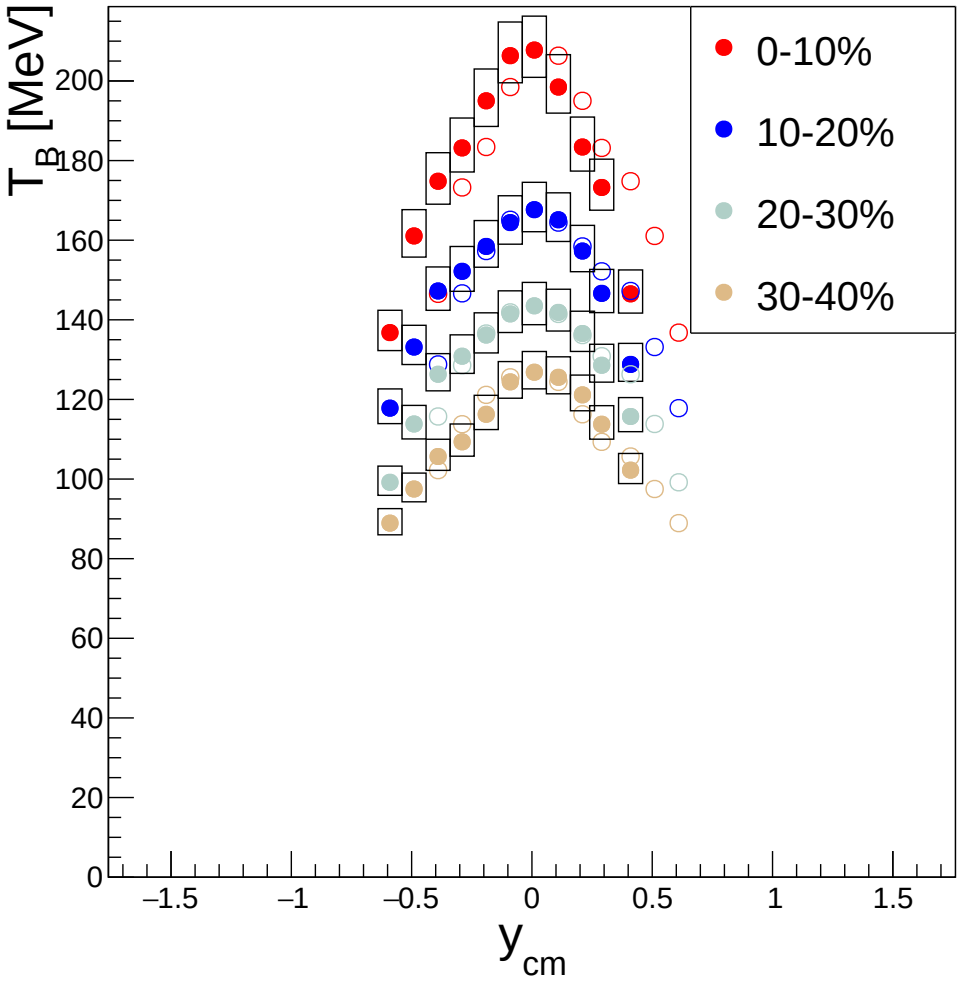

Figure 4.7: Inverse slope parameter distribution of the Boltzmann-fits (Eq. 31) to the transverse mass spectra of the deuterons. Shown are four centrality classes. Also indicated are systematic errors (boxes) (See chapter 4.3), statistical errors (hardly visible due to their small magnitude) and reflections (open symbols).

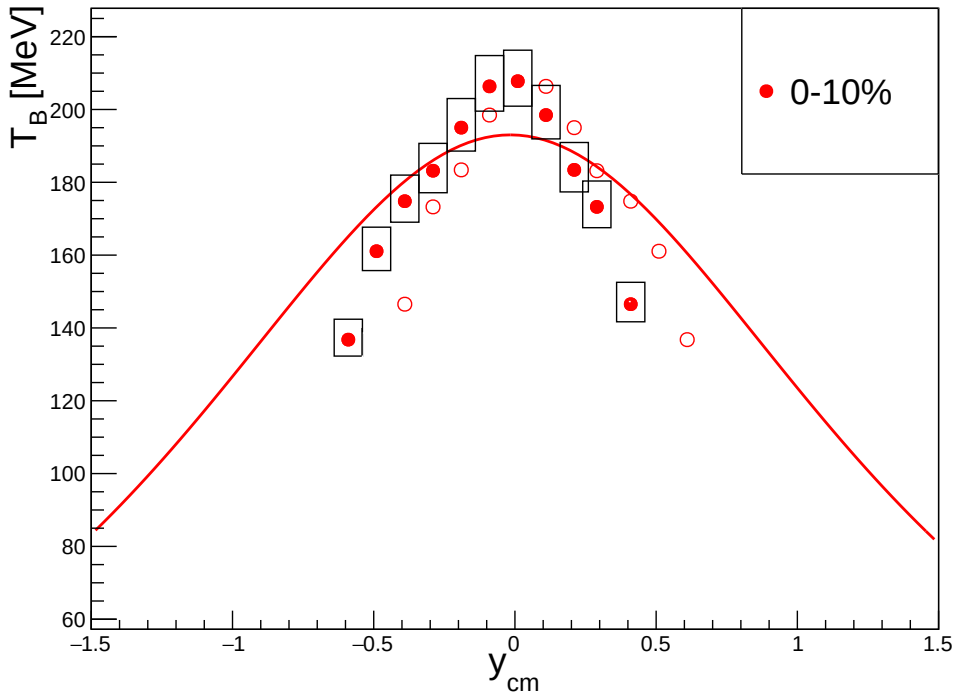

Figure 4.8: Inverse slope parameter distribution of the Boltzmann-fits (Eq. 31) to the transverse mass spectra of deuterons for the most central 10% of events. Also indicated are systematic errors (boxes) (See chapter 4.3), statistical errors and reflections (open symbols). The red line denotes the fit of an inverse $\cosh(y)$ function.

4.3 Estimation of Systematic Errors

Results from any experiment are subject to two major types of errors: *Statistical errors* and *systematic errors*.

Statistical errors originate from statistical fluctuations around a mean value. By increasing the number of events taken into consideration, these errors can usually be reduced. The major source for statistical errors in the analysis at hand is the number of identified deuterons. Because they are reconstructed with good statistics, this error ends up being small.

Systematic errors on the other hand are caused by the detectors and chosen methods used for the analysis. They can not be removed or reduced by increased statistic, but reproduce for every repetition of the experiment. As every selection, correction or processing of data introduces new systematic errors, they have to be evaluated for every step of the analysis. The major contributions are discussed in the following section.
In order to estimate the systematic uncertainties, all applied cuts were varied in a physical range and the deviations on the rapidity and T_B distribution examined. Because the errors on the particle identification cuts originate from the differences between the measured data and the simulations, the efficiency and acceptance corrected results were investigated.

Systematic Effects of the Specific Energy Loss Cuts $\Delta_{dE/dx}$

The specific energy loss cuts, calculated as introduced in section 3.1.3, are very efficient in removing the ^{4}He contamination of the deuteron spectra and considerably improve the signal-to-background ratio of the selected deuteron candidates. Nevertheless, the existing differences in simulation and data lead to a systematical bias in the correction of the measured data.
To inspect the magnitude of this effect, the cuts, which are usually applied in a 3σ interval around the mean, were also applied in a 2σ wide cut. This was done for the most central 10% of events, as well as for the most peripheral analyzed $30\% - 40\%$ centrality bin, in order to rule out a centrality dependence of the error.
Fig. 4.9 shows the bias on the resulting rapidity density. The error appears to be small and independent of the rapidity. Also, no systematic effect of the centrality can be observed, as the trend of the relative error is similar for very central (0-10%) and peripheral (30-40%) events. It can however be observed that ratios > 1 and < 1 are produced.
To take this asymmetry into consideration, the upper and lower error were averaged by using a linear fit. This resulted in an estimated average systematic error of $\Delta_{dE/dx,upp} = 0.5\%$ and $\Delta_{dE/dx,low} = 2\%$ for the particle identification.

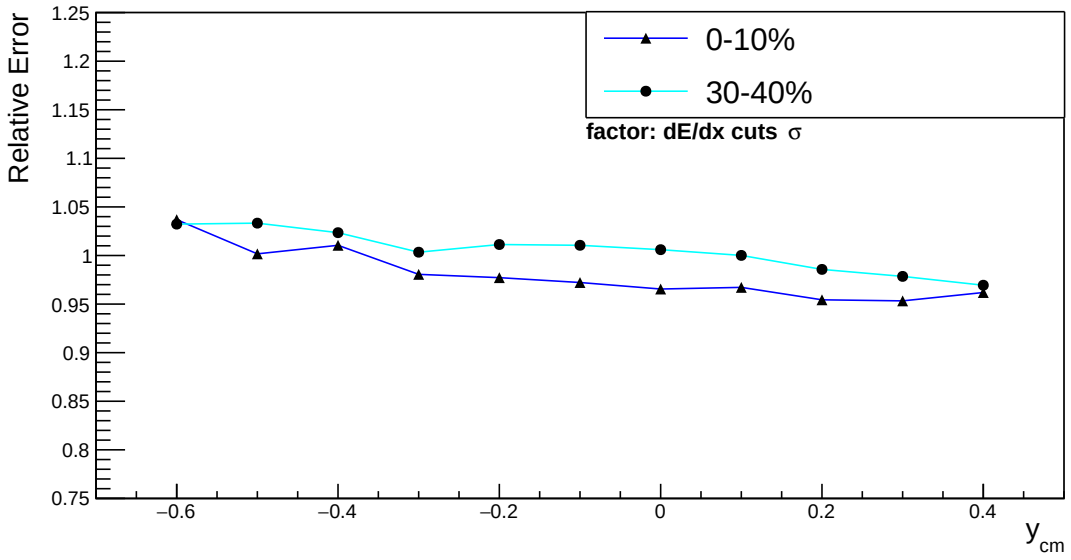

Figure 4.9: Systematic deviations due to the variation of the specific-energy-loss cuts from 3σ to 2σ as function of the center-of-mass rapidity. The variation was done for the most central 10% of analyzed data (blue) and the most peripheral analyzed bin ($30\% - 40\%$) (turquoise).

Systematic Effect of the Mass Integration Window Δ_m

As described in chapter 3.2, the mass spectra are integrated within a 3σ interval around their mean as described in section 3.2. This integration is a possible source of contamination, because even after the particle selection process and background subtraction, other particle species may overlap the deuteron peak.
To further investigate the effect, the cuts were varied to a 2σ width and the resulting rapidity density spectra compared, analogue to the specific energy loss cuts before.
The results are displayed in fig. 4.10. For this estimator, the errors again remain nearly constant for all rapidities and are in good agreement for the different centrality classes, indicating no centrality dependence.
The magnitude of the effect, as estimated by a linear fit, is $\Delta_{m,low} = -1\%$.

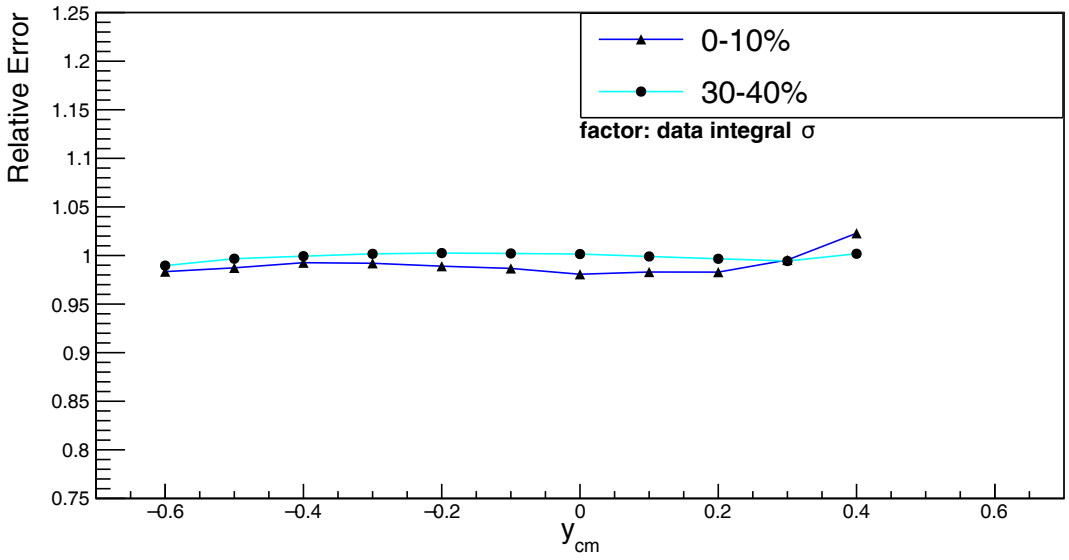

Figure 4.10: Systematic deviations due to the variation of the cuts in the mass spectra from 3σ to 2σ as function of the center-of-mass rapidity. The variation was done for the most central 10% of analyzed data (blue) and the most peripheral analyzed bin ($30\% - 40\%$) (turquoise).

Systematic Effects of the Choice of Simulation Δ_{sim}

As introduced in 2.6.1, two different simulations were available to compare the experimental data to: The two transport based models IQMD and UrQMD. In order to rule out distortions of the identified spectra caused by the choice of simulation, the particle identification process, as described in chapter 3.1.4, was repeated for both approaches and the results compared. Fig. 4.11 shows the resulting width of the upper and lower specific energy loss cuts in the TOF system for both models.

While their differences in the phase space distributions in the detector modules appear small, the overall impact on the resulting rapidity density has to be taken into account.
The resulting bias is shown in Fig. 4.12. Again, the error appears to be constant over the rapidity range and overall independent of the centrality. An estimation by linear fit yields a maximum average systematic error of $\Delta_{sim,low} = -5\%$ for the acceptance and efficiency correction, which can be traced back to the choice of simulation.

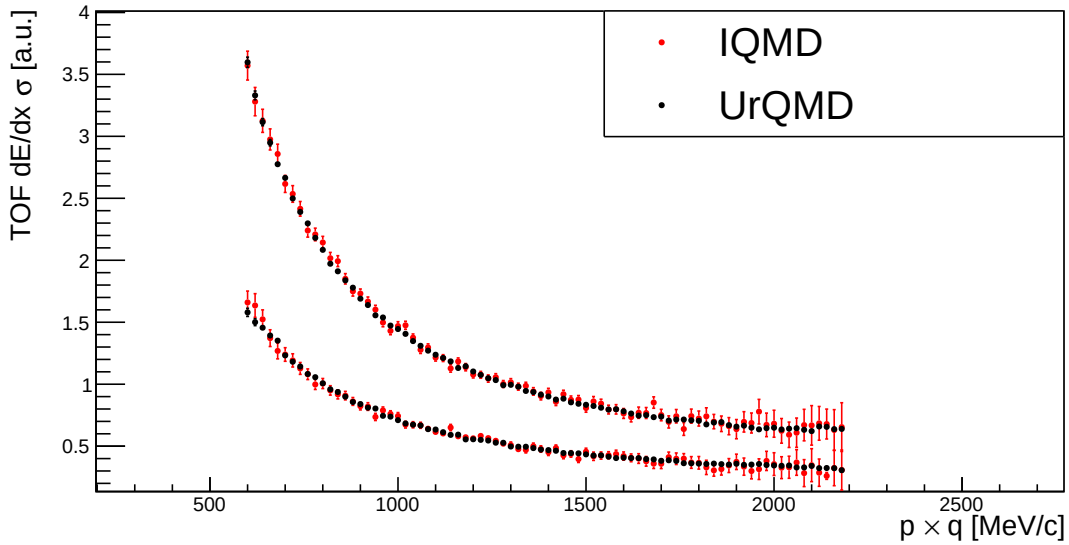

Figure 4.11: Width of the simulated dE/dx cuts in the TOF detector, as obtained by using IQMD (red) and UrQMD (black) simulation

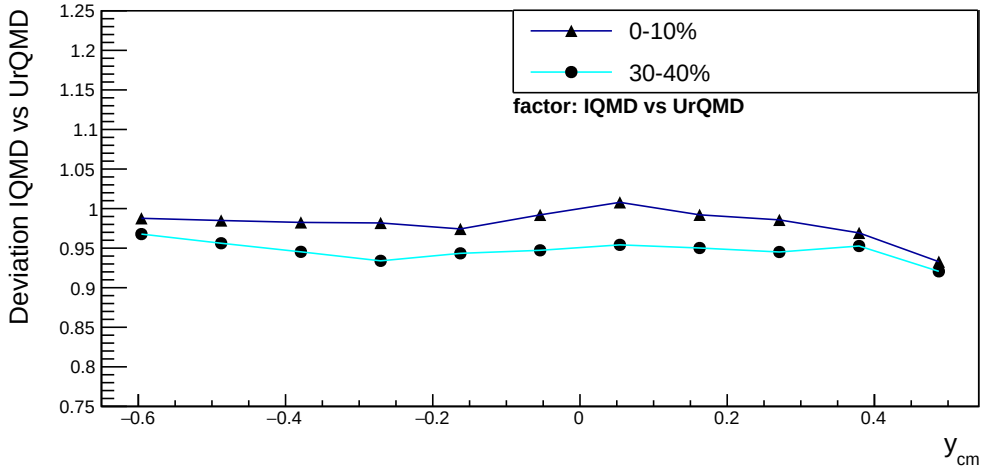

Figure 4.12: Systematic deviations due to the variation of the used simulation from *UrQMD* to *IQMD* as function of the center-of-mass rapidity. The variation was done for the most central 10% of analyzed data (blue) and the most peripheral analyzed bin (30% – 40%) (turquoise).

Systematic Influence of the MDC Sectors Δ_{sec}

Because of high voltage performance issues with MDC sector 2, the analysis was only conducted for particles, that were detected in the remaining 5 sectors. Although they did not experience fluctuations as severe as the second sector, minor deviations can be observed in their responses. The ratios of the rapidity density spectra, normalized to the spectrum of the sum over all 5 sectors (excluding sector 2) are shown in fig. 4.13 for the $0-10\%$ most central events. Except for the bin at the most backward rapidity, which exhibits a negative difference, all sectors fluctuate around the mean. To improve clarity and in order to consider the largest offset, the upper and lower enveloping functions were identified and taken as references. Fig. 4.14 shows the enveloping functions, again for the most central $0-10\%$ and more peripheral $30\%-40\%$ events.
The upper and lower error are in good agreement with being rapidity independent, so the error is again estimated to be constant over the entire rapidity region for all centralities as $\Delta_{sec,upp} = 4.5\%$ and $\Delta_{sec,low} = -4.5\%$. Only the first bin for the 10% most central events differs from this trend.

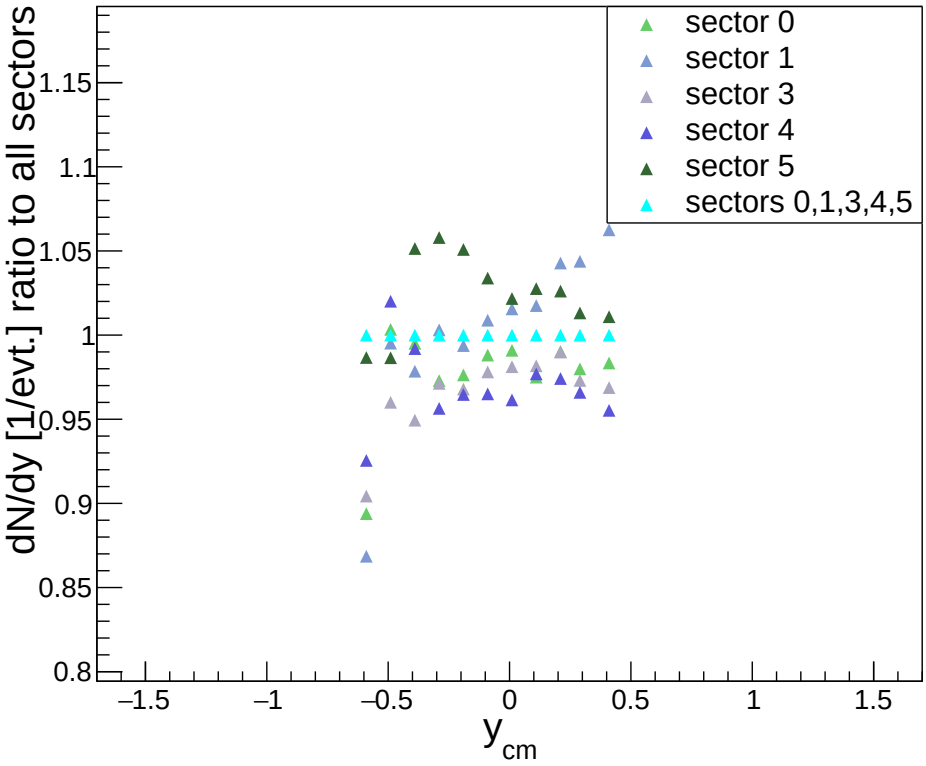

Figure 4.13: Ratio of the rapidity density distribution, as obtained by taking into account only the particles detected in certain sectors, compared to the spectra as detected by all active sectors for 0-10% most central events. Sector 2 is always excluded, because of performance issues.

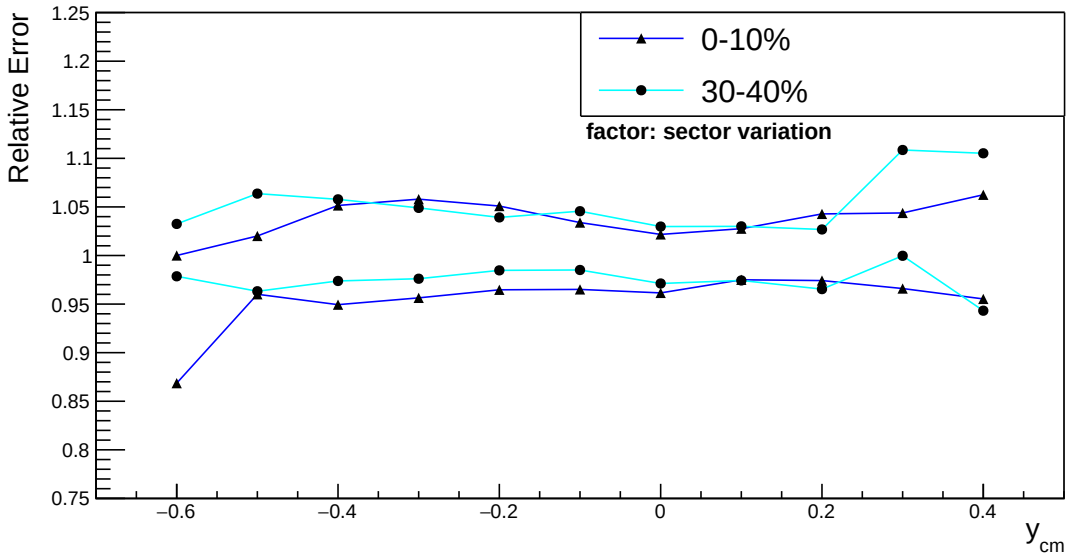

Figure 4.14: Enveloping functions for the systematic error obtained by sector dependence, as shown in fig. 4.13. Analyzed for the most central $0-10\%$ and more peripheral $30\%-40\%$ events.

Systematic Effects of the Siemens-Rasmussen Extrapolation Δ_{extra}

The extrapolation of the measured m_t spectra (fig. 4.1) by fitting with a Siemens-Rasmussen function (Eq. 33) also poses a possibility for systematic uncertainties. Because the global parameters are obtained by a χ^2 mapping, this method also has to be investigated for systematic biases.
Therefore, the χ^2-map (Fig. 4.4) was projected. While the parameter T was set constant at the global minimum, as determined in chapter 4.1.1, a projection along the β_r axis was conducted and for constant β_r, the projection was done along T. The results for the 0-10% most central events are shown in fig. 4.15. Both can be described in good agreement with Gaussian fits, which yield the standard deviations $\sigma_T = 8MeV$ and $\sigma_\beta = 0.013$. Subsequently, the fit of the m_t spectra was repeated with one parameter held constant, while the other was varied by $\pm\sigma$. The resulting fit functions are shown in fig. 4.16 and fig. 4.17.
The trends of the fits stay comparable, while the deviations grow for increasing transverse masses in both cases. However, the contribution of the high transverse momentum to the rapidity density is comparably small, as the count rates are smaller by an order of magnitude.
As it was done for the other systematics, the resulting integrals were compared to the mean values, as shown in fig. 4.18.
For this factor, a dependence on the center-of-mass rapidity becomes visible, as the ratios exhibit a systematic trend with increasing rapidity. In order to take this dependence into consideration, again the enveloping function was determined and used as a rapidity and centrality dependent error, which was newly calculated for each centrality.

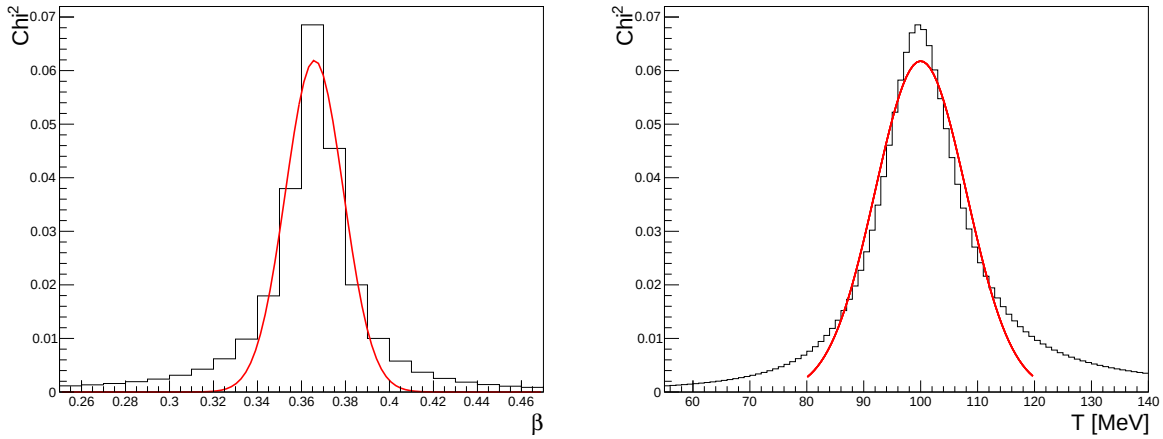

(I) (II)

Figure 4.15: Projection of the χ^2-map for the most central 10% of events (Fig. 4.4). (I) along the β axis for $T = 100MeV$ (II) along the T axis for $\beta = 0.37$. Also indicated are fits with a Gaussian curve (red).

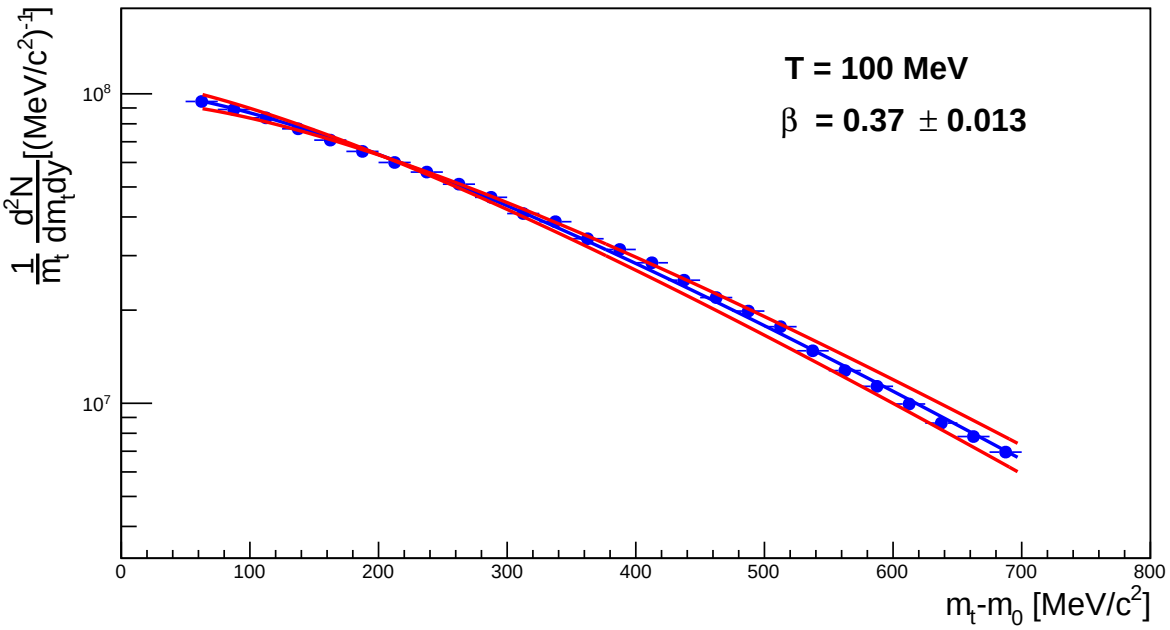

Figure 4.16: m_t-spectrum at midrapidity for the most central 0-10% events, together with fits using the Siemens-Rasmussen function (Eq. 33),where β has been varied within $\pm 1\sigma$ (red) around the reference spectrum (blue), while T is held constant.

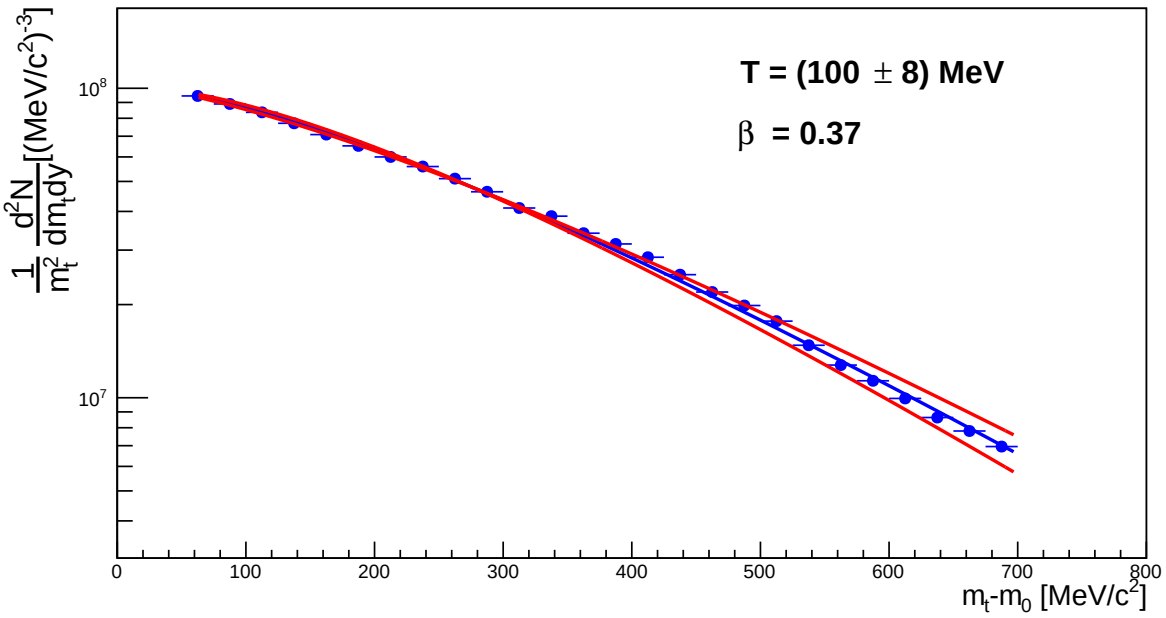

Figure 4.17: m_t-spectrum at midrapidity for the most central 0-10% events, together with fits using the Siemens-Rasmussen function (Eq. 33), where T has been varied within $\pm 1\sigma$ (red) around the reference spectrum (blue), while β is held constant.

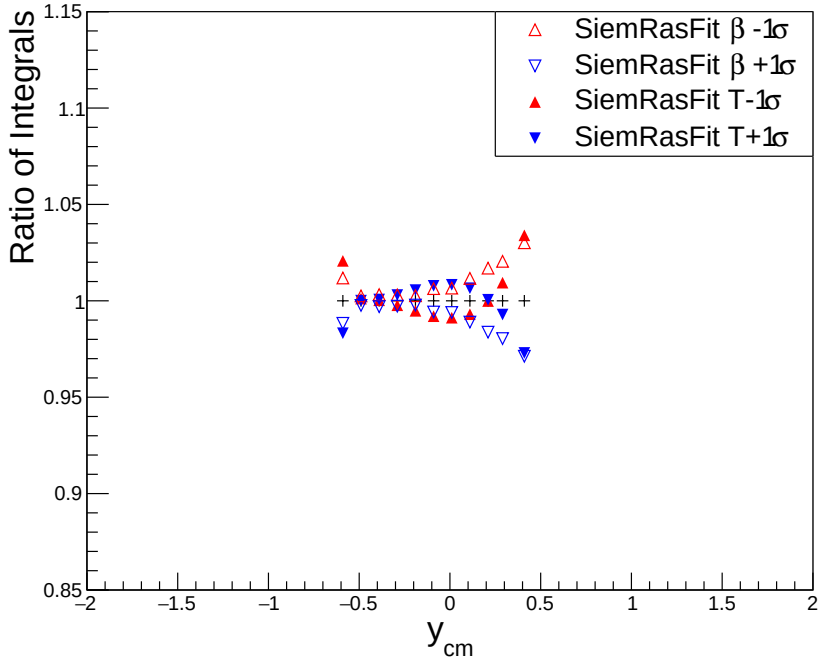

Figure 4.18: Ratios of the integrated yields after variation of the Siemens-Rasmussen parameters compared to the spectra fitted with default parameters.

Overall Systematic Error

Considering all the systematic error sources as introduced above, the overall systematic error Δ_{Sys} of the obtained rapidity density yield[1] can be calculated as the quadratic sum of the relative errors:

$$\Delta_{Sys} = \sqrt{\Delta^2_{dE/dx} + \Delta^2_{sim} + \Delta^2_{m} + \Delta^2_{sec} + \Delta^2_{extra}} \tag{36}$$

For better accuracy, the error is considered separately for an upper $\Delta_{Sys,upp}$ and a lower $\Delta_{Sys,low}$ contribution, yielding an asymmetric error. Respectively, they are:

$$\Delta_{Sys,up}(y) = \sqrt{(0.005)^2 + (0.00)^2 + (0.00)^2 + (0.045)^2 + \Delta^2_{extra}(y)} \approx 5.5\% \tag{37}$$

$$\Delta_{Sys,low}(y) = -\sqrt{(0.02)^2 + (0.05)^2 + (0.01)^2 + (0.045)^2 + \Delta^2_{extra}(y)} \approx 7\% \tag{38}$$

[1]The same procedure was repeated, to obtain the systematic errors of the inverse slope parameter. Naturally, the error of the Siemens-Rasmussen extrapolation was not considered for this evaluation.

5 Discussion

The results obtained during the analysis in this thesis are discussed in different theoretical contexts. The transverse mass spectra and particle yields provide information about the freeze-out characteristics of the system. Considering the thermal interpretation of a static, particle emitting source after the initial collision the inverse slope parameter of the produced m_t spectra can be used to extract information about the kinetic freeze-out temperature (See sec. 5.1).
A *blast-wave* approach also takes into account the collective expansion of the system and incorporates a radial expansion velocity. In this framework, multiple particle species are being described simultaneously to obtain comprehensive information about the system (See sec. 5.2).
To investigate the formation of light nuclei, a simple *nucleon coalescence model* assumption was applied to the resulting data. This theory explains the yields of light nuclei, such as deuterons, to be fixed only by the distribution of their constituent baryons (protons and neutrons) and a coalescence parameter B (See sec. 5.3).

5.1 Effective Temperature

As introduced in chapter 1.2.2, the inverse slope parameter of the Boltzmann-fit (Eq. 31) to the efficiency and acceptance corrected transverse mass spectra at midrapidity might correspond to the kinetic freeze-out temperature T_{kin} of the emitting system. T_{kin} is defined as the temperature, when no further elastic scattering between particles is observed.

The effective temperature of deuterons was measured for the most central 0-20% of events as:

$$T_{eff,\text{deuteron}} = (190.1 \pm 9.5)\ \text{MeV} \tag{39}$$

This effective temperature is higher than the chemical freeze-out temperature T_{chem}, as calculated with a *statistical hadronization model (SHM)* fit to the particle yields [40]. This is a contradiction, as after inelastic interactions cease, particles still can scatter elastically and therefore $T_{chem} \geq T_{kin}$.
To further investigate this effect, different particle species were compared. Fig 5.1 shows the effective temperature as a function of the particles nominal mass. It is clearly visible that the effective temperature rises with increasing particle masses for non strange particles and does not stay constant, which contradicts the expectations of a static source. The deuteron data confirms this trend with the leverage of a considerably higher mass. In order to quantify this observation, the effective temperatures are fitted with a linear function that identifies the kinetic freeze-out temperature T_{kin}.

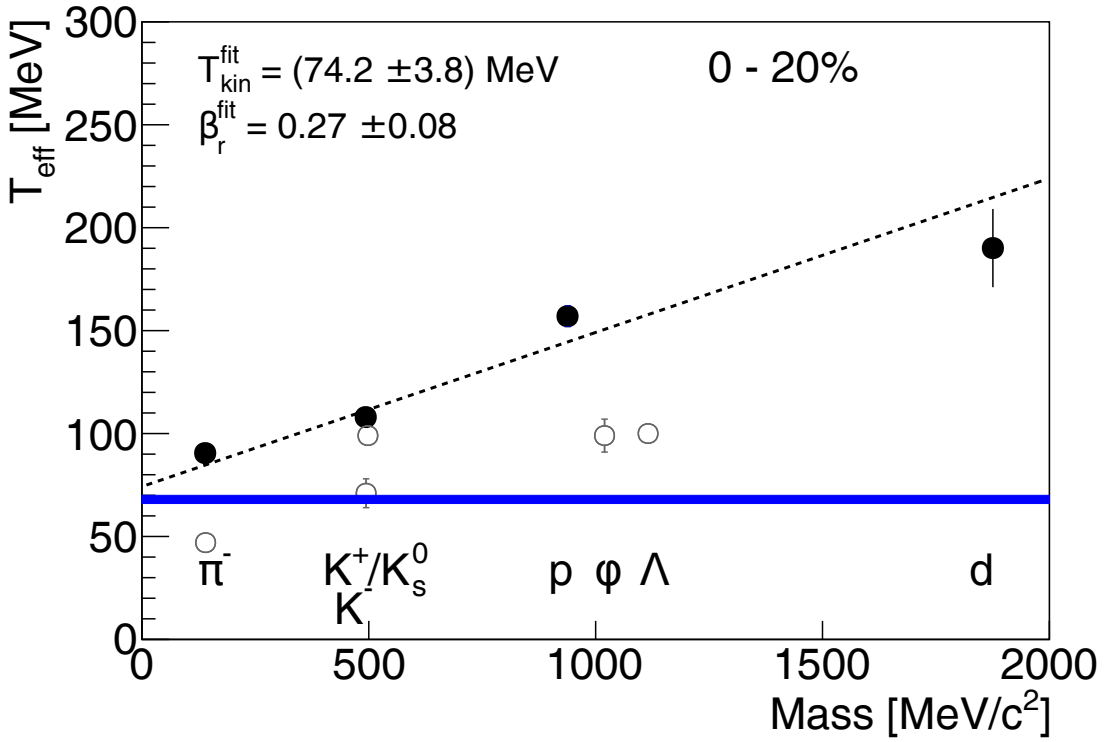

Figure 5.1: Effective temperatures of different particle species with and without strangeness for 0-20% most central events. Pions are represented with two data-points, because their transverse mass spectrum is fitted with two Boltzmann functions to account for resonance-decays in the lower and thermal contributions in the higher m_t regions. The dashed line corresponds to a fit of Eq.40 to the data and the obtained parameters for the kinetic freeze-out temperature T_{kin} and radial flow β_r are indicated in the upper left hand corner. The blue line represents the chemical freeze-out temperature.

However, this observation can be explained with the assumption of an expanding thermal source. To verify this, a mass dependent term is added to the inverse slope parameter proportional to the radial expansion velocity β_r, according to equation 40. Using this simplified assumption, the freeze-out parameters of the system can be obtained by applying a linear fit to the data.

$$T_{eff} = \frac{1}{2} m \beta_r^2 + T_{kin} \tag{40}$$

The fit estimates this parameters to be $T_{kin} = (74.2 \pm 3.8)$ MeV and $\beta_r = 0.27 \pm 0.08$.

5.2 Global Blast-Wave Fit

A description of the transverse flow velocity as being constant is a too simplified scenario. The outermost elements of the expanding media should travel with a significantly higher transverse velocity than the innermost ones. $\beta_r(r_1) > \beta_r(r_2)$ should hold true for $r_1 > r_2$.
A more exact representation of the velocity profile is employed in the *Blast-Wave* model, as described in [14]. The model assumes particles to suddenly decouple from a thermal system with temperature T. They then expand with a cylindrical symmetry, which is boost-invariant in longitudinal and follows a velocity field in transverse direction. The differential cross section for deuterons is predicted to follow the form:

$$\frac{1}{m_t}\frac{d^2N}{dm_t dy} = \int_0^{R_G} A m_t K_1\left(\frac{m_t \cosh(\rho)}{T}\right) I_0\left(\frac{p_t \sinh(\rho)}{T}\right) r\mathrm{d}r \tag{41}$$

with A being a constant, $\rho(r) = \tanh^{-1}(\beta_r(r))$, K_1 and I_0 are two modified Bessel functions and the transverse geometric radius of the source is denoted by R.
The transverse velocity field $\beta_r(r)$ can be derived as:

$$\beta_r(r) = \beta_s\left[\frac{r}{R}\right]^n \tag{42}$$

To represent a linear profile, n was then set to 1.
In order to compare the radial flow profiles, the average transverse expansion velocity $\langle\beta_r\rangle$ was considered. In the case of a uniform particle density,it can be calculated as:

$$\langle\beta_r\rangle = \frac{2}{3}\beta_s \tag{43}$$

Fig. 5.2 shows the differential cross sections of various particle species measured in the Au+Au collisions at 1.23AGeV for the most central 10% of events to which the fit, according to Eq. 41, was applied [41]. For this comparison the deuterons that were analyzed in this thesis are compared to the m_t spectra of particle species originating from other analyses. A systematic uncertainty of 10% was assumed for the Φ, 6.7% for the deuterons, and 5% for all other species. These errors were then added quadratically to the statistical ones. For the simultaneous fit, the parameters T and $\langle\beta_r\rangle$ were held as global parameters.
The deuterons, which are represented by the uppermost spectra, are well described by the theoretical curve. The other particle species included in the fit also follow the global trend within their errors. Only the very light π^+ and π^- particles exhibit a deviation for low transverse momenta, as in this region their spectra are dominated by contributions from resonance decays. Therefore, only their contributions above $m_t - m_0 > 400$ MeV/c are included in the fit, which is indicated in the figure by larger data points.
Fig. 5.3 shows the global parameters T and $\langle\beta_r\rangle$ that are extracted from the fit. They are estimated to be $T = (68 \pm 1)$ MeV and $\langle\beta_r\rangle = 0.341 \pm 0.003$.
The results obtained by the simultaneous fits are still subject to uncertainties, as different particle species might, due to their different hadronic cross sections, decouple from the system at differing times. Therefore, the global parameters are only a simplified assumption to characterize the system.

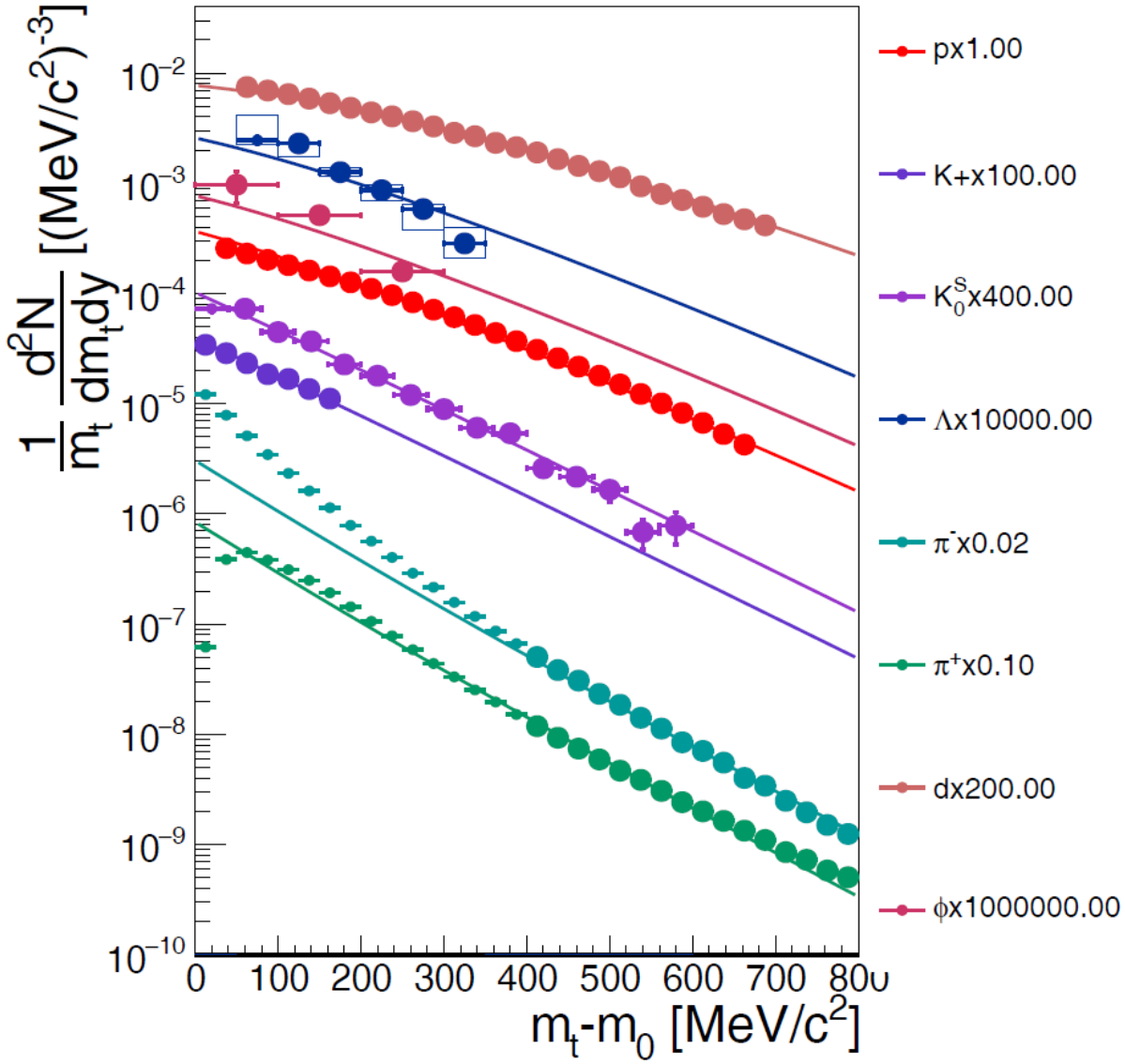

Figure 5.2: Global fit with a Blast-Wave function (Eq. 41) with parameters T and $\langle\beta_r\rangle$ to the differential cross section of different particle species, measured for the most central 10% of events around mid-rapidity in Au+Au collisions at 1.23AGeV with HADES. Only large data points are considered for the fit. The spectra are scaled with arbitrary constants for better visibility, as indicated on the right.

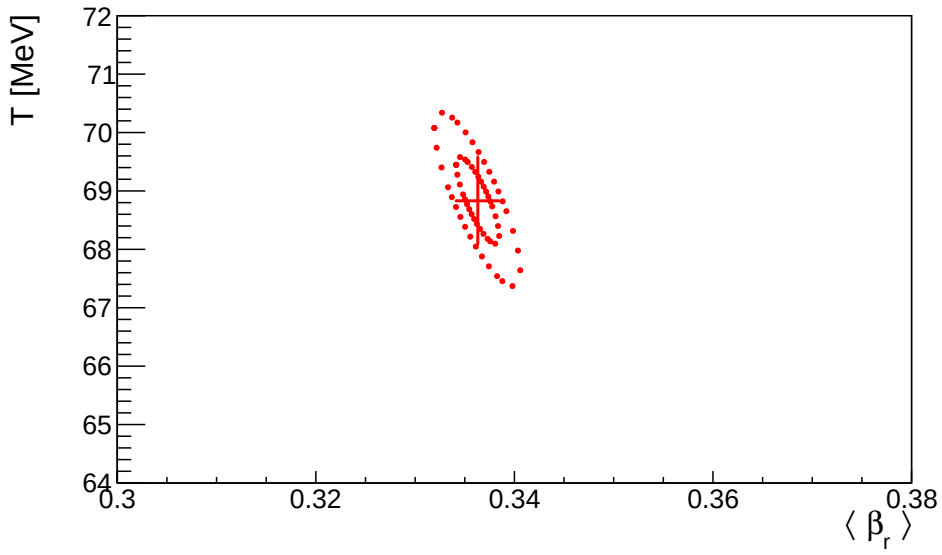

Figure 5.3: Parameters of the global Blast-Wave (Eq. 41) fit, including deuterons, as shown in Fig. 5.2. Besides the statistical error bars, the 1σ and 2σ confidence levels are indicated by dashed lines.

In order to estimate the influence of the deuteron data on the global characteristics, the fit was repeated for the same set of particle species, exluding deuterons.
It exhibits a similar behavior. The resulting fit parameters T and $\langle\beta_r\rangle$ are shown in fig. 5.4. They are extracted as $T = (65 \pm 1)$ MeV and $\langle\beta_r\rangle = 0.356 \pm 0.004$.
Including deuterons in the analysis decreases the expansion velocity while the emission temperature of the system increases. Due to their higher mass, they might be more sensitive to the effects of radial flow.
In an earlier analysis of the simultaneous fit, the parameters of the Blast-Wave were found to be $T = 62 \pm 10$ MeV and $\langle\beta_r\rangle = 0.36 \pm 0.04$ [41]. These results are within the systematic errors in good agreement with the parameters extracted in this thesis.
As shown in fig. 5.5, they follow the trend of the world data, obtained by other experiments at various beam energies $\sqrt{s_{NN}}$. With increasing energy of the collision system, the temperature rises, but reaches an almost constant maximum temperature of about 160 MeV that only increases marginally for energies above 40 GeV. The transverse expansion velocity $\langle\beta_r\rangle$ increases over the entire observed energy range.

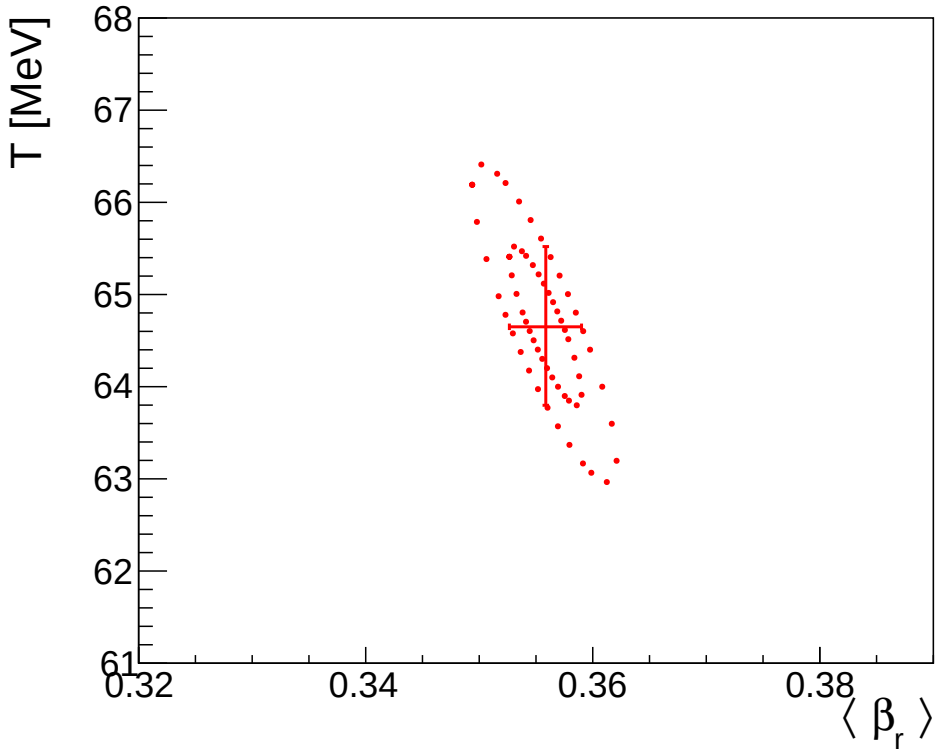

Figure 5.4: Parameters of the global Blast-Wave (Eq. 41) fit, excluding deuterons, as shown in Fig. 5.2. Besides the statistical error bars, the 1σ and 2σ confidence levels are indicated by dashed lines.

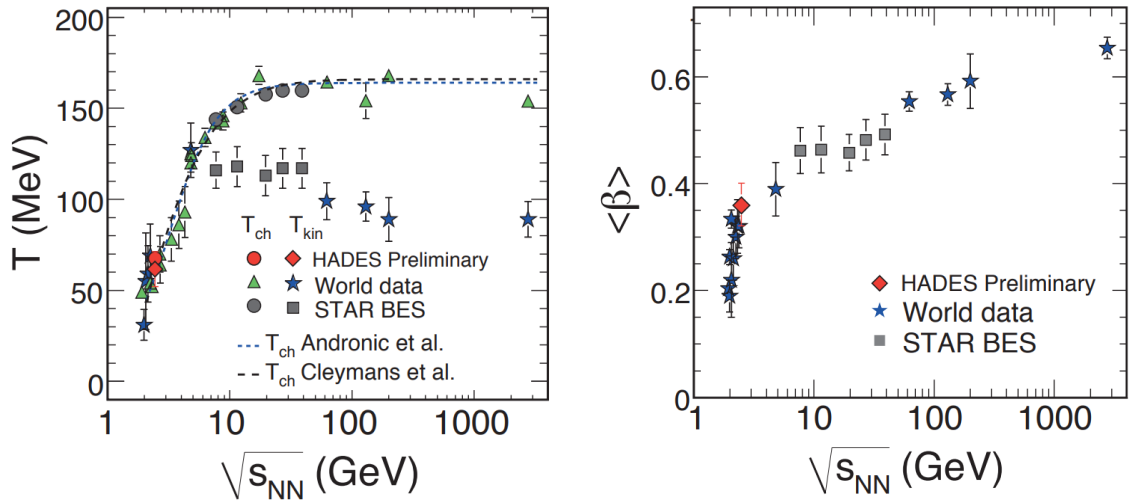

Figure 5.5: Temperature T (left) and mean transverse velocity $\langle\beta_r\rangle$ (right) as function of the beam energy $\sqrt{s_{NN}}$. HADES data as presented at Quark Matter conference 2017 [41]. STAR and world data taken from [42]

5.3 Nucleon Coalescence Model

Light nuclei, such as deuterons, have a small binding energy ($\approx$ 2.2 MeV for deuterons, see table 2 and can therefore not stay bound during the extreme conditions of multiple scatterings that occur during heavy ion collisions at the present energies. Consequently, they have to be formed during the freeze-out stage of the hot and dense matter. As described in chapter 1.2.1, the *Nucleon Coalescence Model* provides an description for the formation of deuterons by recombination of a proton and neutron with small relative momentum. Under the assumption that the invariant proton yield is identical to that of the neutrons, the invariant yield of the produced deuteron can be derived as:

$$\frac{1}{2\pi(p_t/A)}\frac{\mathrm{d}^2N_A}{\mathrm{d}y_{cm}\mathrm{d}(p_t/A)} = B_A\left[\frac{1}{2\pi p_t}\frac{\mathrm{d}^2N_p}{\mathrm{d}y_{cm}\mathrm{d}p_t}\right]^A|_{p=n} \tag{44}$$

where y^{cm} is the respective center-of-mass rapidity y_{cm}. The conversion to the Lorentz-invariant transverse momentum $p_t = \sqrt{p_x^2 + p_y^2}$ can then be calculated as:

$$p_t = \sqrt{m_t^2 - m_0^2}. \tag{45}$$

Fig. 5.6 shows the efficiency and acceptance corrected invariant deuteron and proton spectra at midrapidity for the most central 10% of events as function of the transverse momentum divided by the number of nucleons A. The region around midrapidity was chosen, because the contamination of spectator fragments is minimized.
After this scaling, the invariant transverse momentum spectra of the protons appear to exhibit a less pronounced curvature than that of the deuterons.

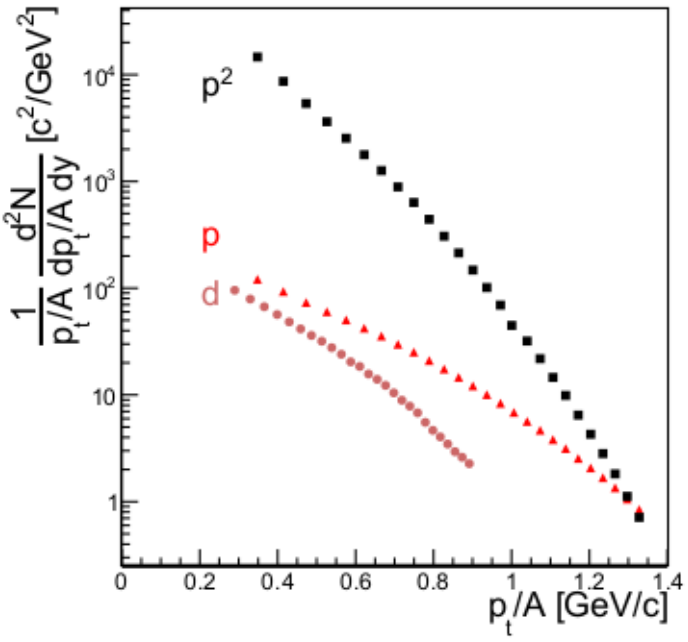

Figure 5.6: Invariant spectra of deuterons and protons at midrapidity as function of p_t, divided by the number of nucleons A for the most central 0-10% of events, originating from Au+Au collisions at 1.23A GeV. Also included is the squared proton spectrum, indicated with black squares. Data for the proton spectra taken from [16].

Eq. 44 now allows for a calculation of the coalescence factor B_A, where $A = 2$. Using Eq. 45, B_2 is shown as a function of the transverse mass $m_t - m_0$ in Fig. 5.7 for the most central 10% of events.
It is observed that the trend of the data can be well described by an exponential fit

$$B_2(m_t) = a \exp\left[c(m_t - m_0)\right] \tag{46}$$

as indicated by the solid line in the figure. For increasing transverse mass values, the coalescence probability B_2 also rises. As deuterons are formed not before freeze-out, they have not directly experienced the force of the expanding motion. Instead, they contain the accumulated flow effects of their constituent nucleons which leads to a higher inverse slope. The relatively higher abundance of protons for high transverse masses leads to an increase in the coalescence parameter.

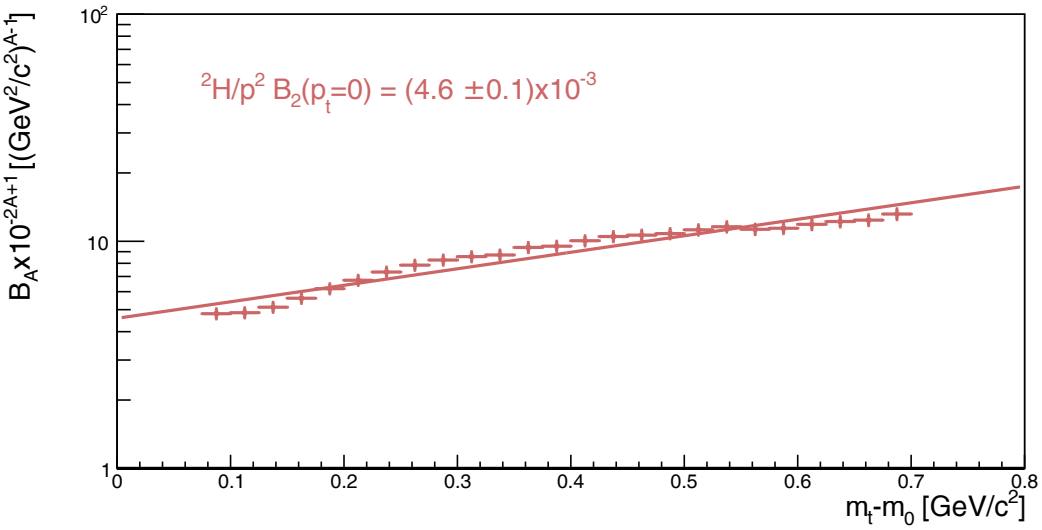

Figure 5.7: Coalescence parameter B_A for $A = 2$ as function of the transverse mass $m_t - m_0$ for the most central 10% of events fitted with an exponential function according to Eq. 46. Also indicated is the value of B_2 at $p_t = 0$.

Different experiments have published the coalescence parameter B_2 for their respective beam energies, measured in various phase space regions because of differing rapidity and transverse momentum coverage. According to [43], the parameter B_2 is extracted at $p_t = 0$. Therefore, the coalescence parameter equals the parameter a of the exponential fit, applied to the data in Fig. 5.7. It follows that $B_2(p_t = 0) = (4.6 \pm 0.1) \times 10^{-3}$ GeV$^2/c^3$ for Au+Au at a collision energy of 1.23AGeV.

In order to verify the validity of this result, the coalescence parameter B_2 was also calculated by another approach, using the rapidity density distribution, as explained in chapter 1.2.1. As B_2 depends on the total invariant yield of deuterons and protons, a comparison of the full yield, as obtained by integrating the rapidity density distribution was conducted.
Fig 5.8 shows the rapidity density distribution of the deuterons originating from the most central 10% of events, normalized to the number of analyzed events. The distribution was fitted by a Gaussian function to extrapolate the data to unmeasured rapidity regions. This function was then integrated and the total yield $N_{\mathrm{tot,deut}} = (34 \pm 1)$ deuterons per event extracted. This yield

was then compared to the invariant proton yield $N_{\text{tot,p}} = 87$ protons per event, as measured in [16]. The coalescence parameter $B_{2,\text{integral}}$ then directly follows as:

$$B_{2,\text{integral}} = \frac{34}{87^2} = (4.5 \pm 0.1) \times 10^{-3} \tag{47}$$

which, within the errors, is identical with the previously calculated $B_2(p_t = 0) = (4.6 \pm 0.1) \times 10^{-3}$.

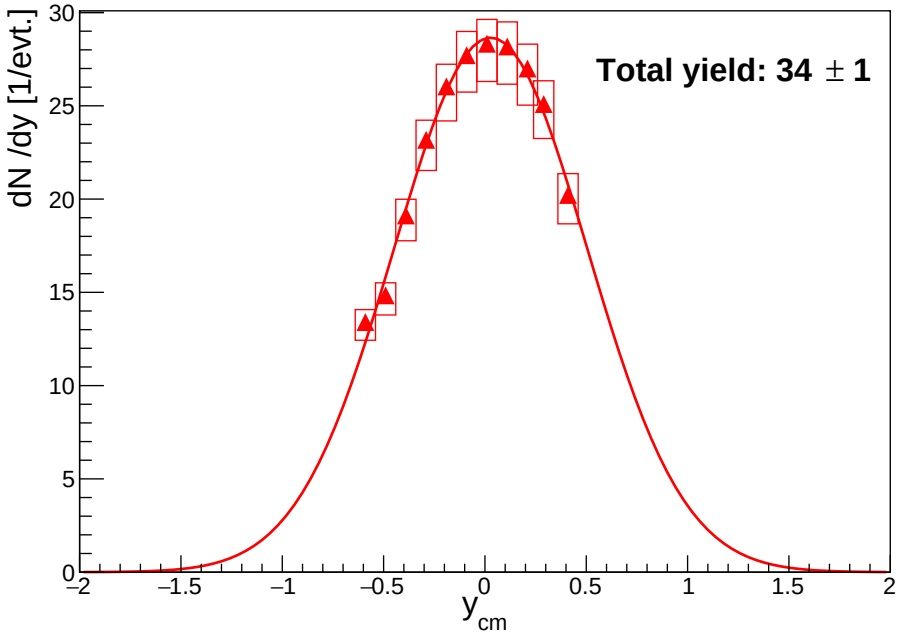

Figure 5.8: Rapidity density distribution for the most central 10% of events normalized to the number of analyzed events with systematic errors indicated. Also included is a Gaussian fit to the data points.

As further reference, the coalescence at mid-rapidity was extracted by comparing the invariant yield of deuterons at midrapidity $N_{y_{cm},\text{deut}} = 28 \pm 2$ deuterons per event to that of protons of $N_{y_{cm},\text{prot}} = 68 \pm 4$ protons per event [16]. Then the coalescence parameter at midrapidity $B_{2,y_{cm}}$ is

$$B_{2,y_{cm}} = \frac{28}{68^2} = (6.0 \pm 0.7) \times 10^{-3} \tag{48}$$

While still in the same order of magnitude, this result differs from the ones obtained by evaluation of the m_t spectra at $p_t = 0$ and extrapolation of the rapidity density by about 50%. All three measurements can be compared with the data from other experiments: (FOPI Ru+Ru at 0.4 and 1.528AGeV [20], EOS Au+Au at 1.15AGeV [44], AGS E878 Au+Au at 10.8AGeV [45], AGS E877 Au+Au at 15AGeV [46] and NA49 Pb+Pb at $20, 30, 40, 80$ and 158AGeV [43]).
Fig. 5.9 displays the B_2 values for central collisions, calculated by various experiments at different beam energies and in different collision systems. These measurements indicate a decrease of the coalescence parameter with increasing beam energy, spanning over almost 2 orders of magnitude. The new HADES result, obtained in this analysis, further confirms this trend.
All results however still contain the bias introduced with the assumption of identical proton and neutron invariant yields. Multiple rescattering effects are believed to change the yields over the evolution of the collision [47].

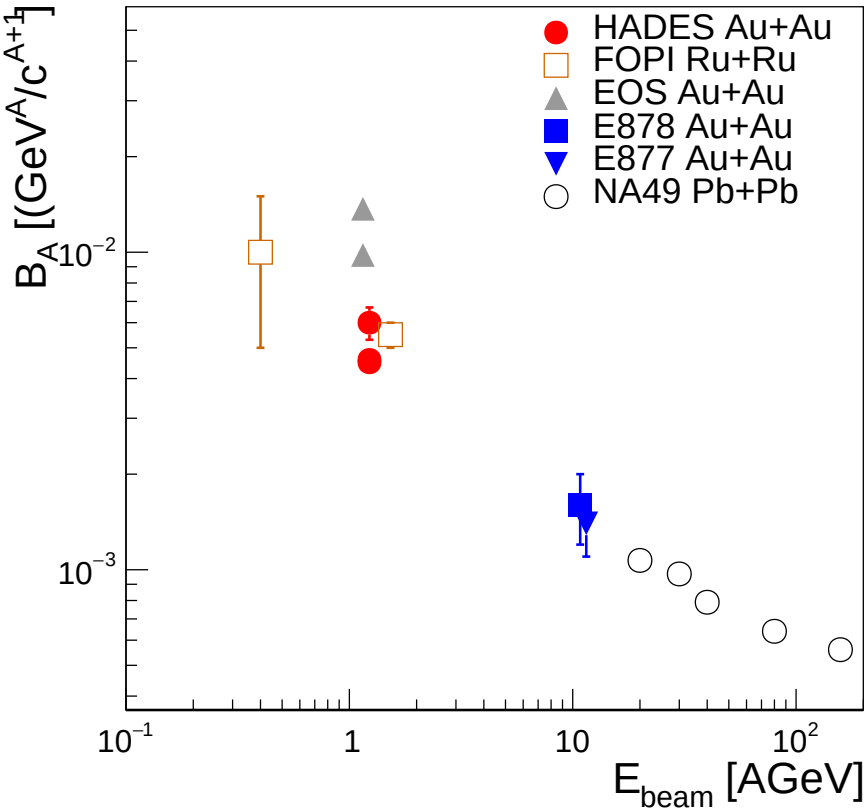

Figure 5.9: Coalescence parameter B_2 of the HADES Au+Au data at 1.23AGeV at midrapidity for $A = 2$ shown in comparison with results from FOPI Ru+Ru at 0.4 and 1.528AGeV [20], EOS Au+Au at 1.15AGeV [44], AGS E878 Au+Au at 10.8AGeV [45], AGS E877 Au+Au at 15AGeV [46] and NA49 Pb+Pb at $20, 30, 40, 80$ and 158AGeV [43] as function of the beam energy E_{Beam}.

6 Summary and Outlook

In this thesis, studies of the deuteron production in Au+Au collisions at 1.23AGeV, measured by the HADES experiment in April and May 2012, are presented. It is shown that deuterons can be reconstructed from the data with high statistics. Improvements of the data purity are achieved by cuts in the specific energy loss and momentum distributions. The remaining background is due to contaminating signals of other particles like ^{4}He and can be subtracted. The corrections for the detector's acceptance and efficiency are based on simulations with the transport models UrQMD and IQMD, the thermal Pluto model and a HGEANT detector simulation.

The obtained transverse mass spectra at mid-rapidity are fitted with a Boltzmann function to extract the inverse slope parameter, which in a static thermal system corresponds to the kinetic freeze-out temperature and is often called the effective temperature. The resulting $T_{Eff} = (190 \pm 10)$ MeV is found to exceed the chemical freeze-out temperature of $T_{chem} = 69 \pm 1$ MeV as calculated by an SHM fit to different particle yields. When this measurement is compared to the results from previous analyses of other particle species, a trend of rising effective temperature with increasing particle mass is observed. This leads to the assumption of a radial expansion of the thermal system, characterized by the radial expansion velocity β_r. Studies of heavier fragments, such as tritons, could provide further leverage to confirm this trend.
Subsequently, the m_t spectra are fitted with Siemens-Rasmussen functions, which provide a better description of the distributions, and the global parameters $T = (100 \pm 8)$ MeV and $\beta_r = 0.37 \pm 0.01$ are extracted for the most central 10% of events. This analysis is repeated for the three centrality classes $10 - 20\%$, $20 - 30\%$ and $30 - 40\%$.

These fits of the transverse mass spectra are used to extrapolate them into unmeasured m_t regions, so that the rapidity density yield for the four studied centrality classes can be determined. For the 10% most central events the rapidity density follows a thermal shape, while the more peripheral events exhibit a stronger influence of spectator particles.
A simultaneous fit of a blast-wave function to the deuteron transverse mass spectra and various lighter particles is performed to study the global freeze-out characteristics of the system. By including particles with lower masses and assuming a common freeze-out temperature, the resulting global kinetic freeze-out temperature $T_{kin} = (68 \pm 1)$ MeV is considerably lower than the temperature extracted from the Siemens-Rasmussen fits. As the blast-wave function that was used for the fit assumes a linear velocity profile of β_r, an average expansion velocity $\langle\beta_r\rangle = 0.342 \pm 0.003$ is extracted. These parameters are compared to results from previous experiments and agree with the trend of the world data. Including more particles in the simultaneous fit can improve the validity of the global parameters.

Investigations of the nuclei formation process, according to a nucleon coalescence model, are conducted. The invariant yield of the deuterons, as function of the transverse momentum p_t is divided by the squared invariant yield of protons, as obtained in a previous analysis. The result is the coalescence parameter $B_2 = (4.6 \pm 0.1) \times 10^{-3}$ for $p_t = 0$. This study is extended by integrating the rapidity density for the most central 10% of events and dividing the resulting (34 ± 1) deuterons/event by the squared integrated invariant yield of (87 ± 1) protons/event. The resulting coalescence parameter $B_{2,\text{integral}} = (4.5 \pm 0.1) \times 10^{-3}$ agrees with the previous calculation. At mid-rapidity, the direct comparison of the deuteron yield of (28 ± 2) deuterons per event and squared proton yield of (68 ± 4) protons/event lead to a coalescence parameter of $B_{2,y_{cm}} = (6.0 \pm 0.7) \times 10^{-3}$, which deviates from the other calculations by approximately 50%, but is in the same order of magnitude. This deviation was to be expected, as the calculations

consider different regions of the phase space. The results are set in context with the results from other experiments and confirm the predictions.
Studies of heavier nuclei with $A > 2$ can be used to determine further coalescence parameters B_A and confirm the predictions of the nucleon coalescence model.

7 Supplemental Material

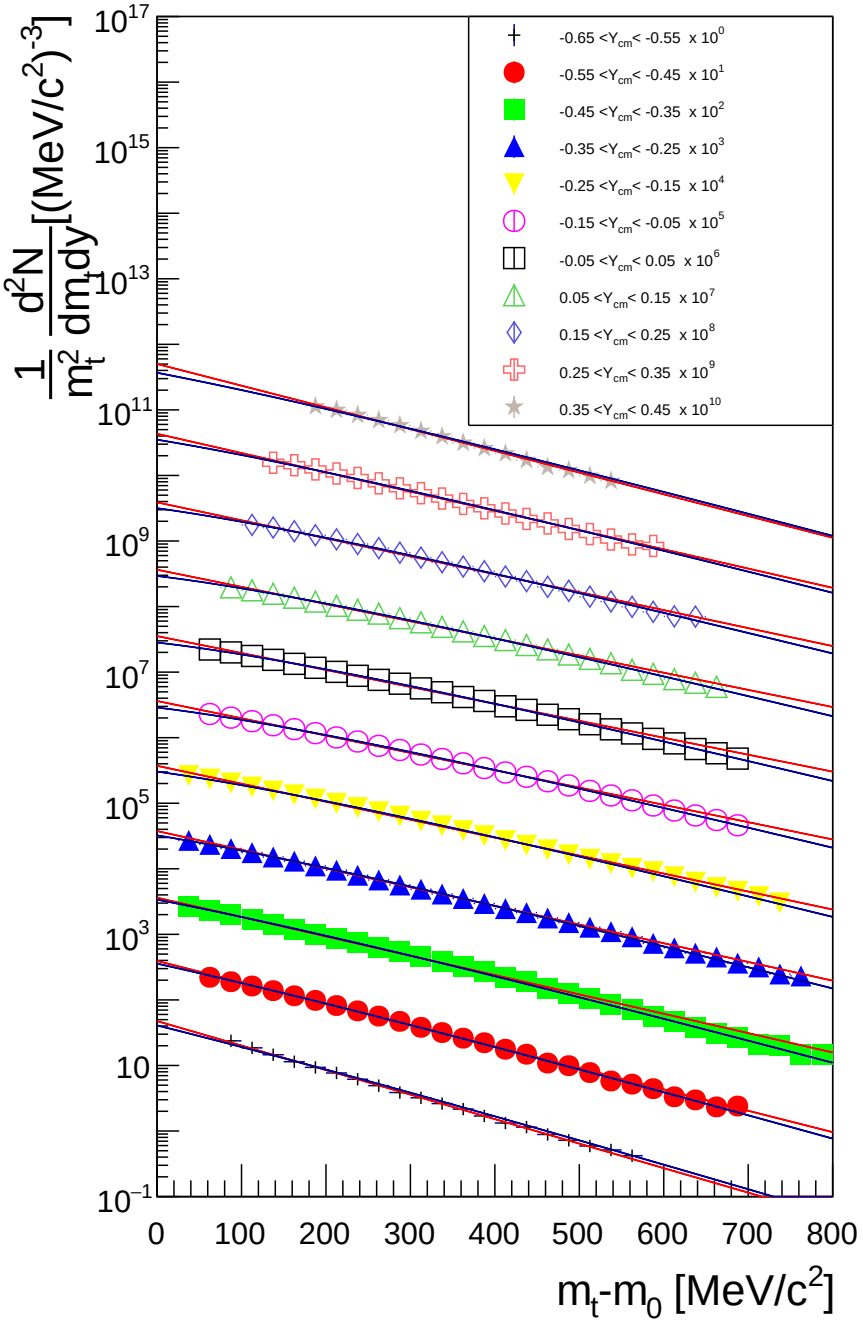

Figure 7.1: Efficiency and acceptance corrected transverse mass spectra of deuterons for the 10-20% most central events, scaled by $1/m_t^2$. For better visibility, each spectrum is multiplied by a power of 10, as indicated in the legend. Also drawn are fits with a *Boltzmann* (red, Eq. 31) and *Siemens Rasmussen* (blue, Eq. 33) function.

.

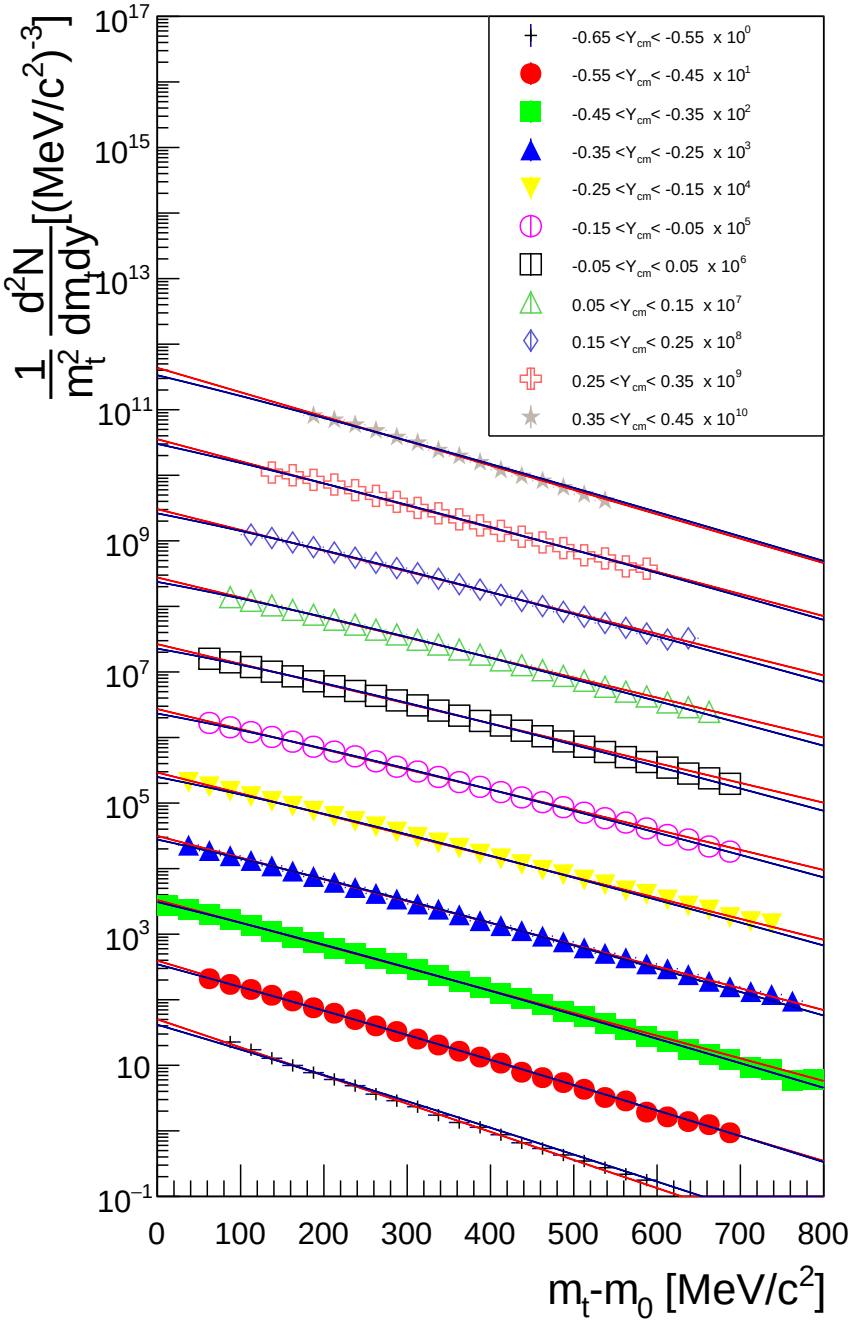

Figure 7.2: Efficiency and acceptance corrected transverse mass spectra of deuterons for the 20-30% most central events, scaled by $1/m_t^2$. For better visibility, each spectrum is multiplied by a power of 10, as indicated in the legend. Also drawn are fits with a *Boltzmann* (red, Eq. 31) and *Siemens Rasmussen* (blue, Eq. 33) function.

.

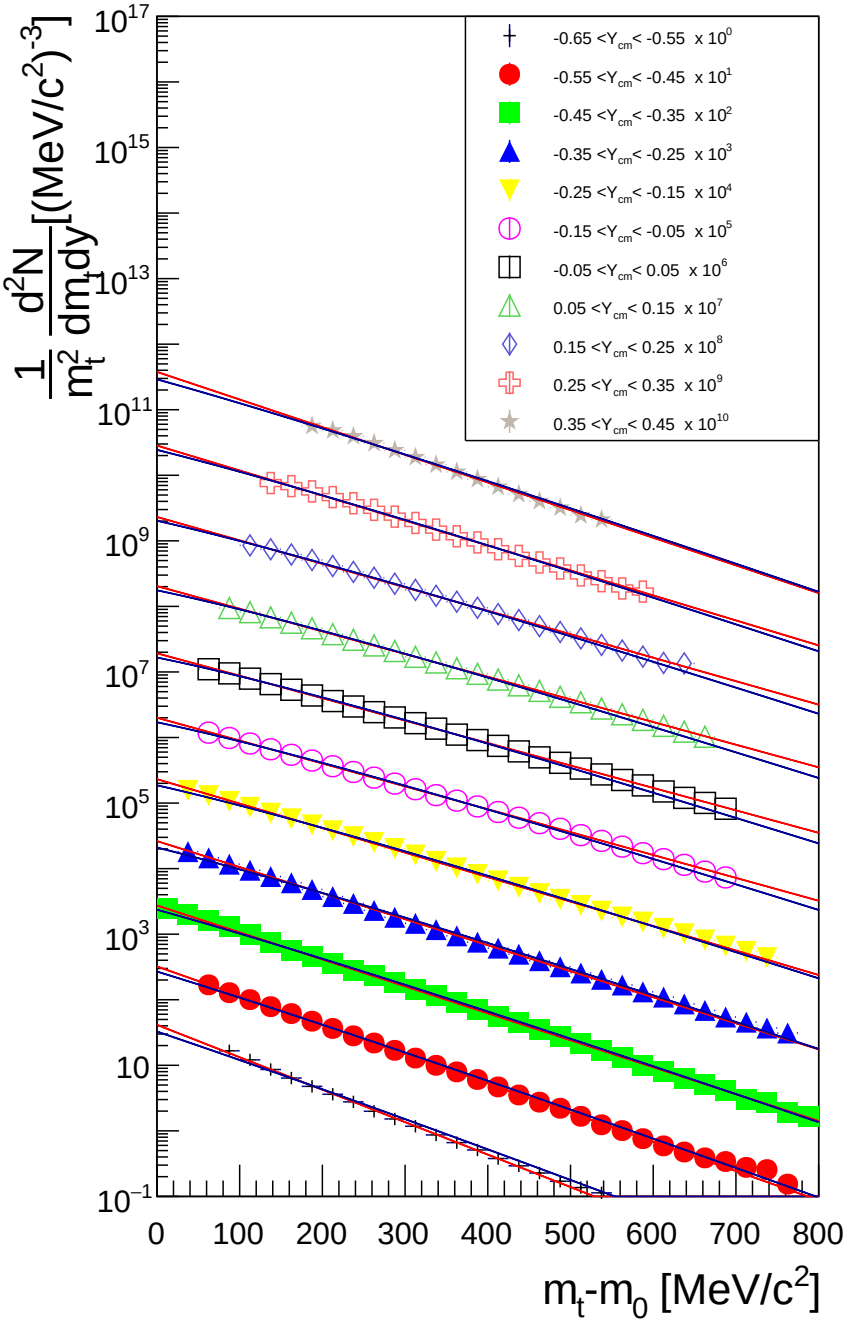

Figure 7.3: Efficiency and acceptance corrected transverse mass spectra of deuterons for the 30-40% most central events, scaled by $1/m_t^2$. For better visibility, each spectrum is multiplied by a power of 10, as indicated in the legend. Also drawn are fits with a *Boltzmann* (red, Eq. 31) and *Siemens Rasmussen* (blue, Eq. 33) function.

.

List of Figures

References

[1] U. Heinz, "The strongly coupled quark–gluon plasma created at rhic," *Journal of Physics A: Mathematical and Theoretical*, vol. 42, no. 21, p. 214003, 2009.

[2] G. Aad *et al.*, "Observation of a new particle in the search for the standard model higgs boson with the atlas detector at the lhc," *Physics Letters B*, vol. 716, no. 1, pp. 1 – 29, 2012.

[3] MissMJ,Wikimedia Commons, "Standard model of elementary particles," 2017. [`https://commons.wikimedia.org/wiki/File:Standard_Model_of_Elementary_Particles.svg`; accessed Sep 14, 2017].

[4] A. Chodos, R. L. Jaffe, K. Johnson, C. B. Thorn, and V. F. Weisskopf, "New extended model of hadrons," *Phys. Rev. D*, vol. 9, pp. 3471–3495, Jun 1974.

[5] P. Colangelo and A. Khodjamirian, *QCD Sum Rules, a Modern Perspective*, pp. 1495–1576. World Scientific Publishing Co, 2001.

[6] D. H. Rischke, "The quark-gluon plasma in equilibrium," *Progress in Particle and Nuclear Physics*, vol. 52, pp. 197–296, Mar. 2004.

[7] T. Galatyuk, *Di-electron spectroscopy in HADES and CBM: from p + p and n + p collisions at GSI to Au + Au collisions at FAIR*. Dissertation, Johann Wolfgang Goethe-Universitaet Frankfurt am Main, 2009.

[8] B. C. Barrois, "Superconducting quark matter," *Nuclear Physics B*, vol. 129, no. 3, pp. 390 – 396, 1977.

[9] B. Kardan, *Centrality Determination and HADES ECAL Readout-Electronics*. Diploma thesis, Johann Wolfgang Goethe-Universitaet Frankfurt am Main, 6 2015.

[10] S. T. Butler and C. A. Pearson, "Deuterons from high-energy proton bombardment of matter," *Phys. Rev.*, vol. 129, pp. 836–842, Jan 1963.

[11] R. Scheibl and U. Heinz, "Coalescence and flow in ultrarelativistic heavy ion collisions," *Phys. Rev. C*, vol. 59, pp. 1585–1602, Mar 1999.

[12] B. Hong, "Critical evidence for nucleon coalescence in heavy-ion collisions at 400 mev per nucleon," *Journal of the Korean Physical Society*, vol. 51, pp. 1640–1644, Nov 2007.

[13] *Electromagnetic and Hadronic Probes of Nuclear Matter: Proceedings of the TAPS Workshop IV, Sept. 14-20, 1997, Mont Saint Odile, Fr (DISC, Elche, Spain, September 2009)*, (Biarrity, France), Atlantica Séguier Frontières, 1998.

[14] G. E. Bruno, "Transverse mass distributions of strange particles produced in Pb-Pb collisions at 158 A GeV/c," *ArXiv Nuclear Experiment e-prints*, Nov. 2003.

[15] H. Schuldes, *Produktion leichter Fragmente in Ar+KClKollisionen bei 1,76A GeV*. Master thesis, Johann Wolfgang Goethe-Universitaet Frankfurt am Main, 2012.

[16] H. Schuldes, *Charged Kaon and Φ Reconstruction in Au+Au Collisions at 1.23 AGeV*. PhD thesis, Johann Wolfgang Goethe-Universitaet Frankfurt am Main, 2017.

[17] P. Huovinen, P. F. Kolb, U. Heinz, P. V. Ruuskanen, and S. A. Voloshin, "Radial and elliptic flow at RHIC: further predictions," *Physics Letters B*, vol. 503, pp. 58–64, Mar. 2001.

[18] P. Braun-Munzinger, K. Redlich, and J. Stachel, *Particle Production in Heavy Ion Collisions*, pp. 491–599. World Scientific Publishing Co, 2004.

[19] H. Oeschler, J. Cleymans, B. Hippolyte, K. Redlich, and N. Sharma, "Thermal Model Description of Collisions of Small Nuclei," *ArXiv e-prints*, Mar. 2016.

[20] M. S. Ryu, *Production of the proton and light fragments in* ${}^{96}_{44}Ru+{}^{96}_{44}Ru$ *collisions at SIS18 energies and the multigap Resistive Plate Chamber.* PhD thesis, Graduate School Korea University, 2009.

[21] P. Salabura, "HADES: A High Acceptance DiElectron Spectrometer," *Acta Phys. Polon.*, vol. B27, pp. 421–440, 1996.

[22] G. H. für Schwerionenforschung GmbH, "Aufbau des HADES-Experiments, Website." `https://www.gsi.de/fileadmin/_migrated/pics/Target_Hades.jpg`, 2017. [Online; accessed 26-November-2017].

[23] A. A. Watson, "The discovery of Cherenkov radiation and its use in the detection of extensive air showers," *Nuclear Physics B Proceedings Supplements*, vol. 212, pp. 13–19, Mar. 2011.

[24] A. et al, "The high-acceptance dielectron spectrometer HADES," *The European Physical Journal A*, vol. 41, no. 2, pp. 243–277, 2009.

[25] T. Bretz, "Magnetfeldeigenschaften des Spektrometers HADES," Master's thesis, TU München, München, 1999.

[26] D. J. Markert, *Untersuchung zum Ansprechverhalten der Vieldraht-Driftkammern niedriger Massenbelegung des HADES Experiments.* Dissertation, Goethe Universität Frankfurt, 2005.

[27] J. Pietraszko, T. Galatyuk, V. Grilj, W. Koenig, S. Spataro, and M. Träger, "Radiation damage in single crystal CVD diamond material investigated with a high current relativistic ${}^{197}Au$ beam," *Nucl. Instrum. Meth.*, vol. A763, pp. 1–5, 2014.

[28] J. Pietraszko, "Beam Detectors in Au+Au run and future developments." `https://indico.gsi.de/materialDisplay.py?contribId=9&sessionId=4&materialId=slides&confId=2142`, 2013. [Online; accessed 26-September-2017].

[29] D. Belver *et al.*, "The hades rpc inner tof wall," *Nuclear Instruments and Methods in Physics Research Section A: Accelerators, Spectrometers, Detectors and Associated Equipment*, vol. 602, no. 3, pp. 687 – 690, 2009. Proceedings of the 9th International Workshop on Resistive Plate Chambers and Related Detectors.

[30] C. Agodi *et al.*, "The HADES time-of-flight wall," *Nucl. Instrum. Meth.*, vol. A492, pp. 14–25, 2002.

[31] O. Andreeva *et al.*, "Forward scintillation hodoscope for nuclear fragment detection at the high acceptance dielectron spectrometer (HADES) setup," *Instruments and Experimental Techniques*, vol. 57, no. 2, pp. 103–119, 2014.

[32] C. Behnke, T. Galatyuk, and J. Stroth, "Understanding the hades dilepton invariant mass spectra with urqmd simulations," *Journal of Physics: Conference Series*, vol. 426, no. 1, p. 012026, 2013.

[33] C. Hartnack *et al.*, "Modelling the many-body dynamics of heavy ion collisions: Present status and future perspective," *The European Physical Journal A - Hadrons and Nuclei*, vol. 1, pp. 151–169, Feb 1998.

[34] I. Fröhlich *et al.*, "Design of the pluto event generator," in *Journal of Physics Conference Series*, vol. 219 of *Journal of Physics Conference Series*, p. 032039, Apr. 2010.

[35] K. Bethge, G. Walter, and B. Wiedemann, *Kernphysik - Eine Einführung*. Berlin Heidelberg New York: Springer-Verlag, 2013.

[36] K. A. Olive et al, *Particle Physics Booklet*. Particle Data Group, 2014 ed., 2014.

[37] T. Scheib, Λ *and* K^0_S *Production in Au+Au Collisions at 1.23A GeV*. PhD thesis, Johann Wolfgang Goethe-Universitaet Frankfurt am Main, 2017.

[38] A. Dumitru and C. Spieles, "Inverse slope systematics in high-energy p+p and au+au reactions," *Physics Letters B*, vol. 446, no. 3, pp. 326 – 331, 1999.

[39] K. P. F.R.S., "X. on the criterion that a given system of deviations from the probable in the case of a correlated system of variables is such that it can be reasonably supposed to have arisen from random sampling," *Philosophical Magazine*, vol. 50, no. 302, pp. 157–175, 1900.

[40] S. Wheaton, J. Cleymans, and M. Hauer, "THERMUS A thermal model package for ROOT," *Computer Physics Communications*, vol. 180, pp. 84–106, Jan. 2009.

[41] B. Kardan, "Collective flow measurements with hades in au+au collisions at 1.23a gev." Talk by Behruz Kardan at the Annual Quark Matter conference, Chicago, USA in Februarz 2017.

[42] STAR Collaboration, L. Adamczyk, J. K. Adkins, G. Agakishiev, M. M. Aggarwal, Z. Ahammed, N. N. Ajitanand, I. Alekseev, D. M. Anderson, R. Aoyama, and et al., "Bulk Properties of the Medium Produced in Relativistic Heavy-Ion Collisions from the Beam Energy Scan Program," *ArXiv e-prints*, Jan. 2017.

[43] T. Anticic *et al.*, "Energy and centrality dependence of deuteron and proton production in pb + pb collisions at relativistic energies," *Phys. Rev.*, vol. 69, p. 024902, 2004.

[44] S. Wang *et al.*, "Light fragment production and power law behavior in Au + Au collisions," *Phys. Rev. Lett.*, vol. 74, pp. 2646–2649, 1995.

[45] M. J. Bennett *et al.*, "Light nuclei production in relativistic Au + nucleus collisions," *Phys. Rev. C*, vol. 58, pp. 1155–1164, Aug 1998.

[46] J. Barrette *et al.*, "Production of light nuclei in relativistic heavy-ion collisions," *Phys. Rev. C*, vol. 50, pp. 1077–1084, Aug 1994.

[47] T. Anticic *et al.*, "Production of deuterium, tritium, and He3 in central Pb + Pb collisions at 20A,30A,40A,80A , and 158A GeV at the CERN Super Proton Synchrotron," *Phys. Rev.*, vol. C94, no. 4, p. 044906, 2016.

Acknowledgments

Die vorliegende Arbeit wäre ohne die vielen kleinen und großen Beiträge von verschiedenen Seiten nie zu Stande gekommen:

Bei Prof. Dr. Blume, der in seiner Vorlesung mein Interesse an Kernphysik weckte und mich in seine Arbeitsgruppe aufnahm, wo er mir erst meine Bachelor- und jetzt Masterarbeit ermöglichte, möchte ich mich für die Betreuung und Unterstützung bedanken.
Dr. Manuel Lorenz gilt mein großer Dank für die hilfreiche Einführung in die Methodiken der Analyse und die Erstellung des Zweitgutachtens.
Auch Dr. Heidi Schuldes bin ich besonders dankbar für die intensive Betreuung und Korrektur und dass ich es nicht geschafft habe sie komplett in die Verzweiflung zu treiben. Danke für die Zeit und Geduld!
Der gesamten Arbeitsgruppe am IKF und allen Beteiligten der HADES-Kollaboration danke ich für die schöne Zeit an Uni, GSI und auf Konferenzen. Die Leidenschaft und Begeisterung für Forschung ist jedem anzumerken.
Speziell die Arbeitsatmosphäre im Büro mit Etienne Bechtel hat die tägliche Arbeit durch interessante und spa*ss*ige Diskussionen bereichert.
Marianne Freys unermüdlicher Einsatz im Dschungel der Formularwelt erleichterte die Arbeit im Institut ungemein.
Alle Freunde in Frankfurt und der Heimat haben mir immer einen Rückhalt gegeben, den ich gar nicht ausreichend schätzen kann.
Auch auf das Vertrauen und die Unterstützung meiner Familie konnte ich immer zählen, was mir das gesamte Studium überhaupt erst ermöglicht hat.

Danke!

Declaration

Hiermit erkläre ich, dass ich die Arbeit selbstständig und ohne Benutzung anderer als der angegebenen Quellen und Hilfsmittel verfasst habe. Alle Stellen der Arbeit, die wörtlich oder sinngemäß aus Veröffentlichungen oder aus anderen fremden Texten entnommen wurden, sind von mir als solche kenntlich gemacht worden. Ferner erkläre ich, dass die Arbeit nicht - auch nicht auszugsweise - für eine andere Prüfung verwendet wurde.

I hereby assert that the work at hand was done autonomously by myself, no other than the quoted sources have been used and all passages that have been adapted in wording or meaning from the cited works have been marked by indication of their source or reference. Furthermore, I assert that the work at hand, or any part of it, has not been used for another examination.

Maximilian Zuschke

Date